DTU Wind and Energy Systems

Practical uncertainty estimation for turbulence from ground-based lidar

Joram Jacob de Vries

DTU Wind-M-0856
July 2024

Author:
Joram Jacob de Vries

Title:
Practical uncertainty estimation for turbulence from ground-based lidar

DTU Wind-M-0856
July 2024

ECTS: 45

Education: Master of Science

Mark Charles Kelly
Ásta Hannesdóttir
DTU Wind & Energy Systems

Wim Bierbooms
TU Delft

Andrew Black
Vaisala

Levent Kücük
Vattenfall

Remarks:
This report is submitted as partial fulfillment of the requirements for graduation in the above education at the Technical University of Denmark.

DTU Wind & Energy Systems is a department of the Technical University of Denmark with a unique integration of research, education, innovation and public/private sector consulting in the field of wind energy. Our activities develop new opportunities and technology for the global and Danish exploitation of wind energy. Research focuses on key technical-scientific fields, which are central for the development, innovation and use of wind energy and provides the basis for advanced education at the education.

Technical University of Denmark
Department of Wind and Energy Systems
Frederiksborgvej 399
4000 Roskilde
Denmark
www.wind.dtu.dk

PRACTICAL UNCERTAINTY ESTIMATION FOR TURBULENCE FROM GROUND-BASED LIDAR

by

JORAM DE VRIES

to obtain the degrees of

Master of Science
in Wind Energy
at Technical University of Denmark

Master of Science
in Aerospace Engineering
at Delft University of Technology

To be defended on the 13th of September 2024

Supervisors:	Wim Bierbooms	TU Delft
	Mark Charles Kelly	DTU
	Ásta Hannesdóttir	DTU
	Levent Kücük	Vattenfall
	Andrew Black	Vaisala
Defence committee:	Dominic Von Terzi	TU Delft
	Lars Landberg	DNV
Start date:	November 1, 2023	
End date:	July 31, 2024	
Student numbers:	TU Delft:	4855779
	DTU:	S223727

An electronic version of this thesis is available at
`https://repository.tudelft.nl` and `https://findit.dtu.dk`

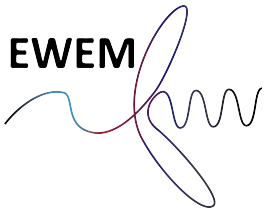

Abstract

The global energy consumption relies heavily on fossil fuels, which are projected to be depleted by 2050. This makes it necessary to optimize renewable sources such as wind energy. However, wind energy faces challenges due to the unpredictability and turbulence of wind patterns. Traditional wind turbines are limited by their reactive approach to turbulence. To address this issue, the integration of lidar technology in wind turbines provides a predictive advantage, enhancing the control of wind parks by offering insights into incoming wind disturbances and improving feedback mechanisms. A new method for adjusting ground-based lidar turbulence intensity measurements is investigated in this master's thesis, aiming to reduce measurement uncertainties. A novel turbulence intensity equation, developed using perturbation theory, serves as the foundation for an adjustment model that has been validated against existing standards. This adjustment method was tested in both virtual environments and on an actual wind site in the Netherlands, demonstrating its effectiveness in reducing uncertainties associated with lidar data. The study also utilizes the findings of a joint-industry project to refine data precision and compares various adjustment methods, ultimately showing that the perturbation-based adjustment improves the alignment of lidar measurements with traditional met mast data. Furthermore, the thesis explores the acceptance of lidar technology through a model based on the technology acceptance framework, revealing that reducing measurement uncertainties positively impacts the perceived usefulness and adoption of lidar systems. This research aims to enhance the accuracy and reliability of wind energy assessments using ground-based lidar, paving the way for broader adoption in the industry. Future work should focus on expanding the dataset, incorporating advanced machine learning techniques, and extending the turbulence intensity equation to accommodate complex terrains, further reducing uncertainties in lidar measurements.

Preface

This master's thesis is submitted to fulfill the requirements for obtaining the master's degree in Aerospace Engineering at Delft University of Technology, as well as the master's degree in Wind Energy at the Technical University of Denmark under the European Wind Energy Master (EWEM) program. The work was conducted in collaboration between the Department of Aerospace Engineering at TU Delft, the Netherlands, and the Department of Wind Energy at DTU in Lyngby, Denmark. The supervision from DTU has been done by Mark Charles Kelly and Ásta Hannesdóttir and from TU Delft by Dr.ir. W.A.A.M. (Wim) Bierbooms.

173,448,000. That is how many seconds I have studied at the TU Delft. Of those 173,448,000, I spend 31,536,000 seconds at the Technical University of Denmark. These two universities are the cornerstone of this Master's thesis project. I am just a small part of the history of these two universities, especially if you place my 173,448,000 seconds against the 5.758.845.369 seconds that the TU Delft exists, and the 6.167.430.969 seconds that the DTU exists on this earth. Still, I hope that I gathered knowledge that will help me further in life. And even though I won't last as long as these universities, I hope I can make an impact on the world through the knowledge gathered at these two brilliant universities. The academic journey has been an amazing ride.

First and foremost, I want to thank my university supervisors for their guidance throughout my thesis. Throughout the thesis period, they helped me in the organization, research, and execution of the project, through their knowledge, critical thinking, and positive feedback. They offered great support whenever my project stumbled upon problems. I want to massively thank Wim Bierbooms for his great support from the Delft side of things. He taught me to be mindful of my research and sometimes take a step back and put my focus back where it needed to be. His expertise in supervising thesis projects was evident from the start and his insights were super helpful to reach a well-validated final project. I am also very thankful to Mark Kelly for his amazing expertise in meteorology. Through the numerous calls we had, I have the feeling I got a private course in meteorology. His positive but critical feedback on my work helped shape this research. Lastly, I want to express my gratitude to Ásta Hannesdóttir, who has been a tremendous help, especially in teaching me her knowledge of turbulence. With her help, I had created turbulence boxes way faster than I thought I could. With her clear and positive remarks, I could improve my work a lot.

One big part of my thesis work was my opportunity to work together with Vattenfall. This was one of my main motivators for doing this master's thesis work: getting experience in the industry and learning the ways of working with one of the industry's biggest players. This could have never happened if it wasn't for my amazing supervisor and manager Levent Kücük. I want to thank him for his great guidance, making me feel right at home in Vattenfall's onshore wind resource team. He and the rest of the wind resource team gave me a great experience at Vattenfall, not only supporting me in my thesis work but also showing me what it means to work in the wind industry. Not only did Vattenfall give me industry insight, but Andrew Black did as well. This will not be the last time that I mention his name, as his work is mentioned throughout the report. Andrew gave me the great opportunity to extend his work on perturbation theory and has been a supportive supervisor throughout the entire project, helping me dissect the new turbulence intensity formula. His experience with Vaisala also greatly helped in my understanding of lidar equipment.

Then I would like to thank everyone who has supported me throughout the past two years of this master's. I want to thank all the friends I made along the way. I want to thank the rest of the EWEM batch, who had to go through the same program as me and therefore knew best how to give inside support. I want to thank all my friends in the Netherlands, who were always there to take my mind off my studies and focus on all the fun stuff life has to offer. Most importantly I want to thank my family, especially my parents, who have always been there for me and supported me in everything I have done and therefore made me accomplish my dreams. Last but not least, I want to thank my beautiful girlfriend, who not only supported me throughout this master's degree but also throughout my bachelor's degree. Your love and support always gave me motivation and made me the guy I am today. Thank you all!

Joram de Vries

Contents

List of Figures

List of Tables

Nomenclature

α	Kolmogorov constant	–
$\alpha\epsilon^{2/3}$	Mann turbulence parameter	–
β	Bias magnitude	–
β	Systematic error	–
ϵ	Combination of fluctuation terms after Reynolds decomposition	–
ϵ	Random error	–
ϵ	Turbulence dissipation rate	–
Γ	Eddy lifetime factor	–
γ_{ij}	Scalar inflation tensor	–
$\hat{y}$	Predicted output value	–
$\overline{u}$	Mean component of the stream-wise longitudinal component of wind field	m/s
$\overline{v}$	Mean component of the lateral transversal component of wind field	m/s
$\overline{w}$	Mean component of the vertical component of wind field	m/s
ϕ	Coefficient of viscosity	$\mathrm{Pa} \cdot \mathrm{s}$
ϕ	Half-opening angle	$^\circ$
σ	Standard deviation of wind speed	m/s
σ_u	Standard deviation of the stream-wise longitudinal component of wind field	Hz
θ	Azimuth angle	$^\circ$
A^+	Pseudo-inverse matrix	–
b_i^2	Estimate of the variance of the systematic error distribution	–
b_{ik}	Estimate of the covariance of the systematic errors in i and k	–
C	Zephyr correction factor	–
d_f	Focus distance for a CW lidar	m
f	Frequency	Hz
I	Turbulence intensity	–
i	Wind bin	–
L	Mann turbulence length scale	m
L	Obukhov length	m
L_u	Integral length scale	m
n	Point within wind bin	–

N_i	Number of TI measurements	–
P	Weighting matrix for using horizontal components	–
r	Error distribution	–
s_i^2	Estimate of the variance of the random error distribution	–
S_u	Single-sided velocity component spectrum	m/s
s_{ik}	Estimate of the covariance of the random errors in i and k	–
u	Stream-wise longitudinal component of wind field	m/s
u'	Fluctuating component of the stream-wise longitudinal component of wind field	m/s
v	Lateral transversal component of wind field	m/s
v'	Fluctuating component of the lateral transversal component of wind field	m/s
v_r	Radial velocity	m/s
w	Vertical component of wind field	m/s
w'	Fluctuating component of the vertical component of wind field	m/s
y	Actual output value	–
T	Temperature	°
t	Time	s
U	Wind Speed	m/s

Abbreviations

Abbreviations	*Description*
AC	Acceptance Criteria
CFD	Computational Fluid Dynamics
CNR	Carrier-to-Noise
CSV	Comma Separated Value
DBS	Doppler Beam Swinging
FM	Frequency Modulation
GBL	Ground-Based LiDAR
GUM	Guide to the Expression of Uncertainty in Measurement
IDT	Innovation Diffusion Theory
IEC	International Electrotechnical Commission
ISO	International Organization for Standardization
JCGM	International Joint Committee for Guides in Metrology
JIP	Joint Industry Project
LiDAR	Light Detection and Ranging
LoA	Limits of Agreement
LPU	Law of Propagation of Uncertainty
LSTM	Long Short-Term Memory
L-TERRA	Lidar Turbulence Error Reduction Algorithm
MAE	Mean Absolute Error
ML	Machine Learning
MRBE	Mean Relative Bias Error
MRI	Magnetic Resonance Imaging
MSE	Mean Squared Error
N	North
NW	North-West
PDM	Power Deviation Matrix
QC	Quality-Controlled
RANS	Reynolds-averaged Navier-Stokes
RDT	Rapid Distortion Theory
REWS	Rotor Equivalent Wind Speed
RHS	Right-Hand Side
RIX	Ruggedness Index
RP	Recommended Practice
RMSE	Root Mean Square Error
RRMSE	Relative Root Mean Square Error
TAM	Technology Acceptance Model
TI	Turbulence Intensity
TI AM	Turbulence Intensity Adjustment Method
TWh	Terawatt-hours
VAD	Velocity Azimuth Display
WEGS	Wind Energy Generation Systems
WRF	Weather Research and Forecasting
WT	Wind Turbine

Introduction

Global energy consumption currently stands at around 200,000 Terawatt-hours (TWh), with wind energy contributing approximately 5,000 TWh to this figure [3]. However, more than half of this energy generation still relies on fossil fuels, and experts predict that oil and gas reserves will be exhausted by 2050 [4]. Therefore, it is essential to expand and optimize wind energy to meet energy needs in the future. One of the challenges of wind energy is the unpredictability of wind patterns, which is further complicated by the turbulent nature of wind fields [5]. Traditional wind turbines are designed to optimise power output and reduce structural stress, but they can only react to turbulence once it has already affected the turbine. However, the recent integration of lidar technology in wind turbines offers a new approach by providing predictive insights into incoming wind disturbances. This technological advancement is particularly crucial in managing the complexity of controlling wakes within wind parks, where lidar's capability to measure airflow and predict wake locations significantly enhances feedback mechanisms [6]. Central to the performance of wind turbines is the power curve, a metric highly sensitive to atmospheric conditions, including turbulence intensity (TI) [7]. While lidar has proven effective in remote wind speed measurements at altitudes surpassing the hub heights of turbines, its limitation lies in its inability to resolve finer scales of turbulence due to its reliance on large volume averaging. Nonetheless, lidar's accuracy in measuring first-order quantities like wind speed and direction has garnered widespread acceptance. The challenge, however, arises in measuring second-order quantities such as turbulence intensity. To address this, a recommended practice for ground-based vertical profiling lidar has been developed. A key component of this research is implementing this practice on an existing wind site. Additionally, this study aims to explore alternative methodologies for quantifying turbulence intensity, thereby contributing to the broader understanding and optimization of wind turbine efficiency. The master thesis work aims to increase the acceptance of ground-based lidar usage. To increase this acceptance, the thesis work tackles an academic and a practical challenge. Academically, the research looks at the derivation of a new turbulence intensity equation by exploiting perturbation theory. This work therefore adds to the research into renewable energy technology by exploiting the knowledge in ground-based lidar technology. Practically, the findings of a recommended practice by DNV in IEA Wind Task 32 [8] will be implemented on a flat wind site in the Netherlands. In this way, the work will add to the already existing experience in reducing uncertainties in turbulence intensity predictions, therefore paving the way to the widespread usage of ground-based lidar systems. The master's thesis report begins with a comprehensive literature review in chapter 1, which identifies a specific problem after a thorough exploration of the theoretical underpinnings and the latest lidar technology. Then, chapter 2 provides the project framework necessary to establish a methodology and research setup for addressing the core research inquiries. In chapter 3, the analysis of the data provided by Vattenfall involves data filtering, error metric computation, and statistical analysis. After this, chapter 4 is dedicated to the derivation of the TI equation for a continuous-wave lidar using perturbation theory. Subsequently, in chapter 5, an adjustment method is introduced and tested in a virtual turbulence environment, with a comparative analysis of different adjustment methods. Furthermore, chapter 6 conducts an uncertainty analysis addressing various lidar uncertainty types and performs statistical and sensitivity analyses. Then, chapter 7 explores the acceptance of lidar TI measurements utilizing a technology acceptance model. Finally, the report concludes with a presentation of findings and recommendations in chapter 8.

VATTENFALL

Chapter 1

Literature review

In this chapter, an extensive review of the literature and industry benchmarks relevant to the research topic has been carried out. The primary objective is to identify key research areas and gain a comprehensive understanding of the current state of knowledge in the field. This chapter will focus on various crucial aspects, including lidar technology, turbulence intensity, perturbation theory, and a recommended practice setup by DNV. By exploring these topics in detail, we aim to lay a solid foundation for this thesis project's subsequent data analysis and findings. This chapter will go over the theoretical background of these topics, the current state-of-the-art, and lastly, the chapter will pose a problem setting with research questions for this thesis project.

1.1 Theoretical background

This section involves an in-depth review of the literature and industry benchmarks related to the research topic. The review aims to identify the relevant research areas and comprehensively understand the current state of knowledge in the field. The section will go over lidar technology in subsection 1.1.1, turbulence intensity in subsection 1.1.2, the perturbation theory in subsection 1.1.3, mathematical preliminaries in subsection 1.1.4, atmospheric stability in subsection 1.1.5, the recommended practice in subsection 1.1.6, and the GUM method in subsection 1.1.7.

1.1.1 Lidar

Lidar is an acronym for Light Detection And Ranging. Lidars have only just been introduced in wind energy [9], but the first remote sensing turbulence study using a 360° scan in a horizontal plane was carried out by Browing and Wexler [10]. Later work by Kropfli showed that the technique could be used to make estimates for turbulent kinetic energy [11]. It can be divided into two types: range-finding lidar and Doppler lidar. The former is utilized in autonomous vehicles [12]. This type of lidar relies on light to determine the distance between the lidar and an object. The latter is mostly used in wind turbines. It can be used to measure distance and gather information on the Doppler shift of the light. This kind of lidar is similar to radar, but it makes use of a different frequency of light that interacts with the atmosphere.

Doppler effect

The Doppler effect is classically described as a moving vehicle producing a change in acoustic pitch between approaching and departing. When the vehicle moves towards you, the sound is compressed, creating a higher pitch. The same is true for light; when something is moving away, the light waves expand. We can use this to measure the shift in light to determine where the aerosols are moving (assuming they move perfectly with the wind). Most commercial wind lidars use homodyne detection to detect the Doppler shift. With homodyne detection, information on the magnitude of the shift is collected, but no information on whether it is positive or negative. Therefore we don't know if the wind is moving towards or away from the lidar. Heterodyne detection gathers both magnitude and sign but requires more hardware, driving up the cost to produce the lidar.

Carrier to Noise ratio

For lidar, we use the Carrier to Noise ratio. CNR is a measure of the amount of signal returned (i.e., the reflected light from the Doppler effect) to the lidar compared to the amount sent. CNR is used to show the variance in instrument noise, which is overestimated by lidar in unstable conditions [13]. Continuous wave lidar focuses the laser beam to measure a volume in the atmosphere, whereas pulsed lidar sends a coherent light signal and uses

time of flight to measure a volume in the atmosphere. Either of these methods can be fixed beams or scanning. Different configurations of lidar technology exist, as explained by A. Sathe and J. Mann in their article [14]. There are three modes of operation: Staring Mode, Scanning Mode in a cone, and Scanning Mode in a vertical plane. In the staring mode, the lidar beam is fixed at a specific angle, while in the scanning mode, the beam rotates. It's important to filter the data before analyzing it, to ensure that the wind sensors and lidar system are compatible. As mentioned by D. Kim et al [15], some factors to consider include wind speed range, CNR, lidar availability, precipitation, and tower shadow.

Vector averaging

Unlike a cup anemometer, which takes a scalar average of the air due to its insensitivity to wind direction, a lidar takes a volume of air. Over a certain averaging interval, the lidar takes measurements around the volume. Taking these averaged individual components together creates a vector [16]. The scalar average is the average magnitude of the vector, which will differ from the magnitude of the vector average. Lidar uses the Doppler effect in multiple directions which results in a radial velocity in a way that is similar to obtaining average values of vector components from which the vector can be reconstructed, therefore lidar measurements lead to vector averages. Due to the difference in averaging between cup and lidar, a bias occurs in the lidar measurements, when compared with cup anemometer data.

1.1.2 Turbulence

When wind flows past a turbine, the kinetic energy of the wind can be converted into electrical energy by that turbine. Since the hub height of turbines is approximately 100m, the hub is located in the atmospheric boundary layer [17]. In this boundary layer, high turbulence is located [18]. This means that wind turbines are influenced by high turbulence. Turbulence intensity is therefore significant for wind farms. Turbulence intensity is defined as the mean wind speed ($\overline{u}$) over the standard deviation (σ) of wind speed: $I = \frac{\sigma}{\overline{u}}$ [19]. Studies have looked into the impacts of turbulence intensity on wind turbine power output and aerodynamic loads.

Wind turbines are affected by turbulence in one of two ways: fluctuations in extracted wind power [20] or load fluctuations, which can occur at different components of the turbine [9]. The produced power depends on both the mean and variance of the wind speed, which is analytically shown with Reynolds decomposition in Equation 4.2. This leads to different effects on the different regions of power [21]. Turbulence influences power mostly in the region around rated wind speed. The power output increases with the increase of turbulence intensity at lower wind speed and decreases with the increase of turbulence intensity in the transition region to rated power [19]. Turbulence intensity has an impact on the aerodynamic loads on wind turbines. According to Sathe and Mann [14], these fluctuations result in the inefficiency of harnessing energy from the wind flow and could inflict fatigue damage on the turbine. Due to turbulence, fatigue loads on wind turbine blades increase [22], while turbulence can also lead to extreme load events [23]. This is especially important for the creation of acceptance criteria in the recommended practice in subsection 1.1.6.

Taylor's frozen turbulence hypothesis

Taylor's hypothesis plays a pivotal role in understanding wind flow behavior and its implications for wind energy applications. Proposed by Geoffrey I. Taylor in 1938, this hypothesis posits that the fluctuations in wind speed can be treated as a random process, assuming that the characteristic time scale of the turbulence is much smaller than the time scale of the mean wind speed variations [24]. In the context of wind energy, this hypothesis is crucial for analyzing the split of wind speed into mean and fluctuating components. Turbulence, characterized by rapid and irregular wind speed variations, significantly influences the efficiency and stability of wind turbines. The turbulence intensity, defined as the ratio of the standard deviation of the fluctuating wind speed to the mean wind speed, is a key parameter in quantifying turbulence effects [25].

Capturing the dynamic nature of eddies in three dimensions and quantifying their dimensions in real-time is a challenging task. Direct observation of these eddies is difficult. One common approach involves monitoring fluctuations in variables like wind speed, specific humidity, or temperature at a single location over time to observe the passage of eddies past the sensor. It is important to note that these eddies may change in size and shape during this passage. To better understand this phenomenon, Taylor's hypothesis [24] can be used within the framework of the total derivative. For instance, when considering a variable like temperature, denoted by T, the change in T over time at a given location (where a sensor is typically placed) can be expressed as the sum of the total derivative and the temperature advection [26].

$$\frac{\partial T}{\partial t} = \frac{DT}{Dt} - \overrightarrow{U} \cdot \overrightarrow{\nabla} T \tag{1.1}$$

The concept of temperature advection refers to the change in temperature detected by a sensor due to the movement of warmer or colder air past it. On the other hand, the total derivative represents the temperature change experienced by an air parcel as it passes by the sensor. This change can occur due to various processes such as radiation absorption or emission, condensation or evaporation, and compression or expansion. According to Taylor's hypothesis, turbulent eddies, similar to air parcels' circulation, remain nearly unchanged or "frozen" as they pass by the sensor, making the temperature change within each eddy insignificant [27].

$$\frac{DT}{Dt} \sim 0 \tag{1.2}$$

This simplifies the expression to:

$$\frac{\partial T}{\partial t} = -\overrightarrow{U} \cdot \overrightarrow{\nabla} T \tag{1.3}$$

Based on empirical studies, it has been observed that when the turbulence-induced variation in wind speed is less than half of the mean wind speed, the local temperature gradients across an eddy remain advected across the sensor without significant alteration to the eddy itself by the mean wind [26]. This approximation is valuable as it provides a fundamental tool for inferring the sizes of turbulent structures from observational data collected over time. If the approximation holds, the size of a turbulent eddy can be estimated by multiplying the time taken for an eddy to traverse the sensor by the mean wind speed responsible for its advection. Therefore, the eddy size can be calculated by multiplying the eddy advection time by the mean wind speed. This method has proven to be essential in understanding the complexities of turbulence structure [27].

1.1.3 Perturbation theory

Perturbation theory involves using methods to find an approximate solution to a problem by starting from the exact solution of a related, simpler problem. It's particularly useful in systems where a small parameter, known as the "perturbation," slightly alters a known, solvable problem. The idea is to start with a simple, solvable problem and then gradually adjust the solution to account for the effects of the perturbation. This method uses the same building blocks as the Guide to the Expression of Uncertainty in Measurement (GUM), the preferred uncertainty method in wind energy. It utilizes Taylor expansion and focuses on low-order moments. Further explanation of this method can be found in subsection 1.1.7.

Steps in perturbation theory

1. Unperturbed Solution:
    - Solve the problem without the perturbation. This solution is usually denoted as the zeroth-order approximation.
2. First-Order Perturbation:
    - Calculate the first-order correction, which involves the first power of ϵ. This gives a better approximation of the true solution.
3. Higher-Order Corrections:
    - If needed, calculate second-order, third-order, higher-order, corrections, each involving higher powers of ϵ.
4. Summing the Series:
    - The approximate solution to the original problem is the sum of the unperturbed solution and all the perturbative corrections.

Implementation for lidar

During a presentation by Andrew H. Black, a new framework for LiDAR measurement uncertainties was developed using perturbation theory [28]. The presentation starts with a simple case for mean wind speed, where an anemometer is placed in a flat, turbulent flow. Rosenbusch [29] and Robey [30] use a 2nd-order Taylor series expansion for horizontal wind speed in this case. However, this solution becomes complex for more intricate flows. Therefore, the perturbation method is proposed as a solution. Using Reynolds decomposition, binomial approximation, and time averaging, this case concludes with the statement that the Perturbation Method is adequate for this application. This case is then further advanced with the cases of turbulent flow, inclined turbulent flow, and lidar in complex flow. These all conclude with a generalized framework for mean wind speed, with the opportunity for further development in turbulence intensity.

1.1.4 Mathematical preliminaries

The wind field will be defined as $\mathbf{v} = (u, v, w)$, where the coordinate system will be defined to be right-handed with u as the stream-wise longitudinal component in the x_1 direction, v is the lateral transversal component in the x_2 direction, and w is the vertical component in the x_3 direction. As said by Sathe and Mann [14], here at a given focus distance for a CW lidar (d_f), the radial velocity can be written as:

$$v_r(\theta) = u\cos(\theta)\sin(\phi) + v\sin(\theta)\sin(\phi) + w\cos(\phi) \tag{1.4}$$

where θ is the azimuth angle and the half-opening angle (ϕ) is kept constant throughout the scan at 30° [31]. As can be seen in Equation 1.4, the radial velocity is a function of the three wind field components u, v, and w. Therefore, since there are three unknowns, three different measurements of the radial velocity are needed to know the wind field components.

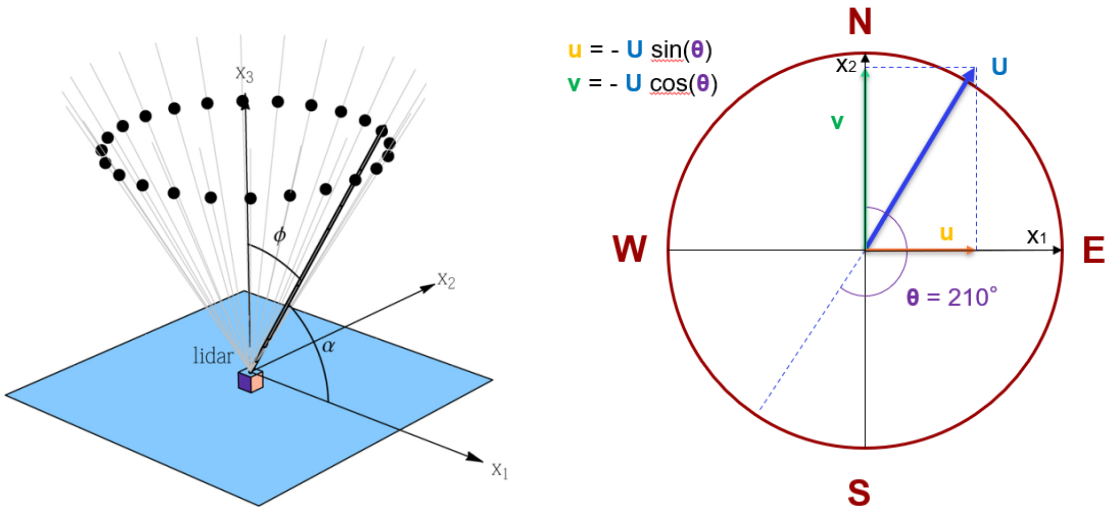

(a) Schematic of continuous wave ground-based lidar as given in [14]

(b) Schematic showing the u and v component of wind including the azimuth angle θ

Figure 1.1: Wind Field

The ZephIR 300 is a vertical profiling wind lidar used in a measurement campaign. It operates by transmitting a laser beam through a rotating prism to perform a velocity azimuth display (VAD) scan with a scanning cone angle of 30 degrees [31]. For each height, one complete rotation takes 1 second, during which 50 measurements of 20 milliseconds are taken to reconstruct the 3-D wind vector (horizontal and vertical wind speed, and wind direction). The manufacturer specifies wind speed and wind direction accuracies as better than 0.1 m/s and 0.5 degrees, respectively, with a wind speed range from 1 m/s to 80 m/s. The height range is 10m to 200m above the instrument, extendable to 300m in the software. The instrument can measure up to 10 user-configurable heights and a pre-fixed height of 38m above the instrument, with the laser beam focus changing after each VAD scan [32].

The wind retrieval from the VAD scan assumes a homogeneous wind field in the scanning cone at each measurement level. The probe length increases quadratically with height, ranging from 0.07m at 10m height to 30m at 200m. Clouds above the maximum range can affect the Doppler signal, and a cloud removal algorithm is used to correct for this, involving measurements at an additional higher altitude [33] [34]. Due to the homodyne detection, there is a 180-degree ambiguity in the measured wind direction and a sign ambiguity in the vertical wind speed. To address this, the ZephIR 300 includes a meteorological station with a sonic anemometer, and wind direction information is fed into the internal algorithm to determine the true wind direction. Additionally, zero wind speed cannot be measured, as a small region around zero Doppler shift needs to be filtered out [35]. The instrument reports unaveraged data as well as quality-controlled (QC) 10-minute averaged data, including horizontal and vertical wind speed, wind direction, minimum, maximum, and standard deviation of the horizontal wind speed, and turbulence intensity. Reasons for not passing QC can include very low wind speed events, window obscuration or interference with the laser beam, or adverse atmospheric conditions affecting lidar wind speed measurements.

1.1.5 Atmospheric stability

It is important to consider atmospheric stability when making lidar measurements, as it can affect the accuracy of the results. The difference between cup anemometer and lidar measurements is dependent on the atmospheric stability. The turbulence ratio decreases with height and increasing stability, which has been demonstrated in the IEA Wind expert report [13]. According to Gryning *et al* [36], atmospheric stability can be categorised into seven different stabilities based on Obukhov length intervals (Table 1.1). Additionally, σ_u increases linearly with mean wind speed under all the different stabilities, as discussed by Sathe *et al* [37]. Lastly, St. Martin *et al* [38] shows the influence of atmospheric stability and turbulence on the AEP production of a wind park. Next to the Gryning classification, Table 1.1 also shows classifications made by Kelly *et al* [39] and Pasquill [40]. According to Kelly *et al*, the use of L^{-1} instead of L is beneficial in the sense that L^{-1} has improved behavior due to L approaching zero for neutral conditions, and down to L^{-1} being analytically more convenient. This leads to a joint probability distribution $P(z_0, L^{-1})$, caused by L and z_0 (surface roughness length) varying over time. Pasquill stability classes are a different system used to categorize atmospheric stability. It makes use of the vertical mixing coefficient Kz, which describes the rate at which particles are mixed vertically through the atmosphere.

	Class	Gryning [36]	Kelly [39]	Pasquill [40]
1	Very stable	$10 \leq L \leq 50$ m	$0.02 \leq L^{-1} \leq 0.1$ m^{-1}	$Kz < 0.5$ m^2/s
2	Stable	$50 \leq L \leq 200$ m	$0.005 \leq L^{-1} \leq 0.02$ m^{-1}	$0.5 \leq Kz < 3$ m^2/s
3	Near-neutral stable	$200 \leq L \leq 500$ m	$0.002 \leq L^{-1} \leq 0.005$ m^{-1}	$3 \leq Kz < 10$ m^2/s
4	Neutral	$\lvert L \rvert \geq 500$ m	$\lvert L^{-1} \rvert \leq 0.002$ m^{-1}	$10 \leq Kz < 40$ m^2/s
5	Near-neutral unstable	$-500 \leq L \leq -200$ m	$-0.005 \leq L^{-1} \leq -0.002$ m^{-1}	$40 \leq Kz < 85$ m^2/s
6	Unstable	$-200 \leq L \leq -100$ m	$-0.01 \leq L^{-1} \leq -0.005$ m^{-1}	$85 \leq Kz < 130$ m^2/s
7	Very unstable	$-100 \leq L \leq -50$ m	$-0.02 \leq L^{-1} \leq -0.01$ m^{-1}	130 m^2/s $\leq Kz$

Table 1.1: Classification of atmospheric stability by various research papers

Wind shear

Wind shear is the difference in either wind speed or direction between two layers of air in the atmosphere [41]. Vertical wind shear occurs due to the presence of the ground boundary layer [42]. At the ground's surface, the wind speed is zero due to the no-slip condition [43], and then it increases with height. Therefore the vertical velocity is modelled as a power law, as can be seen in Equation 1.5 [42], where y is the height above the ground, $V_\infty(H)$ is the inflow velocity at hub height H, and γ is the wind shear coefficient.

$$V_\infty(y) = V_\infty(H)(\frac{y}{H})^\gamma \tag{1.5}$$

Rotor equivalent wind speed

As said by Murphy *et al* [44], a rotor equivalent wind speed (REWS) metric shows the actual momentum encountered by a turbine rotor disk by accounting for vertical shear. REWS follows from IEC61400-12-1 [45], which goes into the power performance measurements of electricity-producing wind turbines. Wagner *et al* [46] first define REWS as weighting a 10-min average wind speed ($\overline{U_i}$) at a corresponding height by the corresponding area ratio (A_i/A), after this the authors account for turbulence and lastly they express REWS as wind speed, resulting in Equation 1.6.

$$U_{RE} = \sqrt[3]{\frac{1}{A}\left(\sum_i \overline{U_i^3} \cdot A_i\right)} \tag{1.6}$$

1.1.6 Recommended practice

A recommended practice (RP) has been developed for wind turbines' TI based on the results of a joint industry project (JIP) in DNV-RP-0661. Companies like Vattenfall are responsible for creating this RP. The RP has two main objectives: to provide a method for using Ground-Based LiDAR (GBL) TI measurements in combination with co-located met mast data, and to act as a supporting document when considering the use of GBL TI measurements for wind resource and wind turbine certification in combination with other applicable standards, recommended practices, and guidelines. The RP outlines recommended acceptance criteria (AC) for GBL TI measurements for both "loads" and "energy production assessment." The project used measurement data from

onshore sites with a "flat" terrain as defined by IEC 61400-1 or IEC 61400-12-1, and offshore sites as defined by IEC 61400-3-1 or DNV-ST-0437. This thesis research project will focus on the former. The RP can be used to determine site suitability and validate loads. It is also capable of preconstructing energy production assessments for the wind farm.

TI error metrics

For the project, the appropriate TI error metrics were found to be "mean relative bias error" (MRBE) and "relative root mean square error" (RRMSE). The MRBE, shown in Equation 1.7, provides the relative error or "TI bias" between the lidar and cup TI. On the other hand, the RRMSE, as depicted in Equation 1.8, compares the scatter of the two quantities. In these formulas, i represents the wind bin while n refers to each point within that bin.

$$TI\ MRBE_i[\%] = \frac{1}{N_i} \sum_{n=1}^{N_i} \left(TI_{\text{lidar},n,i} - TI_{\text{cup},n,i}\right) / TI_{\text{cup},n,i} \cdot 100 \tag{1.7}$$

$$TI\ RRMSE_i[\%] = \sqrt{\frac{1}{N_i} \sum_{n=1}^{N_i} \left(\left(TI_{\text{lidar},n,i} - TI_{\text{cup},n,i}\right) / TI_{\text{cup},n,i}\right)^2} \cdot 100 \tag{1.8}$$

Acceptance criteria

This recommended practice entails three different use cases, namely "site suitability", "load validation type testing", and "energy production assessment". According to the DNV report, turbulence intensity primarily affects the fatigue loads of a wind turbine and the observed effects are almost linear. Although TI also has an impact on extreme loads, it is enough in the current context to examine the effect of TI on fatigue loads because the acceptance level of extreme loads is more lenient than for fatigue, considering IEC61400-13. TI affects the results of energy production assessment in two ways. Ambient TI serves as an input into wake models. Additionally, TI has an impact on the consideration of performance losses due to wind characteristics. However, since this impact is significantly smaller than the impact on wake modeling, it has been disregarded. Based on this, the TI metric errors that are acceptable according to DNV-RP-0661 are as follows:

Site suitability

- $-3\% \leq TI\ MRBE \leq 10\%$ $(U > 7$ m/s$)$
- $-6\% \leq TI\ MRBE \leq 10\%$ $(U < 7$ m/s$)$
- $TI\ RRMSE \leq 15\%$ $(U > 7$ m/s$)$
- $TI\ RRMSE \leq 30\%$ $(U < 7$ m/s$)$

Load validation

- $TI\ MRBE \leq \pm 5\%$
- $TI\ RRMSE \leq 15\%$

Energy production assessment

- $TI\ MRBE \leq \pm 10\%$

Adjustment methods

The difference between measurements obtained through lidar and met mast is influenced by various factors such as atmospheric stability, instrument noise, low pass filter effects, and the variability in the volume of air measured by the lidar. If the difference between the two is insignificant and the error metrics are lower than the AC, the lidar data can replace the met mast data. The main objective of a TI adjustment method (TI AM) is to minimize the error and scatter between GBL and cup TI measurements. Ideally, the atmospheric stability will be described by physical expressions like the Monin-Obukhov length or Richardson Number. When a TI AM is applied, the model is trained and tuned using available data sets. The quality of the results provided by the TI AM fundamentally depends on the quality of the data used for training and tuning. GBL TI data can be adjusted using machine learning (ML) techniques or purely analytical approaches.

1.1.7 GUM method

One of the main drivers for not accepting lidar in the wind industry is the uncertainty of turbulence measurements. For wind energy, the uncertainty evaluation method of choice is the ISO/IEC Guide 98-3:2008 "Guide to the Expression of Uncertainty in Measurement" which is given by the International Joint Committee for Guides in Metrology (JCGM) [47]. According to Wei *et al* [1], the GUM evaluation method is based on the law of propagation of uncertainty (LPU). The authors also mention that a deviation in the accuracy of the evaluation can occur when the correlation between input quantities is ignored, thus requiring a correlation GUM method. Wei *et al* also gives the general flow chart of the GUM method, leading to the steps one should take for this evaluation, as can be seen in Figure 1.2.

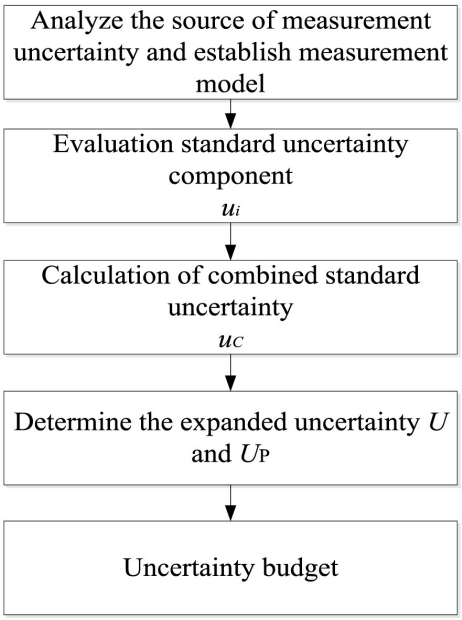

Figure 1.2: General flow chart of GUM method for evaluating measurement uncertainty [1]

1.2 State-of-the-art

Research on the usage of lidar measurements for turbulence started in 1972 [14], however, the implementation of commercial wind lidar systems only happened in the early 2000s [9]. In the current wind industry, the standard for wind measurements is still a cup anemometer [48], according to IEC 61400. A cup anemometer measures wind speed at a point, while lidar can measure air volume and flow more accurately [13] [49] [50]. When wind flows past a turbine, the kinetic energy of the wind can be converted into electrical energy by that turbine. Since the hub height of turbines is approximately 100m, the hub is located in the atmospheric boundary layer [17]. In this boundary layer, high turbulence is located [18]. This means that wind turbines are influenced by high turbulence. Turbulence intensity is therefore significant for wind farms. This section of the literature review will go into the state-of-the-art regarding lidar uses for wind farms, with a focus on its impact on TI measurements. The section will go into the relevant research areas, current perspectives, and opposing views.

1.2.1 Summary of relevant research areas

As mentioned by A. Sathe and J. Mann [14], lidars offer advantages over traditional meteorological mast anemometry, especially for measuring turbulent wind fields at great heights, which is expensive and challenging with met-masts. Despite lidars being extensively used for mean wind speed measurements and wind profiling, they have not yet gained widespread acceptance for turbulence measurements due to various challenges. For example, obtaining unfiltered statistics from the lidars' large probe volume still remains challenging. Currently, algorithms combine an isotropic turbulence model with raw lidar measurements. Nonetheless, Sathe and Mann suggest that an anisotropic turbulence model could provide a more realistic measure for turbulence statistics. Also, due to the growing use of wind lidars in wind energy, it is vital to understand atmospheric turbulence. As said, the TI difference between a point measurement and a volume measurement is dependent on atmospheric stability [51]. Under stable conditions, the motion of turbulence is small, while under unstable conditions the turbulent motion is large and thus results in lidar systems underestimating TI in stable conditions and

overestimating turbulence in unstable conditions when compared to a cup anemometer. Turbulence affects wind turbines by causing fluctuations in extracted wind power and loads on turbine components. This, in turn, leads to inefficient energy production and potential fatigue damage. Turbulence impacts a standard wind turbine power curve in two ways. The produced power depends on both the mean and variance of the wind speed, which is analytically shown with Reynolds decomposition by G. Alfonsi [52]. This leads to different effects on the different regions of power [21]. Turbulence influences power mostly in the region around rated wind speed. The power output increases with the increase of turbulence intensity at lower wind speed and decreases with the increase of turbulence intensity in the transition region to rated power [19]. TI has an impact on the aerodynamic loads on wind turbines. Due to turbulence, fatigue loads on wind turbine blades increase [22], while turbulence can also lead to extreme load events [23]. Perturbation theory can be used through the implementation of Reynolds decomposition for TI. As mentioned in subsection 1.1.3, perturbation theory involves methods for approximating solutions to problems by starting with the exact solution of a related, simpler problem [53]. Right now, however, GUM is the preferred uncertainty method in wind energy. Borraccino *et al* [54] uses the GUM approach to calibrate the relationship between the lidar-measured line-of-sight velocity and the reference velocity, while also using GUM for lidar uncertainty determination. Furthermore, GUM can be combined with Monte-Carlo simulations, which allows for an extended uncertainty analysis [55].

1.2.2 Current understanding and perspectives

It is essential to accurately estimate the wind resource when developing efficient wind farms [56]. The conventional method for measuring wind conditions involves using a cup anemometer and wind vane [25]. These technologies and the measurement uncertainty are highly regarded in literature [57] [58] [59]. The cup anemometer needs to be immune to flow distortion caused by surrounding terrain and obstacles, and it should be installed near the hub height of a wind turbine. This poses a problem, since turbines keep getting bigger the hub height increases as well. This causes cup measurements to be expensive and time-consuming. As said by Goit *et al* [60], several studies have already pointed out the prospect of using lidars for the measurements of the mean wind speed. The study by Goit concludes with the statement that after a long-term measurement campaign, lidar measurements proved to be acceptably accurate for wind speed and turbulence intensity.

The Lidar Acceptance Group, as outlined in IEC 61400-12-1, specifies technical criteria for the application of ground-based lidar systems in wind resource assessment and power curve testing [61]. These regulations serve as the foundation for accepting lidar measurements and addressing uncertainties inherent in the technology. Presently, ground-based lidar devices are deemed suitable primarily for flat terrain applications. Albers *et al.* identifies essential prerequisites for securing acceptance of lidar measurements, including traceability to national standards, repeatability in diverse environmental conditions, and a comprehensive analysis of measurement uncertainties. Another crucial understanding is to acknowledge that wind tunnels cannot be utilized for lidar testing due to the substantial size of the wind scanning volume, a privilege enjoyed by cup anemometers. Consequently, each lidar must undergo testing against a suitably equipped meteorological mast. If the deviation of wind speed measured by the lidar, compared to the reference cup anemometer, falls within the standard uncertainty of the cup anemometer measurement for each wind speed bin, the correction of the lidar based on cup measurements becomes less meaningful. In such cases, it is more appropriate to consider the lidar's wind speed measurement as valid, accounting for uncertainties such as the cup anemometer measurement uncertainty, systematic deviations in cup anemometer and lidar measurements, and statistical uncertainty in the comparison. While lidars offer a cost-effective alternative to meteorological towers, discrepancies in TI measurements pose a hurdle [62]. The LiDAR Turbulence Error Reduction Algorithm (L-TERRA) was developed to enhance lidar TI estimates, incorporating physics-based corrections and machine-learning techniques. L-TERRA performed well under stable conditions but faced challenges in mitigating variance contamination in unstable conditions. By reducing errors in lidar TI estimates, L-TERRA can improve the reliability of lidar measurements. This can lead to more widespread adoption of lidars for wind resource assessment, particularly as turbine hub heights continue to increase. However, the initial impediments hindering the widespread adoption of lidar technology include specific application guidelines and the associated purchase costs, as highlighted by Clifton *et al* [8]. Despite these challenges, lidar is an evolving technology that contributes to cost reduction in wind energy projects by facilitating more affordable site selection. Furthermore, it presents opportunities for enhanced energy capture and diminished structural loads. Addressing these challenges, IEA Wind Task 32 identifies four crucial requirements to foster greater acceptance of lidar systems: the establishment of standards, the cultivation of expertise, the development of data tools, and the refinement of physics models.

1.2.3 Identification of opposing views and controversies

Lidar technology is complex and new challenges often arise. A recent paper by F. Kelberlau and J. Mann [63] discusses the issue of cross-contamination on the turbulence velocity spectra produced by using a Doppler beam

swinging scanning technique. Cross-contamination occurs when measurements from different lidar beams are used to reconstruct three-dimensional wind vectors. The researchers conducted experiments where they sampled wind data in a simulated turbulence environment to predict lidar-derived turbulence spectra for various wind directions and measurement heights. The study found that the shape of lidar-derived spectra is influenced by the angle between wind direction and lidar beams. The conventional processing of horizontal wind velocity components is affected by cross-contamination. F. Kelberlau and J. Mann's study specifically examines the cross-contamination between the three velocity components in DBS lidars, which can result in deviations in turbulence velocity spectra. The study also found that the averaging process used in DBS lidars may reduce the accuracy of turbulence measurements. Finally, the alignment of the lidar beams to the incoming wind direction can also affect the shape of the turbulence spectra.

Furthermore, the implementation of lidar systems is impacted by a low pass filter effect, since the lidar measurements are spatial [51]. Low-pass filtering introduces distortions in the lidar profile shape. This means that both the removal of high frequency, which is the removal of details up to a certain spatial extension, and the spatial distortion produce a reduction of the range resolution [64]. Noise removal in the retrieval of lidar optical properties using low-pass filters results in the loss of useful information contained in the signal. This is problematic, as it means that the filtered signal may not provide a complete and accurate representation of the lidar optical properties. Another problem arises when looking at the differences between lidar and cup anemometer measurements in different terrain conditions. To compare the two, research was conducted on Jeju Island in South Korea [15]. In this research, three different measurement sites were chosen, all with different topographical complexities. The terrain complexity was evaluated using a Ruggedness Index (RIX). It was chosen to also perform CFD analysis at the site with the highest RIX. In this paper, it was concluded that the lidar error rates ranged from 2% to 6% for the measurement sites, with a significant positive lidar error observed over a depression between two parasitic cones. Linear regression analysis showed that the existing wind measurements from lidar and cup anemometers were close to one, indicating a good correlation. The paper highlights the need for reducing uncertainties over various terrain complexities.

1.2.4 Contribution to the body of knowledge

After reviewing the current state of ground-based lidar technology for turbulence measurements in wind energy, it has been found that lidar has several advantages over traditional cup anemometers, especially in measuring turbulent wind fields at greater heights. The literature review traced the historical development of lidar applications and examined current industry practices, standards, and challenges, shedding light on the complexities and uncertainties associated with lidar measurements. The proposal aims to contribute to the understanding of ground-based lidar applications for measuring turbulence in the wind energy sector by addressing challenges and controversies in the field to improve the reliability of lidar measurements. The research will offer practical solutions, ultimately enhancing the effectiveness of ground-based lidar systems for wind resource assessment and power curve testing by promoting the adoption of lidar technology in the industry, leading to advancements in wind energy efficiency and sustainability.

1.3 Problem Setting

As ground-based lidar technology continues to advance and play a vital role in wind energy applications, there is a pressing need to address existing gaps and challenges to enhance its acceptance and reliability. This section delves into the identified gaps, setting the stage for the research questions that will guide this thesis project. The integration of perturbation theory with recommended practices from a JIP emerges as a potential solution to mitigate uncertainties in turbulence intensity predictions using ground-based lidar.

1.3.1 Gap identification

Lidar technology has proven to be effective in wind energy applications, but uncertainties in TI predictions are still a major challenge. Perturbation theory shows promise in addressing this issue, particularly in ground-based lidar measurements of TI. The JIP offers valuable insights into wind turbine site selection based on recommended practices. Understanding the link between these practices and academic research on ground-based lidar is crucial. Identifying the gap between JIP insights and current academic practice can improve the understanding of the criteria for lidar acceptance. It's essential to assess the feasibility and applicability of JIP findings, especially in real-world scenarios with concurrent lidar and cup anemometer data, for informed decision-making. Expanding the use of lidar technology to complex terrains presents unique challenges. Recognizing the differences in wind resource assessment between "flat" and "complex" terrain and identifying suitable wind

sites owned by Vattenfall for further analysis are critical steps in broadening the scope of research. Since the overall acceptance of lidar technology in the wind energy market is influenced by various factors, understanding the current level of acceptance, the factors influencing decision-making, and alternative methods available for measuring turbulence will contribute to a comprehensive assessment of lidar's role in the industry.

1.3.2 Research questions

How much does the uncertainty of ground-based lidar turbulence measurements in wind energy decrease by implementing a perturbation theory-based adjustment?

1. What magnitudes of uncertainty can be expected when using perturbation theory in turbulence intensity predictions using ground-based lidar?
2. How well does the adjustment method follow the insights from the joint industry project for the implementation of TI prediction in a flat wind site?
3. To what extent does this research contribute to the enhanced acceptance of lidar in measuring turbulence in wind energy?

Chapter 2

Project framework

As wind energy is rapidly expanding across the globe with new megawatt projects being initiated in Europe, the US, and China, measuring wind speed has become increasingly important. This is because the power generated by a wind turbine is dependent on the wind speed. However, aside from wind speed, measuring turbulence is also crucial since it is a primary input in load assessment. Currently, the wind energy industry still relies on meteorological masts equipped with cup and/or sonic anemometers as the standard method for measurement. However, these are quite expensive, particularly offshore. To address this issue, remote sensing in the form of lidars has been introduced in the industry to conduct verification campaigns where lidar and cup anemometer measurements are compared [34] [35]. The aim of this thesis is to encourage the use of lidar as a standard measuring instrument in the future. However, for this to happen, lidar turbulence measurements must comply with the IEC standard for loads (IEC2005a,b) and power performance measurements (IEC 2005c).

2.1 Methodology

For the research question "How much does the acceptance and reliability of ground-based lidar in wind energy increase by reducing uncertainties in turbulence intensity predictions?" a theoretical framework could be built using concepts from several relevant areas.

2.1.1 Quantifying uncertainties in TI predictions

Perturbation theory is a mathematical framework that can be used to model the effects of small changes or perturbations on a system. It can be applied to understand how integrating perturbation theory contributes to reducing uncertainties in turbulence intensity predictions. Perturbation theory is the study of the effects of small disturbances [65]. The idea is to obtain an approximate solution to a mathematical problem by exploiting the presence of a small dimensionless parameter. In this project, the findings of A. Black [28] will be extended to fit an equation for turbulence intensity. Using these newly formed equations, uncertainties in TI can be quantified. This will help answer the question of to what extent perturbation theory can quantify uncertainties in turbulence intensity predictions using ground-based lidar.

2.1.2 Joint industry project implementation

There is a wind site available for the thesis project that has a flat terrain and is suitable for testing the findings of the joint industry project. As the wind site is already included in the JIP dataset, it can be assumed that the acceptance criteria will apply to the site, making it a reliable starting point for quantifying TI using JIP techniques. To implement insights for TI prediction in a flat wind site, the JIP report needs to be studied thoroughly and various findings need to be tested against the accessible wind site. If the wind site is not deemed acceptable, another site needs to be found in consultation with Vattenfall for the project to proceed.

2.1.3 Enhancing lidar acceptance

To answer the question, "To what extent does this research contribute to the enhanced acceptance of lidar in measuring turbulence in wind energy?", three academic theories have been identified to test the reliability and acceptance of ground-based lidar measurements.

Technology acceptance model (TAM): The TAM, developed in the field of information systems, can be applied to understand how users perceive and accept new technologies. In this context, it can help in assessing the acceptance of ground-based lidar technology within the wind energy sector. According to N. Marangunic

and Andrina Granic [66], the technology acceptance model poses that two variables, namely "perceived ease of use" and "perceived usefulness," play a mediating role in the intricate association between system characteristics (referred to as external variables) and the potential utilization of the system. Davis [67] explains the "actual use of the system" is a response to "user motivation", which itself is influenced by an "external stimulus". As is evident in Figure 7.1 in chapter 7, the user's motivation consists of three factors: "perceived usefulness", "perceived ease of use", and "attitude toward using". Whereas the parameters outside of the TAM box represent the system design characteristics. The setup in Figure 7.1 and the recommendations by G Hubner [68] can be used to set up a TAM for ground-based lidar systems, and therefore help with answering the question, which aspects of this research contribute to the enhanced acceptance of lidar in measuring turbulence in wind energy.

Innovation diffusion theory: This theory explores how innovations are adopted and spread within a social system [69]. It can provide insights into the factors influencing the adoption of integrating perturbation theory and recommended practices from a joint industry project in the wind energy sector. I. Sahin [70] goes over a detailed review of Rogers' diffusion of innovations theory. According to Rogers, an *innovation* is an idea that is perceived as new by an individual or organisation. In this innovation, an important obstacle is "uncertainty", which is of course a vital part of the research question of this thesis project. As said by Sahin: "to reduce the uncertainty of adopting the innovation, individuals should be informed about its advantages and disadvantages to make them aware of all its consequences".

Reliability theory: This part of the framework draws from engineering and systems reliability literature to assess the reliability of ground-based lidar technology. It achieves this by integrating perturbation theory and recommended practices. According to Alhmoud and Wang [71], reliability analysis can help to identify, classify and investigate several issues and concepts that arise in wind-energy systems. Combining the TAM, IDT, and reliability theory can help address the question of which aspects of this research will contribute to enhancing the acceptance and reliability of lidar in measuring turbulence.

2.2 Setup

This section outlines the practical elements of the research, detailing the laboratory analysis and field environments, collaborative efforts with industry partners, and the technical specifications of the experimental and computational methods employed. These aspects are crucial for effectively addressing the identified research questions.

2.2.1 Ground-based lidar deployment

The focus of the field study is the deployment of ground-based lidar systems at a wind farm site in the Netherlands, a location chosen in collaboration with Vattenfall. To validate and cross-check the data collected by lidar, cup anemometers will also be utilized. Over a twelve-month period, a complete set of data will be gathered to capture a wide range of weather conditions, this will include a two-month overlapping period for lidar and cup anemometer data collection.

2.2.2 Statistical analysis

For the statistical analysis of the research, Python will be utilized due to its application in various key data-related tasks. Python will be used for specific targeted processes that are crucial to the research, such as data filtering. This is essential for refining the dataset and ensuring that only relevant data points are being considered for analysis. The data from the flat terrain site, obtained from lidar and cup anemometer readings, will be imported into Python. Subsequently, the data can be filtered, and statistical analysis can be applied. Due to the lidar and cup anemometer measuring at different heights, interpolation techniques will be utilized to enhance the data. The lidar and cup measurements at the same height can be compared through the implementation of scatter plots, Bland-Altman [72] plots, wind roses, and error metrics. Additionally, a correlation study will be conducted to determine which parameters of data affect each other.

2.2.3 TI derivation and implementation

By utilizing perturbation theory, it is possible to develop a new formula for TI which is based on the existing formula ($\frac{\sigma}{\overline{u}}$). Once the data from the lidar is obtained, this new TI can be computed. It can then be evaluated against the error metrics specified in the JIP to determine if there is any improvement in the reliability of lidar measurements.

2.2.4 Machine learning

Based on the JIP recommended practice, lidar TI data can be adjusted with the help of a machine learning model if it falls outside the given error metrics range. However, due to the limited availability of overlapping data for this wind site, which is only two months, a machine-learning model is not a practical solution. To implement a machine learning model properly, a new site should be identified in collaboration with Vattenfall. However, it should be kept in mind that machine learning may not be the best technique for reducing lidar TI error, as stated in Newman's research [73].

2.2.5 Collaboration with industry

A key aspect of this research is the collaboration with industry partners, particularly the partnership with Vattenfall. This collaboration extends beyond only access to wind farm sites; it includes a wealth of industry expertise and resources. In addition to Vattenfall, the study will also integrate findings from the JIP, thereby ensuring that the research is grounded in practical industry standards and insights. For better understanding, the stakeholders of this project have been listed:

- *Vattenfall:* As a leading energy company, Vattenfall will provide critical access to operational wind farm sites and their associated data. They will also offer technical expertise and industry perspectives, particularly in the areas of wind energy operations and the practical challenges faced in turbulence measurement. Vattenfall's role will be crucial in providing a real-world context for the research, ensuring that the findings are relevant and applicable to current industry practices.
- *Joint industry project participants:* Companies involved in the JIP will contribute by sharing their findings, recommendations, and best practices. Their input will be useful in validating the research methodology and aligning the study with the latest industry developments.
- *Academic experts:* Collaboration with academic experts, particularly those specializing in wind energy and atmospheric sciences, like the Thesis supervisors, will bring a depth of theoretical knowledge to the project. Their role will involve advising on the research methodology, assisting in the interpretation of data, and ensuring that the study sticks to academic standards.

The research process will be structured to facilitate ongoing engagement with these stakeholders. Regular meetings will be organized to discuss progress, share findings, and solicit feedback. Vattenfall's expertise in wind farm operations will directly influence the field study design, ensuring that the data collection methods are practical and relevant to industry needs. The insights from JIP participants will be used to refine the methodology, making sure it aligns with industry challenges and priorities. Academic experts will play a key role in reviewing the findings and providing guidance on theoretical aspects, ensuring academic credibility.

2.3 Results and outcomes

The objective of this research is to enhance the understanding and application of lidar TI predictions in wind energy. To achieve this, wind park data provided by Vattenfall will be utilized, with a focus on the use of ground-based lidar. The study will explore the effectiveness of perturbation theory in quantifying uncertainties in TI predictions. To do this, innovative perturbation theory formulas for TI will be developed, based on mean wind speed equations. The aim is to enhance the potential of lidar in this field. Furthermore, the research will evaluate the JIP recommendations for the selection of new wind turbine sites in the Netherlands. Specifically, the study will examine their applicability and effectiveness in flat terrain conditions. The results of this evaluation are expected to provide insights that are not only specific to the Netherlands but also applicable to similar geographical contexts. In addition, the research will address the challenges of conducting wind research in complex terrain. This will involve assessing the necessary modifications and adaptations in current methodologies and technologies. This research aims to provide verifiable evidence to support the increased acceptance of lidar in turbulence measurements within the wind energy sector. The evidence is expected to be obtained through a detailed understanding of the uncertainties in TI predictions, which will be obtained using perturbation theory and newly developed TI formulas. The outcomes will be validated and verified through comparative analysis, benchmarking the new TI predictions against existing models and literature. To ensure the reliability of the findings, cross-validation methods will be employed to test the derived results with subsets of data. Additionally, collaborations with Vattenfall and academic experts will augment this process, alongside comprehensive statistical analyses to determine the significance of the findings. The research will address data analysis challenges such as the management of large datasets and incomplete data by using thorough data cleaning and validation

techniques. To process and analyze quantitative measurements, including wind speed, direction, and turbulence metrics, data analysis will be conducted. Furthermore, the research will employ comprehensive statistical analyses to determine the significance and reliability of the findings. In conclusion, the outcomes of this research are expected to contribute significantly to the fields of wind energy and remote sensing. By developing new methods and validating lidar technology for wind measurements, the research aims to enhance the accuracy and reliability of wind farm planning and operation, setting a foundation for future innovation in these areas.

2.4 Project planning

The project plan is divided into eight well-defined phases, as shown in Figure F.1 in Appendix F. The first phase will take place in November and December 2023 and involves introducing the thesis, including the kick-off and onboarding with Vattenfall. During this phase, the main focus points of the thesis will be discussed, and administrative documents with academia and the company will be arranged. The second phase will take place from November 2023 until the end of January 2024 and will involve an extensive literature review. This review will consist of writing a research proposal, exploring the theoretical background and state-of-the-art, and coming up with a problem setting. In January, the project will transition into the first research phase of the project, which will delve into the project framework. In this phase, the methodology of the project will be laid out, along with the theoretical framework and setup. The third phase will run in parallel with the fourth phase, both starting in January. The fourth phase will delve into data analysis, consisting of importing data from the chosen wind site, filtering the data, comparing the lidar and cup measurements, and performing statistical analysis. The fifth phase will run from January to April 2024 and will focus on exploiting the methodology. In this phase, the derivation and implementation of TI equation will be done. Using the results of this implementation, a TAM method will be set up, and the results will be analyzed. The core part of the sixth phase will start in April and run into May, and it will focus on the analytical writing for the project. However, it has been decided to start the analytical writing in December. This phase will include writing the results and outcomes. The seventh phase of the project will be the discussion phase. In this phase, the results of the thesis project will be discussed, a conclusion will be drawn, and a review of the work will be done. Based on feedback from industry and academia, the report will be further improved. The project planning will end with phase eight, which is the end of the thesis phase. This phase will be mostly presentation-oriented and will focus on the preparation and execution of the thesis defence. Once the thesis defence is concluded, the thesis project will conclude.

Chapter 3

Data analysis

This thesis project conducts a detailed analysis using data from a Vattenfall wind site in the southern Netherlands, classified as a "flat" terrain wind site by IEC standards. The research is placed in the context of DNV's joint industry project, emphasizing its relevance in industry collaborations. This chapter aims to clarify the data analysis process, comparing it with the JIP project findings. Adherence to IEC criteria ensures a methodically accurate approach for evaluating wind energy sites. The chapter outlines sequential processes for data refinement, including filtering, layering by height, and alignment by column names. Interpolation procedures address data misalignment, providing insights into the wind site's dynamic characteristics. The chapter also explores the integration of a machine-learning model, aligning with JIP recommendations. The initial section details the extraction of height information, and aligning datasets to facilitate comparisons. Subsequently, the nature of interpolating lidar data is explored, addressing height differentials and introducing the incorporation of an LSTM model, to enhance the precision of data outputs. The analysis then extends to the evaluation of results, with a specific emphasis on the TI parameter, resulting in an examination of various data processing methodologies. Additionally, the chapter employs statistical methods, encompassing wind direction, speed, and additional parameters.

3.1 Data filtering

The data has been saved in multiple folders on the Vattenfall servers. The met mast data is spread over multiple CSV (Comma Separated Value) files, while for the lidar data high frequency and 10-minute data is available. The first analysis will compare the 10-minute lidar data with 10-minute met mast data. As can be seen in Figure 3.1, the lidar and meteorological mast measurements did not happen at the same point in time. Two months of data are available for comparison. This data is filtered on height since the lidar and met mast measurements were conducted at different heights.

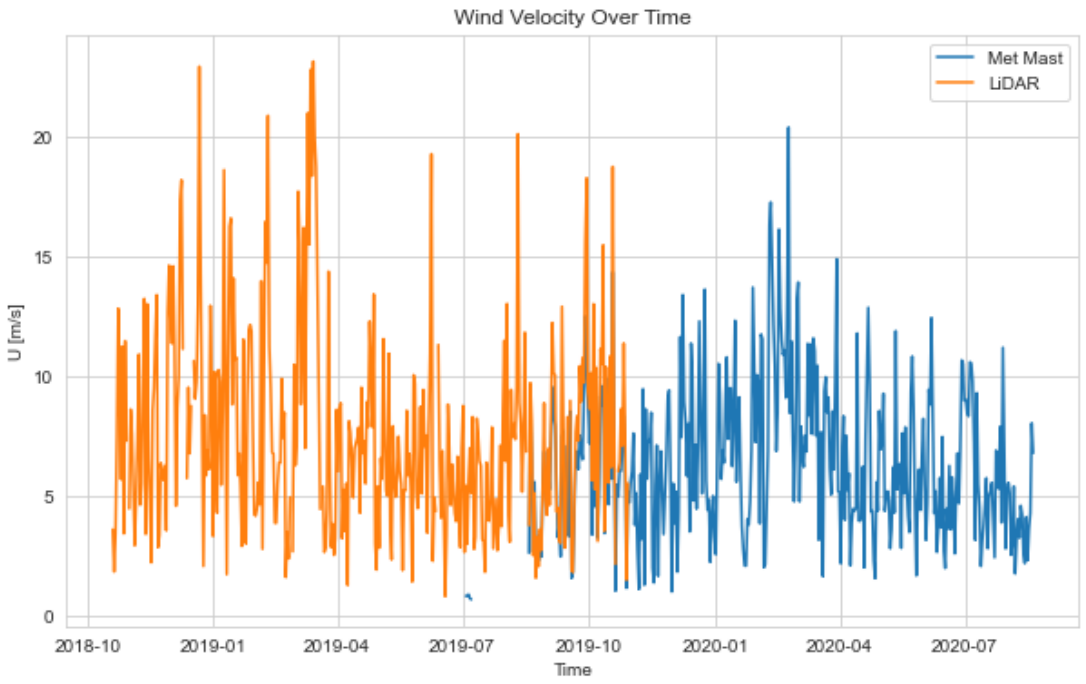

Figure 3.1: Lidar and met mast wind speed measurement campaign data over a time period between October 2018 and October 2020

Lidar data was collected at eleven distinct heights, ranging from 32 to 192 meters, while the meteorological mast data was recorded at seven heights between 55 and 120 meters. To facilitate a more accurate comparison between the two data sets, the lidar data was interpolated after extracting the height information. Additionally, a machine learning approach was employed to adjust the lidar height data to align more closely with the cup anemometer data. It was also observed that the cup anemometer data exhibited an incorrect wind direction, necessitating an adjustment to match the wind direction presented in Figure 3.2.

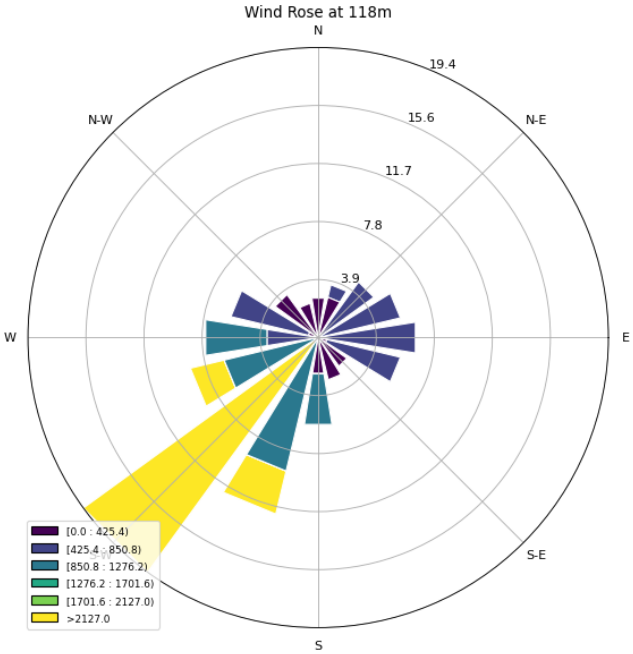

Figure 3.2: Windrose of the ZX lidar at the Vattenfall test site showing the binned wind direction at a height of 118 meters

3.1.1 Extracting height information

The lidar data was structured in a way that the rows contained the various values at various timestamps whereas the columns contained names such as "Wind Direction (deg) at 190m". It is therefore easy to extract the height

value and create multiple data frames based on height, which can then be stored in a list of data frames. The same is true for the met mast measurement, where again the rows give values per timestamp and the columns have names such as "A02VelCal (m/s) max". The met mast columns are labeled with A01 to A12, which stand for different heights, for example, A01 stands for a height of 123 meters whereas A12 shows the values for a height of 56.3 meters. The met mast heights will also be taken out and used to create different data frames that can be stored in a list of data frames. The columns of both lidar and met mast data are then renamed to match one another. Now the lidar data can be coupled to the closest met mast data, and either be interpolated or the data can be kept the same. As is evident in Table 3.1, the meteorological mast only has 6 different measurement heights, whereas the lidar has 11 different measurement heights. Looking at the difference column, the analysis should focus on the heights with the least amount of difference, therefore the analysis should focus on the heights between 82 and 122 meters.

Lidar height	**Closest cup height**	**Difference (%)**
38m	55.8m	46.84
46m	55.8m	21.30
64m	71.3m	11.41
82m	86.3m	5.24
100m	101.3m	1.30
118m	118.2m	0.17
122m	123m	0.82
136m	123m	−9.56
154m	123m	−20.13
172m	123m	−28.49
190m	123m	−35.26

Table 3.1: Data heights for both lidar and cup anemometer measurements including difference in height percentages

3.1.2 Interpolating lidar data

Since some of the met mast heights differ significantly from the lidar heights, interpolating the data seems necessary. Linear interpolation is a mathematical technique used to estimate unknown values within the range of a discrete set of known data points. By applying formulas or functions that best fit the known heights, interpolation predicts values at intermediate positions with a reasonable degree of accuracy. This method is essential since precise estimates between measured points are necessary. Another option would be to shear the data, however, interpolation is preferable to shearing when the goal is to fill in gaps or estimate values between the known heights because it maintains the integrity and continuity of the data. Shearing, on the other hand, distorts the data by shifting parts of it in a non-uniform manner, making it unsuitable for tasks requiring accurate data reconstruction or estimation between points. The method of interpolation used can be found in section A.1.

3.1.3 Machine learning model

As can be read in the JIP report, to reduce uncertainties in lidar TI measurements, using a machine learning (ML) model to alter the lidar data was recommended. In this project, it was opted to train a Long Short-Term Memory (LSTM) model on the lidar data. Utilizing an LSTM machine learning model for modifying lidar data to mitigate uncertainties presents both merits and challenges. LSTMs excel in capturing temporal dependencies and learning intricate patterns over time, aligning well with the sequential nature of lidar measurements. They can autonomously derive relevant features from the data, potentially aiding in uncertainty reduction. However, the complexity of LSTMs may demand substantial computational resources, and the risk of overfitting needs careful management through proper regularization and representative training datasets. Furthermore, the interpretability of the model could be limited, and if the input lidar data contains inherent inaccuracies, the model might inadvertently perpetuate or exacerbate uncertainties. Since the overlapping data between the met mast and lidar is only two months, it was evident that this period was not long enough, since the LSTM model could not properly alter the lidar data, as can be seen in Figure F.2. As is clear in section 3.2, the usage of an ML model was not found useful for the implementation at this Vattenfall wind site.

3.2 Analysis of results

To have a clear view of the data measured from the wind site, the project needs to involve a proper data analysis. This section will go over the comparison between the un-interpolated, interpolated, and ML-adjusted data sets in subsection 3.2.1. After which, it will take a look at the error metrics in subsection 3.2.2, which are vital as seen in the JIP report.

3.2.1 Data comparison

The first part of the analysis of results is the data comparison. Data comparison is vital to understanding the impact of interpolating data and using an ML model to alter lidar data. This comparison will focus solely on the TI parameter, whereas section 3.3 will go over more parameters available from the lidar measurements. The TI data comparison comprises a study of the TI distribution, a comparison between lidar and met mast measurements, a visual comparison between TI wind roses, and a study of the TI error metrics.

Distribution of TI values

Analysing the distribution of TI values is crucial during the data comparison phase. Turbulence intensity directly impacts wind turbine performance, affecting loads on turbine components. By examining the distribution of TI values, one can assess the wind's impact on turbine operation and identify optimal siting conditions within design limits. The TI distribution also plays a role in predicting energy production accurately, as higher turbulence can lead to increased aerodynamic losses. This is due to the TI affecting the REWS, mentioned in subsection 1.1.5, consequently affecting wind turbines' power performance [74]. Moreover, comparing the TI distribution between lidar-derived wind data and met mast data aids in detecting discrepancies, ensuring data consistency, and revealing potential calibration issues. Understanding the local wind characteristics through TI distributions is essential for making informed decisions in wind energy projects and ensures the reliability and suitability of the wind resource for energy production.

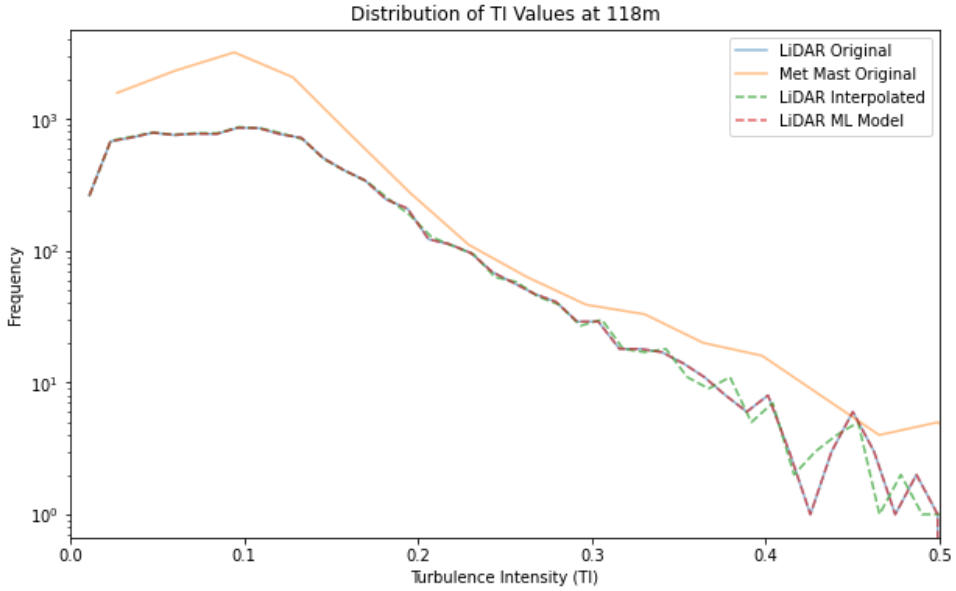

Figure 3.3: Frequency of lidar measured TI values after several data adjustment techniques compared with the frequency of met mast measured TI values at a measuring height of 118 meters

As can be seen in Figure 3.3 and Figure 3.4, except for the "Met Mast Original" frequencies, the TI frequencies follow a similar trend. A TI value between 0.1 and 0.15 is most common for this wind site. As is evident in Figure 3.3 andFigure 3.4, the interpolating or adjusting through ML is not affecting the frequency in TI values significantly. The interpolation has a better effect when the difference between heights is larger. However, the method of interpolation means that a meteorological mast is always needed at the site, whereas this is the expense that lidar should replace. Instead of interpolation, lidar data should have noise removal, as discussed by Newmann and Clifton [50]. The interpolation that should happen, according to this paper, is interpolating to a grid with constant temporal spacing, which leads to the frequency resolution of the measurements being constant.

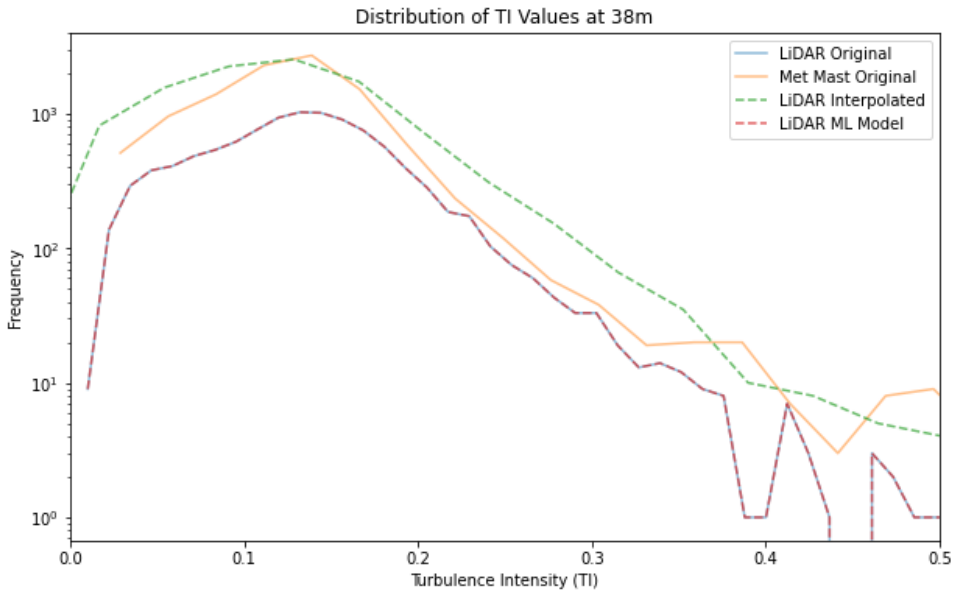

Figure 3.4: Frequency of lidar measured TI values after several data adjustment techniques compared with the frequency of met mast measured TI values at a measuring height of 38 meters

Noise spike filter

As mentioned before, to do a proper analysis of the results, a noise filter is necessary. Therefore it was chosen to preprocess the data by implementing a spike filter based on a paper by Vickers and Mahrt [75], where "*any point in the window that is more than 3.5 standard deviations from the window mean is considered a spike*". Using this, the spikes in TI predictions can be removed from the dataset and a proper comparison between the lidar and the met mast can be conducted.

Lidar / met mast comparison

As said in chapter 1, various literature papers have looked at the differences between lidar and met mast measurements. As said by Sathe and Mann [14], cup anemometers measure at a point, which means that, if the device is set up properly, standard procedures can be used to get the turbulence information from the wind. A lidar, however, measures at different points in a large volume, which causes a challenge in working out the turbulence information. Next to that, as mentioned by Newmann and Clifton [50], lidar data needs to be preprocessed with a noise filter. To properly compare lidar and met mast TI measurements, it was opted to visualise the difference using scatter plots. As is clear in Figure 3.5, the TI values between lidar and met mast are quite different, even though they follow the trend line of an ideal match. As is known from the literature [14], lidar is prone to overpredict TI values, therefore more values can be spotted on the right-hand side (RHS) of the ideal match. As the overpredicting of the lidar is not notably clear in this figure, it has also opted to show a Bland-Altman plot and wind roses later in the data comparison. In general, the different datasets align, as can also be seen in Figure 3.6, when we solely look at TI values below a value of 0.4. It is also evident, that at higher values of TI (above 0.2) the agreement is a lot lower than at lower values of TI.

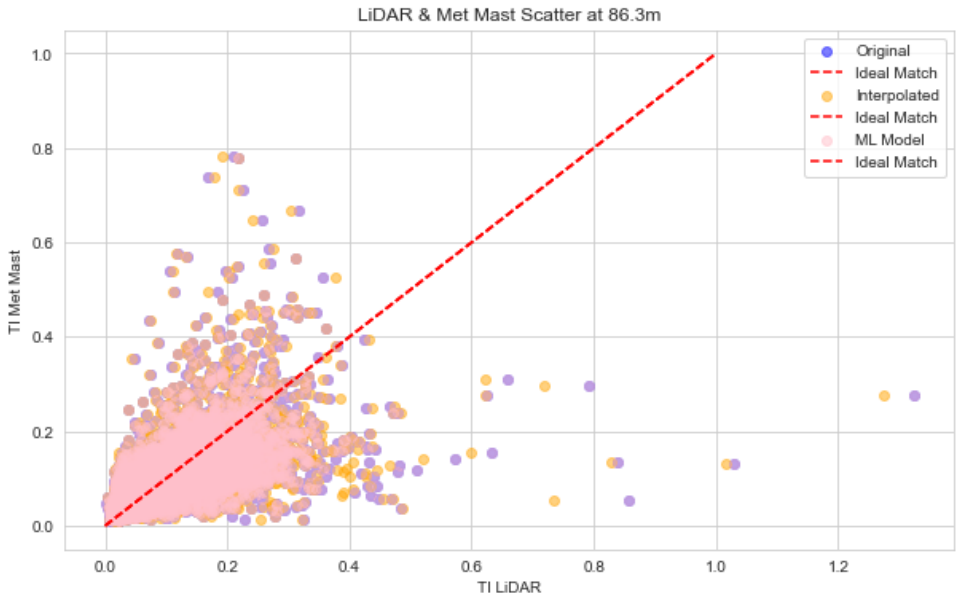

Figure 3.5: Scatter plot comparison between lidar and met mast TI for various lidar alterations

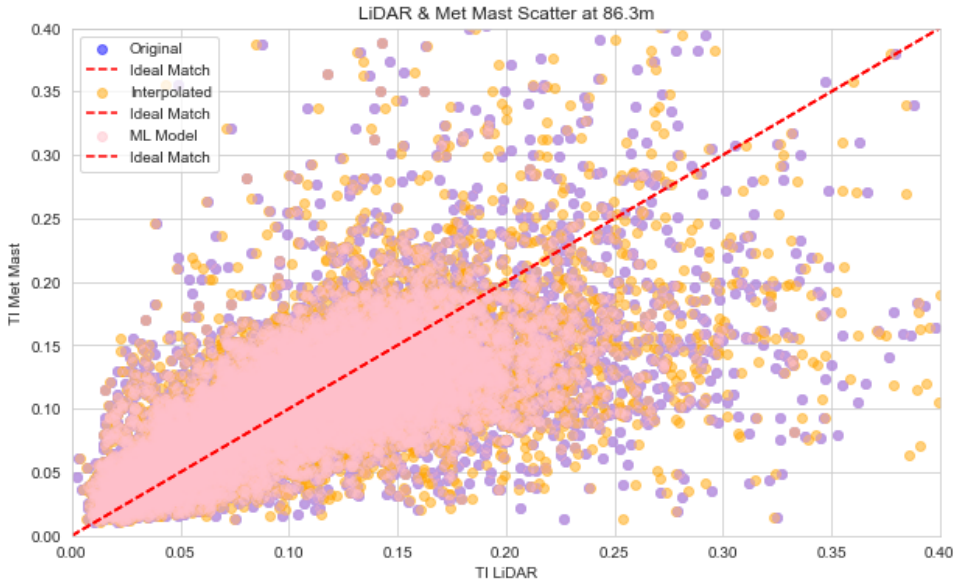

Figure 3.6: Scatter plot comparison between lidar and met mast TI for various lidar alterations with x limit of [0.0 , 0.4]

The Bland-Altman plot, in Figure 3.7 and Figure 3.8, serves as a valuable graphical tool for assessing the agreement between lidar and met mast measurements. It presents the difference between measurements on the y-axis against their average on the x-axis. The plot helps identify any systematic bias, revealing if one method consistently produces higher or lower values than the other. The mean difference and limits of agreement, which are calculated as 1.96 times the standard deviation of differences, offer insights into the overall agreement and variability between methods. After calculation, it turned out that around 4.5% of the measurements fall outside of the limits of agreement (LoA). From this 4.5%, around 2.9% was due to lidar overprediction, meaning the measurement was above the upper LoA, whereas around 1.6% was due to Met Mast overprediction, complying with the measurement point being below the lower LoA.

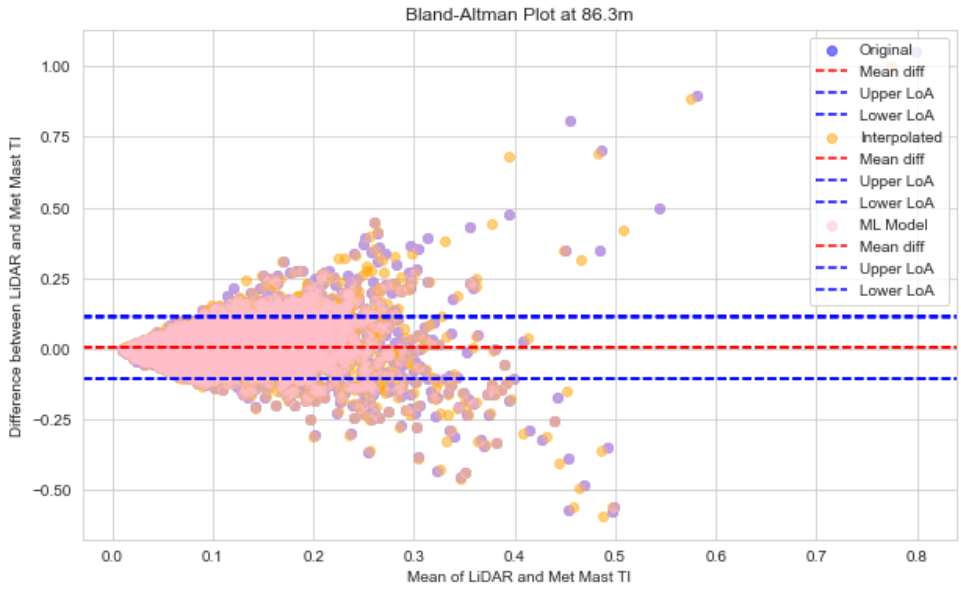

Figure 3.7: Bland-Altman plot showing the difference between the original, interpolated, and ML-adjusted lidar data

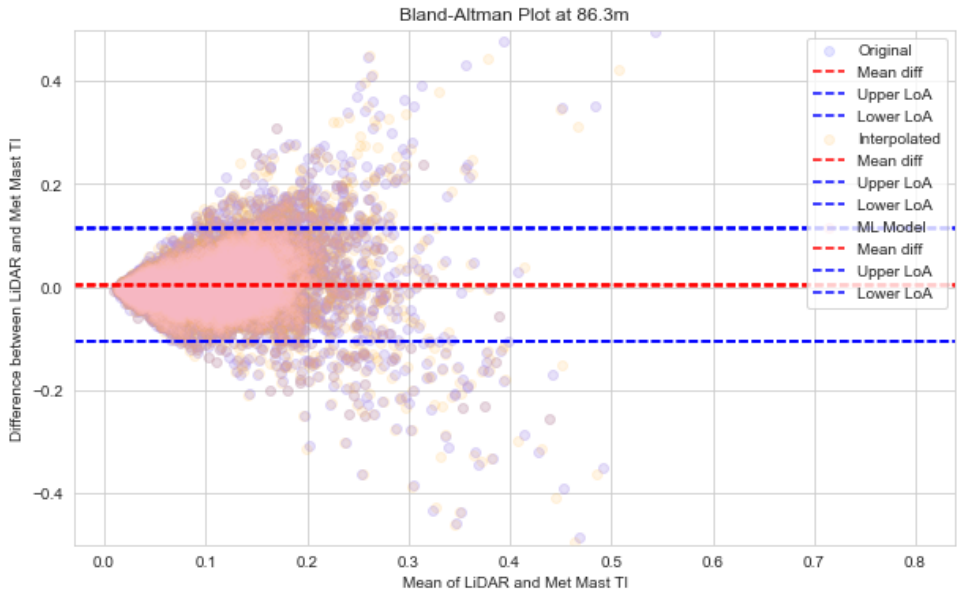

Figure 3.8: Bland-Altman plot showing the difference between the original, interpolated, and ML-adjusted lidar data utilizing a y limit of [-0.5 , 0.5]

TI wind roses

As previously shown in the Bland-Altman plots, the lidar slightly overpredicts the TI values compared to the met mast. To better understand this overprediction, it was decided to create wind roses for turbulence intensity. The first thing that becomes clear from Figure 3.9a is the fact that the met mast significantly overpredicts the TI value in the wind direction of zero degrees. The mast installation report shows the area surrounding the mast, as can be seen in Figure F.4. The surrounding area in the 0° north direction does not have significantly more buildings and trees. Therefore this TI overprediction could be due to the tower. When looking at the met mast picture in Figure F.5, it seems that this picture corresponds with the 270°(W) direction, which would mean that the 0° north wind would come from the right side of the picture. This means that the large influx in TI for the north direction cannot be due to the beam of the met mast tower, since this would play a bigger role for the NW direction.

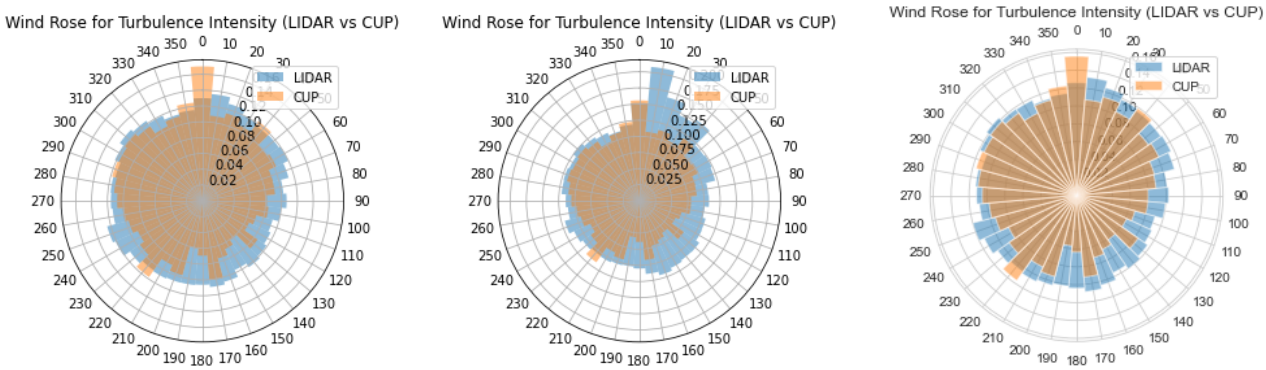

(a) Uninterpolated Wind Rose (b) Interpolated Wind Rose (c) Machine Learning Wind Rose

Figure 3.9: Comparison of TI rose plots showing TI influx in the North direction

3.2.2 Error metrics

In the evaluation of lidar data compared to met mast data using various error metrics, an intriguing observation emerges concerning the performance of different methodologies. The error metrics considered, including Root Mean Square Error (RMSE), Mean Absolute Error (MAE), and Mean Squared Error (MSE), serve as quantitative indicators of the disparities between lidar and met mast data. A detailed examination across distinct wind speed bins, each spanning 2 m/s, was carried out to assess the efficacy of three datasets: Interpolated data, ML data, and the original lidar data. The primary objective was to indicate the accuracy of these datasets under varying wind conditions and identify any potential improvements or setbacks introduced by the applied methodologies. Surprisingly, the ML data exhibits a close resemblance to the original lidar data. While this alignment might initially seem positive, it raises concerns about the effectiveness of the ML model, which was implemented to minimize error metrics. The unexpected similarity suggests that the ML model may not have successfully achieved its intended purpose, potentially due to the constraints of a limited training dataset spanning only two months. This underscores the importance of ensuring an adequately diverse and representative training dataset for machine learning models to effectively generalize across various wind speeds. Similarly, the interpolated data, designed to mitigate errors, presents a contrasting pattern. Notably, this method introduces larger errors at lower wind speeds, which is counterintuitive to its intended purpose of reducing discrepancies between lidar and met mast data.

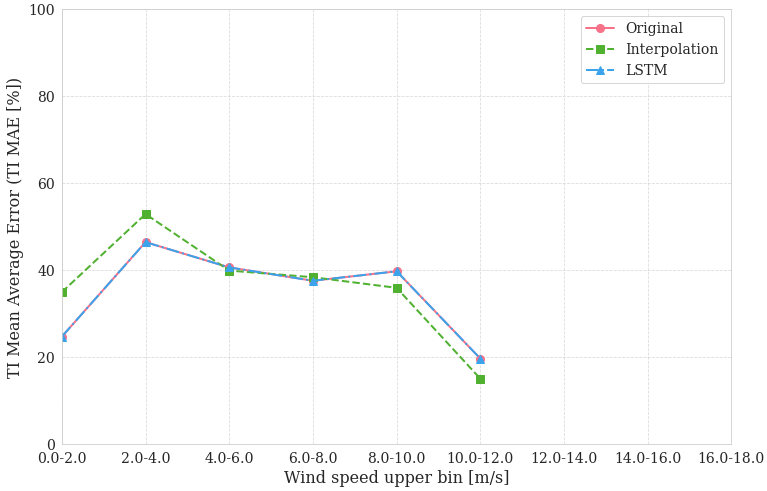

Figure 3.10: MAE graph showing the difference when interpolating lidar data

The MAE is the simplest regression error metric to understand. We'll calculate the residual for every data point, taking only the absolute value of each so that negative and positive residuals do not cancel out. We then take the average of all these residuals. Effectively, MAE describes the typical magnitude of the residuals. In Equation 3.1, y is the actual output value, whereas $\hat{y}$ is the predicted output value, which together create the absolute value of the residual.

$$MAE = \frac{1}{n}\Sigma\,|y - \hat{y}| \tag{3.1}$$

$$MSE = \frac{1}{n}\Sigma\left(y - \hat{y}\right)^2 \tag{3.2}$$

$$RMSE = \frac{1}{n}\sqrt{\Sigma\left(y - \hat{y}\right)^2} \tag{3.3}$$

The MSE is just like the MAE but squares the difference before summing them all instead of using the absolute value. We can see this difference in the equation below. Because we are squaring the difference, the MSE will almost always be bigger than the MAE. For this reason, we cannot directly compare the MAE to the MSE. The RMSE is the square root of the MSE.

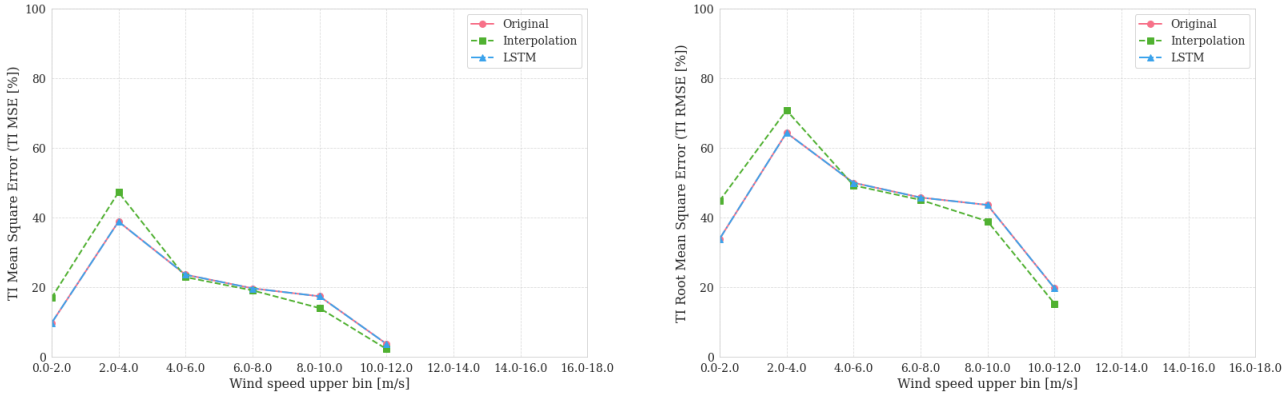

(a) Mean Squared Error

(b) Root Mean Square Error

Figure 3.11: Error metrics showing the difference between the original, interpolated, and ML-adjusted lidar data

3.3 Statistical analysis

In this section, a comprehensive statistical analysis of lidar data is conducted. Various parameters beyond TI will be explored to show relationships among different variables such as wind direction, wind speed, and height. The section will begin with correlation analysis, investigating how wind direction and speed correlate with TI and height, with a specific focus on the 86.1-meter height. This analysis will help identify any significant patterns or anomalies in the data, providing insights into the relationships between these variables. Subsequently, the section moves on to regression analysis. Both linear regression and random forest techniques will be employed to model and predict the relationships between the variables. By comparing these methods, the aim is to determine which model best captures the underlying patterns in the data.

3.3.1 Correlation analysis

After solely focusing on the TI parameter, it is time to zoom out and take a look at other parameters for the lidar data. This statistical analysis will compare the wind direction and speed parameters with TI and height. For part of this study, a single height (86.1 meters) will be taken out of the data frame to also analyze the data at a specific height. Figure 3.12 shows the data correlation at a height of 86.1 meters. The wind direction does not significantly influence the TI, even though subsection 3.2.1 showed a significant increase at the wind direction of 0°. It can also be seen that the TI increases with decreasing wind speed, which makes sense since TI is a function of the standard deviation and the mean wind speed, and it can be seen that this relation of $\frac{U_{sigma}}{U_{mean}}$ decreases with increasing wind speed.

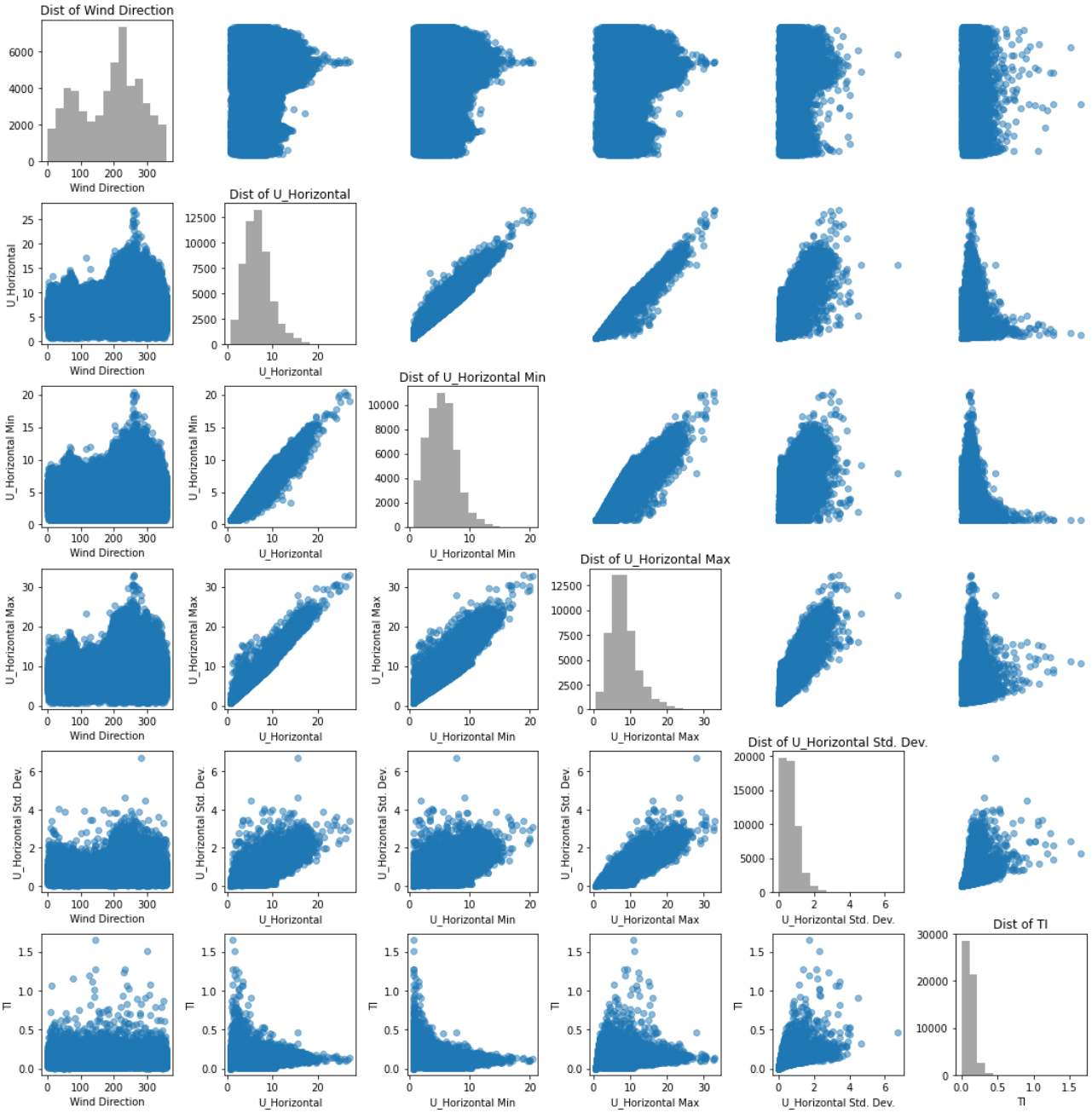

Figure 3.12: Data correlation at height 86.1m

A correlation heatmap is a graphical representation that displays the correlation coefficients between multiple variables in a dataset. Each cell on the heatmap shows the correlation value between two variables, using a colour scale to represent the strength and direction of the relationship. Positive correlations are indicated by one colour spectrum, while negative correlations are shown with another, allowing for an intuitive visual interpretation of how variables relate to one another. The intensity of the colour corresponds to the magnitude of the correlation coefficient, making it easy to identify strong, moderate, or weak relationships at a glance. Figure 3.13 shows results as expected, the wind direction slightly correlates with wind speed, while it does not correlate with TI. The TI is mostly dependent on the standard deviation, which makes sense, knowing that TI is a function of the standard deviation.

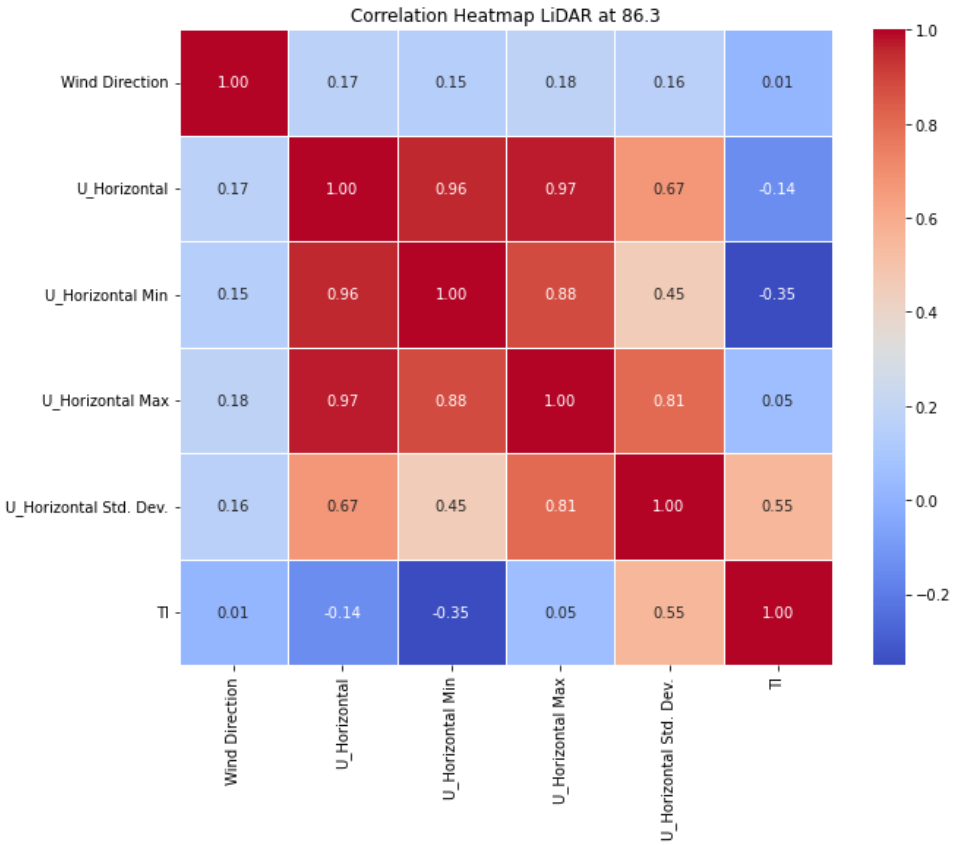

Figure 3.13: Correlation heatmap at height 86.1m

3.3.2 Regression analysis

Linear regression

Linear regression analysis is used to find the correlations between two or more variables [76]. It is a modeling technique used for analyzing data to make predictions [77]. Linear regression fits a straight line through the data and therefore expects a linear relationship between variables. For comparing lidar data with cup anemometer data, a perfect linear regression would mean that both data sets give the same values for TI over two months. The linear regression analysis can therefore show is the lidar is more prone to overpredict or underpredict the TI value when compared with the cup anemometer prediction. This means that the linear regression in Figure 3.14 closely resembles Figure 3.5. However, whereas Figure 3.5 just plots a linear regression line, Figure 3.14 makes use of a machine learning way of linear regression. Here the LinearRegression package in scikit-learn [78] is used. This package works by fitting a linear model to the relationship between a dependent variable and one or more independent variables. It uses the least squares method (explained by Bjorck [79]) to find the best-fitting line by minimizing the sum of the squares of the differences between the observed and predicted values. Once the model is trained using the fit method, it can predict new values.

Random forest

Random forest is a regression model. According to Bulaevskaya *et al* [80], random forest uses an ensemble of regression trees, and the predictions of these different trees are averaged to obtain a final prediction. A tree is created by sampling from the training data and selecting a random sample of the predictors at each node of the tree, which is similar to the method used in a neural network. Although section 3.1 explained that the use of machine learning for this site was not favored due to the limited two months of overlapping data, the random forest regression was still evaluated because the method is easy to understand, as seen in previous applications [50] [80] [81].

Regression between lidar and met mast

A linear regression plot visualizes the relationship between the independent variable(s) and the dependent variable linearly. It illustrates the fitted linear model, representing the best-fitting straight line that minimizes the sum of squared differences between observed and predicted values. The slope and intercept of this line

provide insights into the strength and direction of the relationship. On the other hand, a random forest plot portrays the predictions generated by an ensemble of decision trees. Each point on the plot represents an observation's actual value against its predicted value by the random forest model. This plot offers an overview of the model's ability to capture complex patterns and interactions within the data, showcasing the aggregated predictive power of multiple decision trees. As shown in Figure 3.14, the lidar data (*Predicted*) does not have a great linear regression with the met mast data (*Actual*). However, it does have a great random forest correlation.

The data shows a strong correlation in a random forest model, indicating a complex and nonlinear relationship between the independent and dependent variables. In a random forest model, which consists of multiple decision trees, the algorithm can effectively capture intricate interactions and patterns within the data. This flexibility allows the random forest to excel at modeling nonlinearity and capturing complex relationships that may be difficult for a linear regression model to represent accurately. On the other hand, linear regression assumes a linear relationship between the variables by fitting a straight line to the data. When this assumption doesn't hold, as indicated by a weaker correlation in the linear regression model, it highlights the limitations of linear models in capturing the inherent complexity of the underlying data structure. In such cases, using nonlinear models or exploring more advanced modeling techniques may be necessary to improve predictive performance and better reflect the true nature of the data. Newman and Clifton [73] show that using a trained random forest at the end of the adjustment method could improve the results. The use of random forest seems promising for adjusting the lidar TI predictions. However, in this case, met mast data was needed for this adjustment. The purpose of this adjustment is to ensure that the lidar can function effectively on its own.

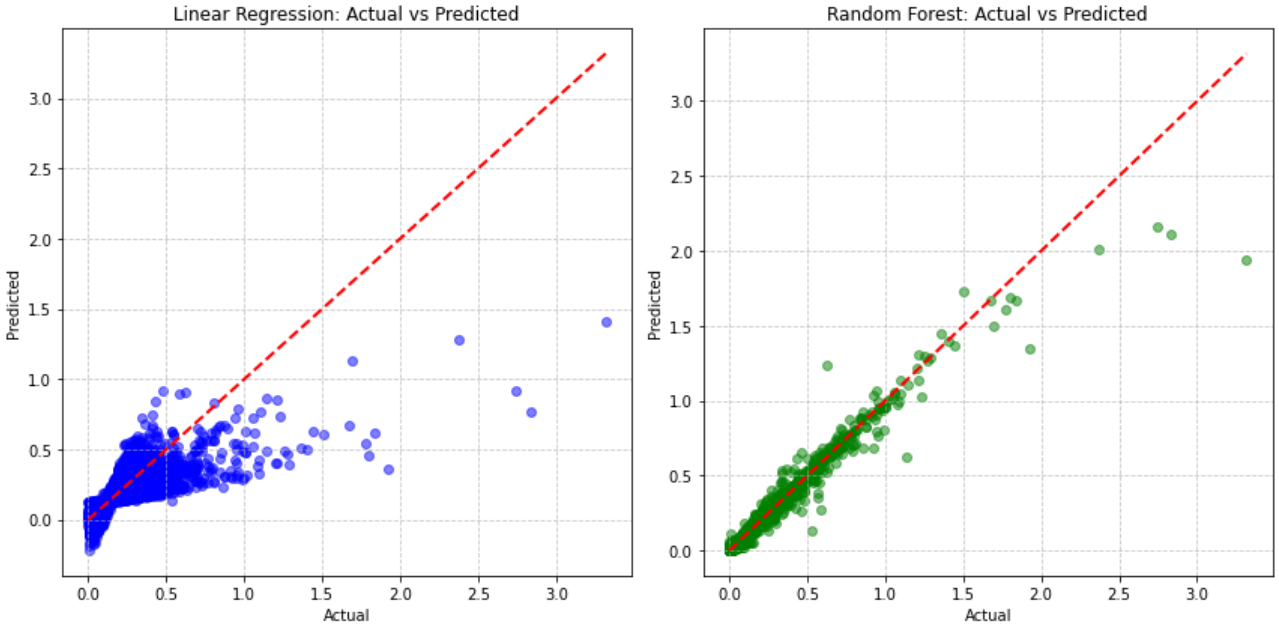

Figure 3.14: Linear Regression and Random Forest Regression for lidar TI data

Chapter 4

Derivation of CW-lidar TI equations using perturbation theory

Perturbation theory comprises methods for finding an approximate solution to a problem, by starting from the exact solution of a related, simpler problem. It's particularly useful in systems where a small parameter, the "perturbation", slightly alters a known, solvable problem. The idea is to start with a simple, solvable problem and then incrementally adjust the solution to account for the effects of the perturbation. The methodology of perturbation theory encompasses a systematic approach for solving complex mathematical problems by introducing a small parameter, typically denoted as ϵ, to facilitate the analysis. The first step in perturbation theory involves obtaining the unperturbed solution, which is achieved by solving the problem without considering the perturbing influence. This initial solution serves as the zeroth-order approximation. Subsequently, the analysis proceeds to the first-order perturbation, where the first-order correction, involving the first power of ϵ, is calculated. This correction refines the accuracy of the solution. If required, higher-order corrections, such as second-order, third-order, and so forth, are computed, each involving higher powers of ϵ and providing increasingly precise approximations. The culmination of the perturbation series involves summing these corrections to the unperturbed solution, yielding an approximate solution to the original problem. This stepwise progression through unperturbed, first-order, and higher-order corrections constitutes a comprehensive approach in perturbation theory for tackling intricate mathematical challenges.

4.1 Derivation theory

Before deriving the continuous-wave turbulence intensity equations of the ground-based lidar, it's important to establish some foundational theoretical principles that will be utilized in the derivation process. This section will cover the theory of time averaging, Reynolds decomposition, Jensen's inequality, binomial approximation, and the pseudo-inverse matrix.

Time averaging

Time averaging is a method employed to minimize the fluctuation in error present in the raw high-frequency measurements obtained from the lidar [30]. It involves calculating the average of a set of data points over a specified period. This method is particularly useful for analyzing wind speeds, where instantaneous measurements can vary significantly due to turbulence. As said by Sumer and Fuhrman [27], the mean value of wind speed can be defined as:

$$\overline{U_i} = \frac{1}{T}\int_{t_0}^{t_0+T} U_i dt \tag{4.1}$$

where U_i is the wind speed, T is the time over which the mean is taken, and t_0 is any arbitrary time.

Reynolds decomposition

In perturbation theory, Reynolds decomposition allows for the decomposition of the wind velocity field. Reynolds decomposition is a mathematical technique used to separate the expectation value of a quantity from its fluctuations [27].

$$u = \overline{u} + u' \tag{4.2}$$

The expected value, $\overline{u}$, is often found from an ensemble average which is an average taken over multiple experiments under identical conditions. For Reynolds decomposition, relations between two quantities have been set up. These Reynolds conditions can be found in section B.1. The Reynolds decomposition is a useful technique to simplify the governing equations of fluid dynamics. The flow of wind around turbine blades is governed by the Navier-Stokes equations, which are inherently complex due to turbulence and nonlinearity. To make it simpler, the Reynolds-averaged Navier-Stokes (RANS) equations have been introduced, which use time-averaged equations of motion to model these flows. This is achieved through Reynolds decomposition, which decomposes the flow variables into mean and fluctuating components. The resulting RANS equations are more manageable as they focus on the time-averaged effects of the turbulent flow, making it easier to analyze fluid dynamics around turbine blades.

$$\rho\overline{u}_j\frac{\delta\overline{u}_i}{\delta x_j} = \rho\overline{f}_i + \frac{\delta}{\delta x_j}\left[-\overline{p}\delta_{ij} + \mu\left(\frac{\delta\overline{u}_i}{\delta x_j} + \frac{\delta\overline{u}_j}{\delta x_i}\right) - \rho\overline{u_i'u_j'}\right] \tag{4.3}$$

Jensen's inequality

Jensens's inequality, Equation 4.4, is a probabilistic inequality that concerns the expected value of convex and concave transformations of a random variable [82]. Jensen's inequality plays a crucial role in the derivation of TI equations by establishing relationships between the expectations of certain functions and functions of expectations. In the context of this study, this inequality will be employed to analyze the statistical characteristics of the flow field, providing valuable insights into the behavior of turbulence. Applying Jensen's inequality to turbulence-related variables allows us to examine the expected values under different scenarios, providing a foundation for understanding the variability in turbulence intensity predictions.

$$\phi(E[X]) \leq E[\phi(X)] \tag{4.4}$$

Binomial approximation

Binomial approximation is a powerful mathematical tool employed to simplify complex probability distributions, particularly in scenarios involving repeated, independent events [83]. In the derivation of TI equations, the binomial approximation will be harnessed to streamline the representation of turbulent fluctuations. binomial approximation enhances our ability to model turbulence, offering a concise representation of the stochastic processes involved. By applying binomial approximation to relevant variables, we aim to derive more tractable expressions for turbulence intensity. Equation 4.5 can be improved by adding Taylor series terms, as is done in Equation 4.6. In the derivation done by Black [28], the binomial approximation in Equation 4.6 is used until the second-order term.

$$(1+x)^n \approx 1 + nx \quad \text{for small } x \tag{4.5}$$

$$(1+x)^n = 1 + nx + \frac{n(n-1)x^2}{2} + \frac{n(n-1)(n-2)x^3}{6} + \frac{n(n-1)(n-2)(n-3)x^4}{24} + ... \tag{4.6}$$

Pseudo-inverse matrix

A pseudo-inverse matrix is a generalization of the inverse of a square, invertible matrix to arbitrary matrices [84]. It is also known as the Moore-Penrose inverse. The pseudo-inverse can be computed using the singular value decomposition (SVD) of a matrix [85]. The SVD of a matrix A is defined as $A = U\sum V^T$, where U and V are orthogonal matrices and $\sum$ is a diagonal matrix containing the singular values of A. The pseudo-inverse of A can be expressed as $A^+ = V\sum^+ UT$, where $\sum^+$ is the diagonal matrix containing the reciprocals of the non-zero singular values of A. The pseudo-inverse has many useful properties, such as being a left inverse of A if A has full column rank, and a right inverse of A if A has full row rank.

4.2 Perturbation method for mean wind speed

For a horizontal wind speed, an anemometer is put in a flat, turbulent flow. For this case Rosenbusch ([29]) and Robey ([30]) use 2nd-order Taylor series expansion. However, this solution gets quite clumsy in more complex flows. Therefore the perturbation method is proposed as a solution by Black [28]. This results in Equation 4.7, the derivation for which can be found in Appendix D.

$$\overline{U_{scalar}} = U_{vector} + \frac{1}{2U_{vector}}\overline{\left|\left|\overrightarrow{U'}\right|\right|_2^2 sin^2\theta} \tag{4.7}$$

This result is identical to the 2nd-order Taylor expansion demonstrated in the literature.

According to Black *et al* [86], the time-averages of the 1 Hz reconstructions of lidar and cup anemometer scalar averages generate a bias relative to vector averages due to Jensen's inequality, which was explained in section 4.1. Due to the Euclidian norm of the u- and v-components of the wind being a convex function, the scalar averages will overestimate the corresponding vector averaging. section A.2 shows the proof that the Euclidian norm is a convex function, as well as an explanation for this norm.

$$U_{scalar} = \frac{1}{N}\sum_{i=1}^{N} ||PA^{+}v_r||_{2,i} = \sqrt{\mathbf{u}^2 + \mathbf{v}^2} \tag{4.8}$$

$$U_{vector} = ||PA^{+}\overline{v_r}||_2 = \sqrt{\overline{u}^2 + \overline{v}^2} \tag{4.9}$$

In Equation 4.7, a relation can be seen between U_{scalar} and U_{vector}. Here, U_{scalar} comes from scalar averaging, which is done by cup anemometers. As said by Black [28], this deals with the reconstruct-then-average approach, whereas U_{vector} comes from the average-then-reconstruct approach, known as vector averaging. In Equation 4.8 and Equation 4.9, P is the weighting matrix for using horizontal components, A^{+} is the pseudo-inverse matrix, explained in section 4.1, and v_r is the radial velocity.

3D Anemometer in flat, turbulent flow

It is shown by Black [28], that if we want to expand the previously found equation, it is helpful to write the 2D equation differently (Equation 4.10). Since there is no difference in the vector measurements of 2D and 3D, the same formula can now be used (Equation 4.11). It can be seen that the scalar averaging sensitivity term is the sum of the element-wise product ($\circ$) of the Reynolds stress tensor (τ_{ij}), the Scalar inflation tensor (γ_{ij}), and the lateral wind direction fluctuation ($sin^2\theta$). This is then normalized by $\frac{1}{2}$ of the vector average wind speed. The sensitivity of a 3D scalar measurement is different than 2D in the fact that now the w'^2 component is included and $sin^2\theta$ now includes fluctuations in 3D. Note that the difference between Equation 4.10 and Equation 4.11 can be seen in the right-bottom corner of the first matrix, where '0' gives 2D-turbulence due to multiplying the w components with '0', and '1' gives 3D-turbulence due to multiplying the w components with '1'.

$$U_{scalar} = U_{vector} + \frac{1}{2U_{vector}}\sum_{i,j=1}^{3}\begin{bmatrix}1&0&0\\0&1&0\\0&0&0\end{bmatrix} \circ \overline{\begin{bmatrix}\overline{u'^2}&\overline{u'v'}&\overline{u'w'}\\\overline{v'u'}&\overline{v'^2}&\overline{v'w'}\\\overline{w'u'}&\overline{w'v'}&\overline{w'^2}\end{bmatrix} sin^2\theta} \tag{4.10}$$

$$U_{scalar} = U_{vector} + \frac{1}{2U_{vector}}\sum_{i,j=1}^{3}\begin{bmatrix}1&0&0\\0&1&0\\0&0&1\end{bmatrix} \circ \overline{\begin{bmatrix}\overline{u'^2}&\overline{u'v'}&\overline{u'w'}\\\overline{v'u'}&\overline{v'^2}&\overline{v'w'}\\\overline{w'u'}&\overline{w'v'}&\overline{w'^2}\end{bmatrix} sin^2\theta} \tag{4.11}$$

Anemometer in inclined, turbulent flow

Then Black [28] rewrites the equation to be valid for an inclined flow, it is necessary to introduce an arbitrary tilt (θ_y) to the wind reference frame along the u-axis with SO(3) group. This leads to Equation 4.12.

$$\begin{bmatrix}cos(\theta_y)&0&sin(\theta_y)\\0&1&0\\-sin(\theta_y)&0&cos(\theta_y)\end{bmatrix}\begin{bmatrix}\overline{u}+u'\\\overline{v}+v'\\w'\end{bmatrix} = \begin{bmatrix}cos(\theta_y)(\overline{u}+u')+sin(\theta_y)w'\\\overline{v}+v'\\-sin(\theta_y)(\overline{u}+u')+cos(\theta_y)w'\end{bmatrix} = \begin{bmatrix}cos(\theta_y)\overline{u}\\\overline{v}\\-sin(\theta_y)\overline{u}\end{bmatrix} + \begin{bmatrix}cos(\theta_y)u'+sin(\theta_y)w'\\v'\\-sin(\theta_y)u'+cos(\theta_y)w'\end{bmatrix} \tag{4.12}$$

After expressing the l_2 norm of the **u-** and **v-**components with: $U_{scalar,1Hz} = \sqrt{(cos\theta_y(\overline{u}+u')+sin\theta_y w')^2 + (\overline{v}+v')^2}$, Equation 4.13 can be given (where ϵ is the combination of fluctuation terms after Reynolds Decomposition).

$$U_{scalar,1Hz} = \sqrt{(cos\theta_y\overline{u})^2 + \overline{v}^2}\sqrt{1+\epsilon} \tag{4.13}$$

where

$$\epsilon = \frac{1}{(cos\theta_y\overline{u})^2 + \overline{v}^2}\left[2cos^2\theta_y\overline{u}u' + 2cos\theta_y sin\theta_y\overline{u}w' + cos^2\theta_y u'^2 + 2cos\theta_y sin\theta_y u'w' + sin^2\theta_y w'^2 + 2\overline{v}v' + v'^2\right] \tag{4.14}$$

Now 2nd order binomial expansion can be used, to form the formula below, with $\overrightarrow{U'} = \begin{bmatrix} cos\theta_y u' + sin\theta_y w' \\ v' \end{bmatrix}$, $U_{vector} = \begin{bmatrix} cos\theta_y \overline{u} \\ \overline{v} \end{bmatrix}$ and $||\overrightarrow{U'}||_2^2 = cos^2\theta_y u'^2 + 2cos\theta_y sin\theta_y u'w' + sin^2\theta_y w'^2 + v'^2$.

$$U_{scalar,1Hz} = U_{vector} + \frac{1}{2U_{vector}} \overline{\left|\left|\overrightarrow{U'}\right|\right| sin^2\theta} \tag{4.15}$$

4.3 Perturbation method for turbulence intensity

For the derivation of equations of TI, the mean speed speed method above will be used. The derivation will include Reynolds decomposition, explained in section 4.1. The whole derivation has been tested in a virtual environment, to prove that certain steps could be taken. For this verification of the equations and a further in-depth derivation, please read Appendix D.

Turbulence intensity is a function of the sigma of the wind speed and the mean wind speed. Therefore the following formulas will be used:

$$TI = \frac{\sigma_U}{U_{mean}} \tag{4.16}$$

$$Var = \sigma_U^2 = \overline{U_{scalar}^2} - \overline{U_{scalar}}^2 \tag{4.17}$$

$$U_{mean} = \sqrt{\overline{u}^2 + \overline{v}^2} \tag{4.18}$$

giving:

$$TI = \frac{\sqrt{\overline{U_{scalar}^2} - \overline{U_{scalar}}^2}}{U_{mean}} \tag{4.19}$$

The derivation in Appendix D gives Equation D.5 as a formula for U_{scaler}. Equation 4.20 is similar to Equation D.5, with the difference in using the formula for U_{mean} in Equation 4.18 instead of the formula for U_{vector} shown in Equation 4.9. When comparing Equation 4.18 with Equation 4.9, it is evident that these formulas are equal, therefore Equation 4.20 is equal to Equation D.5.

$$U_{scalar} = U_{mean}\left[1 + \frac{1}{2U_{mean}^2}\left[2\overline{u}u' + u'^2 + 2\overline{v}v' + v'^2\right] - \frac{1}{8U_{mean}^4}\left[4\overline{u}^2u'^2 + 4\overline{v}^2v'^2 + 8\overline{u}u'\overline{v}v'\right]\right] \tag{4.20}$$

Equation 4.20 can be squared and then the mean can be taken to create Equation 4.21:

$$\begin{aligned}\overline{U_{scalar}^2} = & U_{mean}^2 + \left[\overline{u'^2} + \overline{v'^2}\right] \\ & + \frac{1}{U_{mean}^2}\left[\overline{u}\,\overline{u'^3} + \overline{u}\,\overline{u'v'^2} + \overline{v}\,\overline{u'^2v'} + \overline{v}\,\overline{v'^3}\right] \\ & - \frac{1}{U_{mean}^4}\left[\overline{u}^3\overline{u'^3} + \overline{v}^3\overline{v'^3} + 3\overline{u}^2\overline{v}\,\overline{u'^2v'} + 3\overline{v}^2\overline{u}\,\overline{u'v'^2}\right] + O(4)\end{aligned} \tag{4.21}$$

Now that we have a formula for the first part of the TI equation, we will move on to the next part, using Equation 4.20 as a starting point.

$$\overline{U_{scalar}} = \overline{U_{mean}\left[1 + \frac{1}{2U_{mean}^2}\left(2\overline{u}u' + u'^2 + 2\overline{v}v' + v'^2\right) - \frac{1}{8U_{mean}^4}\left(4\overline{u}^2u'^2 + 4\overline{v}^2v'^2 + 8\overline{u}u'\overline{v}v'\right)\right]} \tag{4.22}$$

$$\begin{aligned}\overline{U_{scalar}}^2 = & U_{mean}^2 + \left[\overline{u'^2} + \overline{v'^2}\right] \\ & - \frac{1}{U_{mean}^2}\left[\overline{u}^2\overline{u'^2} + \overline{v}^2\overline{v'^2} + \overline{2\overline{u}u'\overline{v}v'}\right]\end{aligned} \tag{4.23}$$

We can now fill in the equation for TI:

$$TI = \frac{\sqrt{\overline{U_{scalar}^2} - \overline{U_{scalar}}^2}}{U_{mean}} \tag{4.24}$$

$$TI = \sqrt{\frac{\overline{u'^2} * \overline{cos^2(\theta)} + Cov(u'^2, cos^2\theta)}{U_{mean}^2} + \frac{\overline{v'^2} * \overline{cos^2(\theta)} + Cov(v'^2, cos^2\theta)}{U_{mean}^2}} + O(3) \tag{4.25}$$

We can also include the O(3) term, the formula for this term would be:

$$\begin{aligned} O3 = &\frac{1}{U_{mean}^4}\left[\overline{u}\overline{u'^3} + \overline{u}\overline{u'v'^2} + \overline{v}\overline{u'^2v'} + \overline{v}\overline{v'^3}\right] - \\ &\frac{1}{U_{mean}^6}\left[\overline{u}^3\overline{u'^3} + \overline{v}^3\overline{v'^3} + 3\overline{u}^2\overline{v}\overline{u'^2v'} + 3\overline{v}^2\overline{u}\overline{u'v'^2}\right] \end{aligned} \tag{4.26}$$

Higher-Order Terms

Since the generated TI equation seen in Equation 4.25, is an equation that takes the root of the result, this means that a second-order term is actually a first-order term. As could be seen in Appendix D, the fourth-order terms fell away, but since those are actually second-order terms it might be interesting to expand the derivation to fifth- and sixth-order terms for TI^2. This will depend on the impact of the third-order term of the equation on the eventual result of TI, which will be further discussed in chapter 5.

3D Turbulence

It is also possible to include the vertical wind speed component in the result for TI. This would lead to Equation 4.27. The effect of this inclution will be discussed in chapter 5.

$$TI^2 = \frac{1}{U_{mean}^2}\overline{[u'^2 + v'^2 + w'^2]\, cos^2(\theta)} + O(3) \tag{4.27}$$

4.4 Validation

As can be seen in Appendix D, the different steps taken in the derivation have been validated. However next to that, the equation for turbulence intensity has been validated with a Kaimal spectrum. Firstly, the mean wind speed derivation by Andrew Black [28] was compared against a Kaimal Spectrum, following the IEC standard 61400-1 [25]. The formula for the Kaimal Spectrum can be seen in Equation 4.28 [87]. After the comparison, it was discovered that the difference between Kaimal Mean Wind and Black Mean Wind in the Black derivation is approximately 0.25%. Additionally, when incorporating second-order terms, this difference decreases to 0.005%. Furthermore, incorporating the fourth-order terms reduces the difference to 0.00035%.

$$S_u(f) = \frac{\sigma_u^2}{f} * \frac{4fL_u/\overline{u}}{(1 + 6fL_u/\overline{u})^{\frac{5}{3}}} \tag{4.28}$$

here f is the frequency in hertz, while the subscript u denotes the index of the longitudinal velocity component. The single-sided velocity component spectrum is denoted as S_u, σ_u is the standard deviation and L_u is the integral length scale.

After verifying the derivation carried out by Black, it was essential to validate the newly formulated TI formulas. This was also done using the Kaimal spectral model. Initially, a test case was generated, which resulted in a discrepancy of 0.1%. However, upon incorporating third-order terms, this difference was reduced to 0.02%. In addition to this test case, it was possible to calculate the TI for the Vattenfall wind site dataset. Upon reviewing the documentation for the Zephir LiDAR, it was discovered that the TI is calculated using the following formula for the LiDAR:

$$TI = (\frac{\sigma_u}{\overline{u}})/C \tag{4.29}$$

where C is a correction factor of a value of approximately 0.96 and knowing from Sathe and Mann [14] that $\sigma_u = \sqrt{[u'^2]}$.

Chapter 5

TI Adjustment Method

DNV report DNV-RP-0661 highlighted the need for adjustment methods to accurately predict turbulence intensity using lidar measurements, as they tend to overpredict TI. This chapter will utilize the derivation from chapter 4 to develop an adjustment method. The resulting method will then be compared with lidar TI measurements, the ZX correction, and meteorological mast measurements. Initially, a virtual turbulence environment will be created, incorporating a virtual lidar, to verify the derivation from chapter 4 using known turbulence parameters. Following this, a test site will be selected to validate the adjustment method using real-world data. For confidentiality reasons, the test site will not be referred to by name to respect Vattenfall's site anonymity.

5.1 Turbulence box

To validate the work carried out in chapter 4 and the final derived equation of Equation 4.25, a virtual turbulence box has been created using DTU's Hipersim [88]. Hipersim includes a Mann turbulence generator [89], that is capable of creating stationary Gaussian wind fields with uniform variance and predefined spectrum and coherence properties [90]. The Gaussian nature of the box allows for easy mathematical formulation and reasonable loading in normal wind conditions [91]. Since this thesis project focuses on normal wind conditions and does not extend to highly turbulent fields, a Gaussian turbulence box seems to be the best fit. For the first iteration of the turbulence box, the Mann parameters were chosen based on a paper by N. Dimitrov [92], resulting in the turbulence box shown in Figure 5.1.

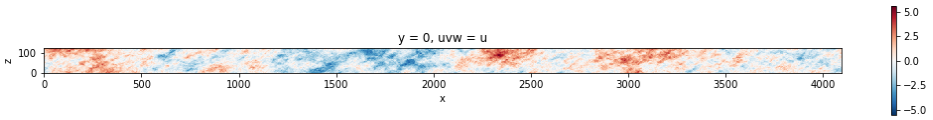

Figure 5.1: Turbulence box (L=23.9, $\alpha\epsilon^{2/3} = 0.867$, $\Gamma = 3.9$)

The turbulence box has been created using a Mann model, which requires turbulence parameters. The Mann model, a spectral tensor model based on rapid distortion theory (RDT) and eddy lifetimes, is particularly useful for generating realistic turbulence fields for simulations [89]. This model requires three parameters: the turbulence dissipation rate, the turbulence length scale, and a parameter related to eddy lifetimes [93]. Studies have utilized the Mann model to create turbulence boxes, which simulate atmospheric turbulence for applications such as lidar measurements in wind energy systems. These virtual turbulence boxes help account for the scanning configurations and probe volume effects of lidars, thereby providing more accurate turbulence measurements and enhancing the performance of wind turbine control systems [94].

5.1.1 Lidar measurements

The Mann turbulence box was created to validate the work in chapter 4. The next step involves creating a virtual lidar capable of taking measurements in the virtual turbulence box. To achieve this, a paper by R. Robey [30] was utilized. In her research, Robey managed to couple a ground-based continuous wave lidar to the WRF-LES data of the Advanced Research Weather Research and Forecasting model. The goal was to modify her model to fit the Hipersim turbulence box. A virtual lidar was successfully created, and measurements were conducted in two different ways. The first method involved letting the lidar generate instant circles and positioning them next to each other, as illustrated in Figure 5.2.

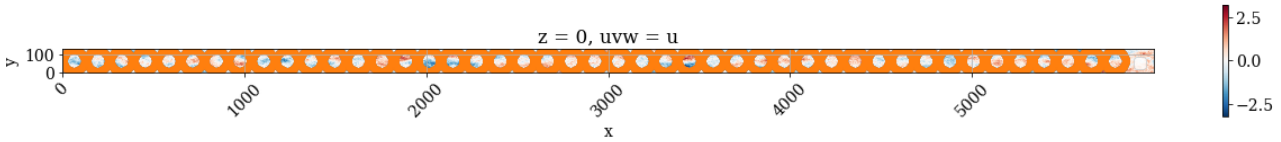

Figure 5.2: Turbulence box with instant lidar rings

In their study, Sathe *et al.* [51] argue that using the instant lidar ring approach will produce the same outcomes as conducting a proper continuous wave scan. As described in subsection 1.1.4, the ZephIR 300 operates by transmitting a laser beam through a rotating prism. Because the turbulence box is stationary, the lidar measurements need to move over this box, resulting in the shapes illustrated in Figure 5.3. There is a spacing of 160 in the x-axis between the starting points of each measurement, as shown more clearly in Figure F.13. This spacing is because the ZephIR lidar takes measurements at different heights, and there is approximately a 15-second delay for the next measurement at the same height to occur, while the measurement itself takes 1 second. Consequently, there is a total time difference of 16 seconds between two measurement starting points. For this virtual lidar, a height of 100m has been selected, which impacts the diameter of the lidar ring (refer to section B.3). The box reaches an x value of 6000. To simulate the test site environment for a 10-minute period, the x value has been set to the product of the wind speed ($U = 10m/s$) and the time ($t = 600s$). It was observed that both the instant and the continuous approach produced similar results, which will be further discussed in subsection 5.1.2.

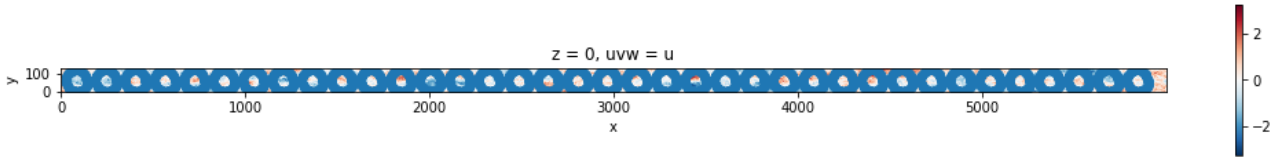

Figure 5.3: Turbulence box with continuous lidar scan

5.1.2 Validation results

The virtual lidar was used to validate the derivation process of chapter 4. This included comparing the TI of the final derivation in Equation 4.25, while also verifying the steps taken in the derivation itself. The verification of the derived equation was done using different turbulence parameters for the Mann turbulence model, and for each set of parameters, four different turbulence boxes were created. In the validation of the perturbation adjustment method, different length scales and different turbulence levels were chosen. Next to varying the length scales and turbulence levels, the other Mann parameters were kept constant. While changing the length scale, the turbulence level was kept low with the value for $\alpha\epsilon^{2/3}$ chosen at 0.03, to focus purely on the effect of changing the length scale. Next to that, the eddy lifetime factor Γ was changed from the previously used value of 3.9, taken from N. Dimitrov [92], to a value of 3.1. While changing the value for $\alpha\epsilon^{2/3}$, the same eddy lifetime factor was chosen and the length scale was kept at a value of 23.6.

Eddy lifetime factor

According to Dimitrov *et al* [92], the eddy lifetime factor Γ describes the shear deformation of turbulence eddies, while also affecting the ratio of the variances of the different wind-speed components. When $\Gamma = 0$, it indicates isotropic turbulence. This implies that $\sigma_u^2 = \sigma_v^2 = \sigma_w^2$ [37]. An increase in the eddy lifetime factor results in ratios between the variances of the u, v, and w components larger than 1. For this project, a value for Γ of 3.1 has been chosen. This value has been chosen as a better parameter value to use for the turbulence box, as explained by M. Kelly [95] and by de Mare and Mann [96].

De Mare and Mann proved that $\sqrt{\alpha}\frac{\Gamma\epsilon^{1/3}}{\frac{\partial U}{\partial z}L_M^{2/3}}$ should be constant and have a value of around 3.0 [97]. After this, the authors introduce the parameter G in a later paper [96], as can be seen in Equation 5.1, which is closely related to the eddy lifetime factor Γ. In Equation 5.1, ϵ is the turbulent kinetic energy dissipation rate, u is the friction velocity, $\frac{dU_1}{dz}$ is the shear, α_K is the Kolmogorov constant, L_M is the turbulent length scale, and lastly M is a constant introduced by the authors.

$$G = \frac{M\frac{dU_1}{dz}L_m^{2/3}}{\sqrt{\alpha_K}\epsilon^{1/3}} \tag{5.1}$$

The IEC standard recommendation for the eddy lifetime factor is to have a value of 3.9 [92], as used in Figure 5.1. However, through stability cases at different wind sites, Chougule *et al* [98] show that 3.16 is a more realistic value when measurements are taken under neutral and slightly unstable conditions. This value is confirmed by the testing of Sathe *et al* at the Høvsøre test site [37]. Since this project takes place at a flat wind site, it is more valuable to use an eddy lifetime factor of 3.1.

Turbulence length scale

The turbulence length scale plays a significant role in characterizing turbulent flows by influencing turbulence intensity and other parameters. The length scale represents the size of the largest eddies within a turbulent flow, which are responsible for the primary energy-containing motions [99]. It determines the transfer of energy from large eddies to smaller ones through the energy cascade process, thereby impacting overall turbulence intensity [100]. A larger turbulence length scale typically indicates stronger and more energetic turbulence, leading to higher turbulence intensity [101]. Additionally, the length scale affects the distribution of kinetic energy across different scales and influences key parameters such as the turbulence dissipation rate, which measures the rate at which turbulent kinetic energy is converted into thermal energy through viscous forces [102]. The length scale is also critical in defining the Reynolds number in a turbulent flow, which dictates the flow regime and the spatial and temporal scales of turbulence [103]. Understanding and accurately measuring the turbulence length scale is crucial for predicting and modeling turbulent behavior in various engineering and environmental applications [43]. As shown in Figure 5.4, an increase in length scale increases turbulence intensity. Additionally, it appears that for all values of the length scale, the measurements closely align with the expected derivations. Since the $\alpha\epsilon^{2/3}$ parameter is kept low, the derivations should closely match the measurements, as they could only differ at high turbulent fields, as mentioned by Black [28].

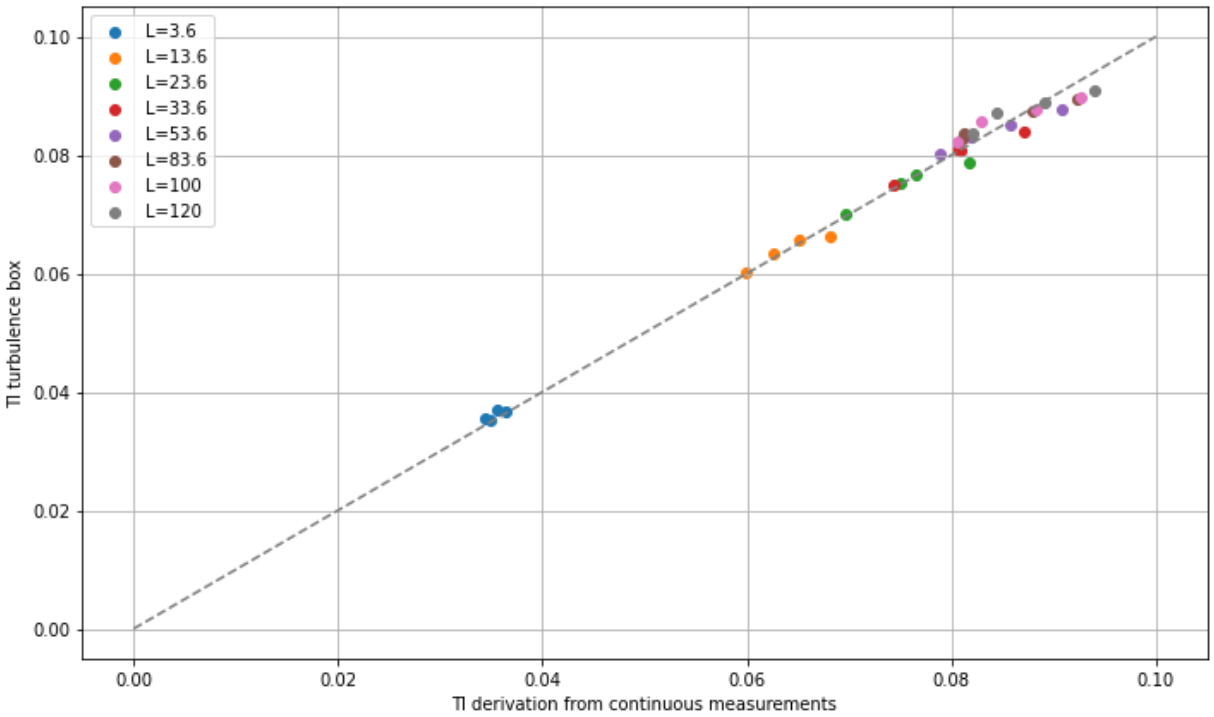

Figure 5.4: Comparison between ideal mean TI from four different turbulence boxes and continuous virtual lidar observations for different Mann-model length scales

Turbulence level

The Mann turbulence parameter, $\alpha\epsilon^{2/3}$, is another vital factor in the Mann model. This parameter combines the Kolmogorov constant, α, with the turbulence dissipation rate, ϵ, and plays a significant role in defining the energy distribution across different scales of turbulence. The parameter α is related to the universal constants of turbulence theory, while ϵ measures the rate at which turbulent kinetic energy is dissipated into thermal energy [89]. In practical applications, such as the simulation of turbulence in virtual turbulence boxes, the Mann model leverages the parameter $\alpha\epsilon^{2/3}$ to accurately represent the spectral energy distribution and anisotropy of the turbulence field [93]. This is particularly important for simulating realistic atmospheric conditions for studies involving wind energy systems and lidar measurements. For instance, $\alpha\epsilon^{2/3}$ directly affects the three-dimensional spectral tensor used in the model, which is critical for generating accurate turbulence realizations

that mimic natural atmospheric conditions [94]. These simulations allow researchers to better predict and control the behavior of wind turbines, thereby optimizing their performance and reliability [51]. As can be seen in Figure 5.5, an increase in the Mann turbulence parameter, leads to an increase in turbulence intensity, and as expected the compliance of the derivation reduces at higher TI values, leading to an overprediction of TI.

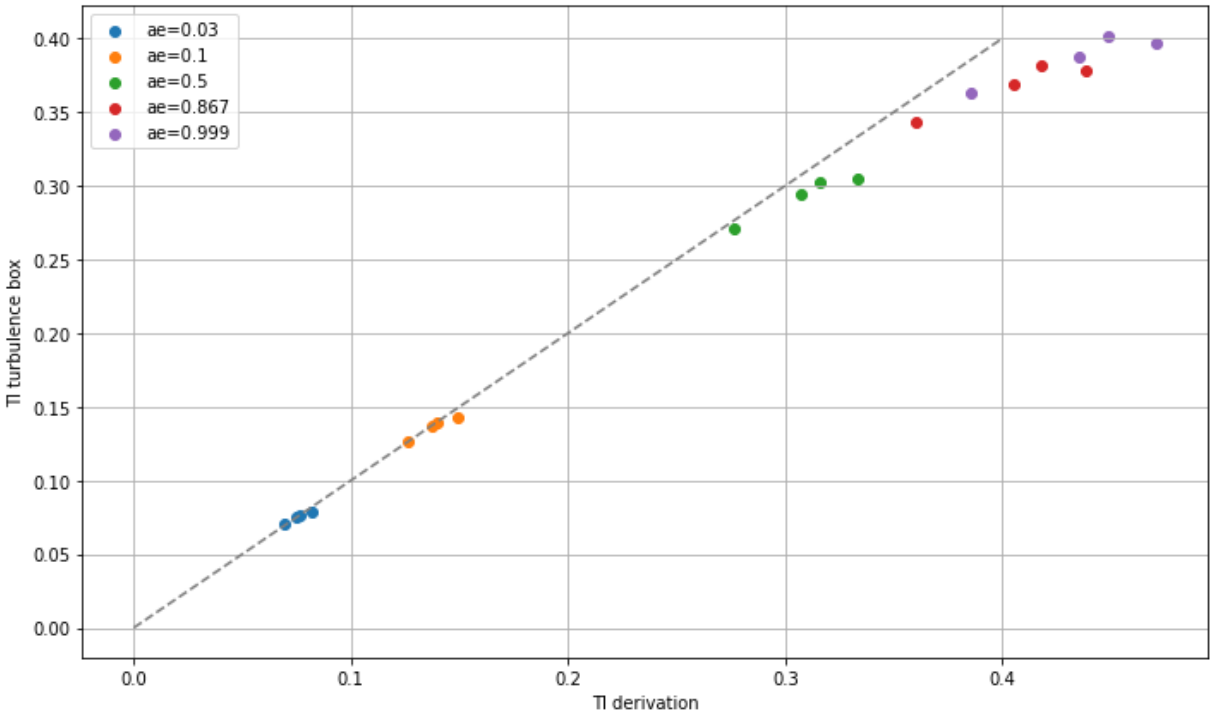

Figure 5.5: Comparison between ideal mean TI from four different turbulence boxes and continuous virtual lidar observations for different Mann-model turbulence parameters

Continuous lidar measurements vs lidar rings

As said before, the virtual lidar measurements have been executed in two ways: placing instant circles next to each other, and using continuous measurements with intervals of 15 seconds. According to Sathe et al. [51] these two methods should yield similar results. As can be seen when comparing Figure 5.6 with Figure 5.4, both the methods perform well when compared with the TI of the entire box, therefore it can be assumed that both methods can be used for the TI calculation in a virtual environment. Next to that, when comparing Figure 5.7 with Figure 5.5, both methods perform the expected trend of overprediction at higher TI levels.

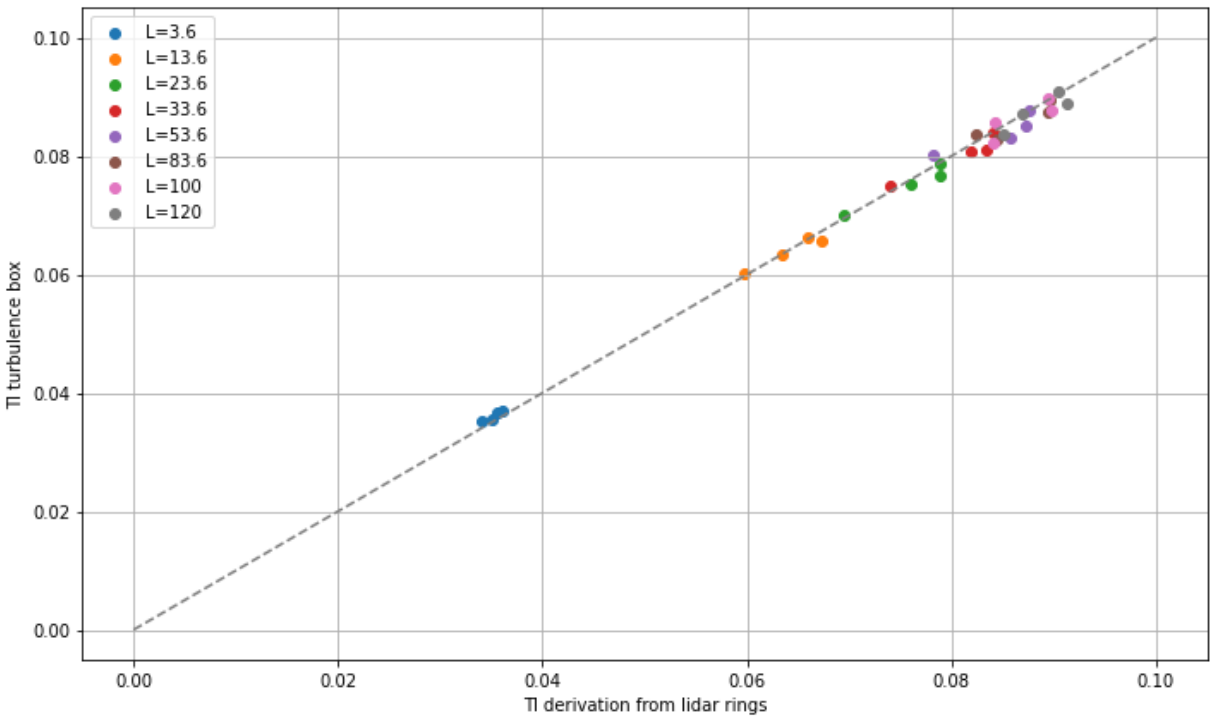

Figure 5.6: Comparison between ideal mean TI from four different turbulence boxes and lidar ring measurements for different Mann-model length scales

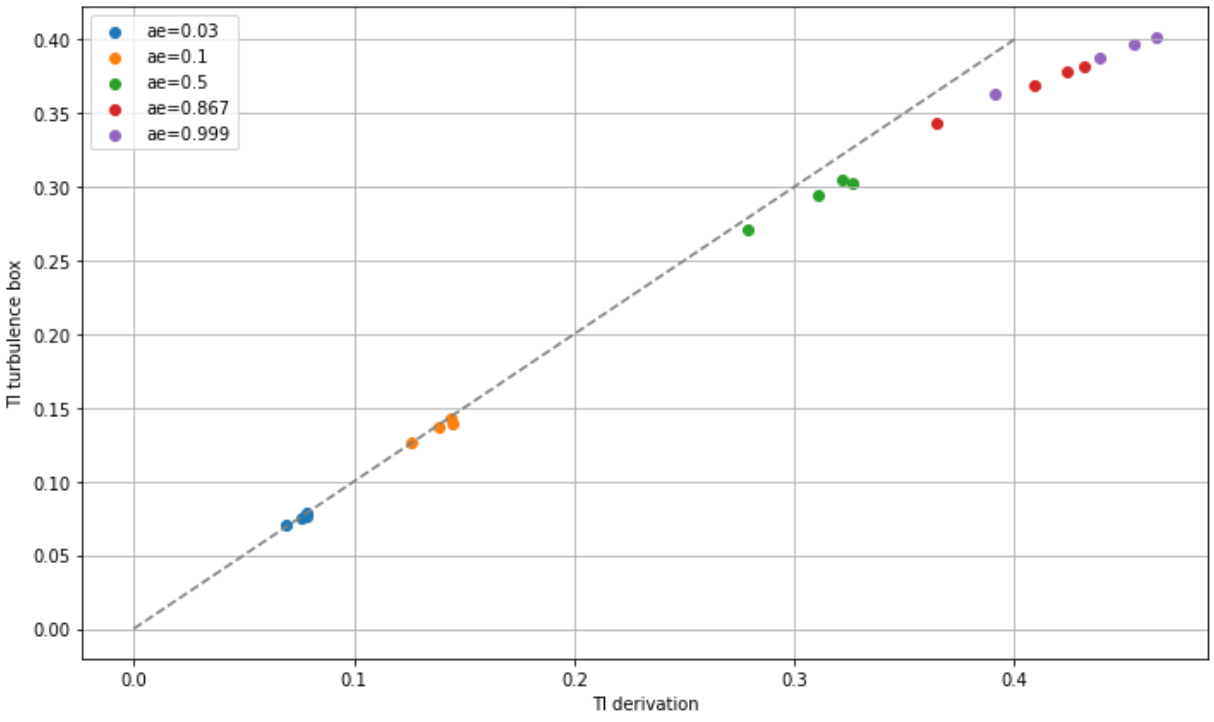

Figure 5.7: Comparison between ideal mean TI from four different turbulence boxes and lidar ring measurements for different Mann-model turbulence parameters

5.2 Vattenfall test site

After validating the work of chapter 4 with the turbulence box, the derivation can be used on real-world data. For this, a Python structure has been created, as can be seen in Appendix C. The real-world data comes from a flat terrain site in the south of the Netherlands. At this site, there was access to a year of lidar data and a year of anemometer data, of which two months of data had an overlap. The dominant wind direction at

this wind site was the southwest wind direction, as can be seen in Figure 3.2. The testing of the derivation in the test site has been based on the DNV report, where different adjustment methods have been compared based on the calculation of the MRBE and RRMSE, as explained in section 1.1.6. In this thesis project, the focus will be on the MRBE graph of this report. Figure 5.8 and Figure 5.9 show the MBRE between different perturbation adjustment methods and the cup anemometer. The figures also show the lidar without an adjustment and the lidar with a ZX correction, which has been explained in section 4.4. As can be seen in Figure 5.8 and Figure 5.9, the adjustment method based on the perturbation adjustment results in a correction of the lidar TI close to the correction made by Zephyr. It also shows the effect of adding third-order terms to the equation, as well as adding the vertical w component. The addition of these components does not result in a significant improvement in the TI prediction. Bear in mind that a positive value for MRBE indicates that the lidar is overpredicting in comparison to the cup anemometer, while a negative MRBE error signifies that the lidar is underpredicting the TI when contrasted with the cup anemometer, as evidenced in Equation 1.7.

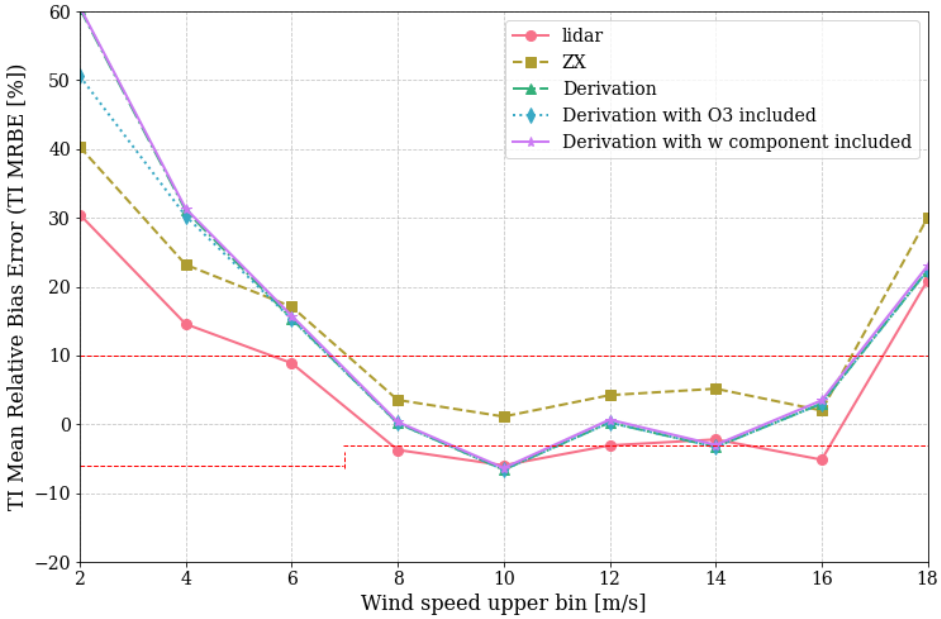

Figure 5.8: Comparison of the MRBE of different adjustment methods at 82m

In the context of optimizing TI predictions using lidar measurements, specific wind speed ranges are particularly important due to their impact on turbine performance and structural integrity. Wind speeds in the range of 4-6 m/s are significant because this is where turbines start to consistently produce power, and accurate TI predictions at these speeds can help fine-tune the turbine's initial operational adjustments. The mid-range speeds of 8-14 m/s are crucial because turbines operate near their optimal efficiency in these ranges; therefore, precise TI measurements are vital for maximizing power output and ensuring smooth operation. These speeds are also where the impact of turbulence on fatigue loads becomes significant. For higher wind speeds, particularly in the 16-18 m/s range, accurate TI predictions are essential for managing power regulation and mitigating increased fatigue loads. At these speeds, turbines often approach their rated capacity, and turbulence can cause substantial mechanical stress. Finally, at very high wind speeds (20-24 m/s), correct TI predictions are critical for preventing damage and ensuring the safety of the turbines. Turbulence intensity in this range can lead to severe mechanical fatigue and increased wear, making it essential to have precise lidar-based measurements to manage these conditions effectively. Overall, while all wind speed ranges have their importance, the 8-14 m/s range is particularly crucial for optimizing turbine performance and longevity through accurate TI predictions.

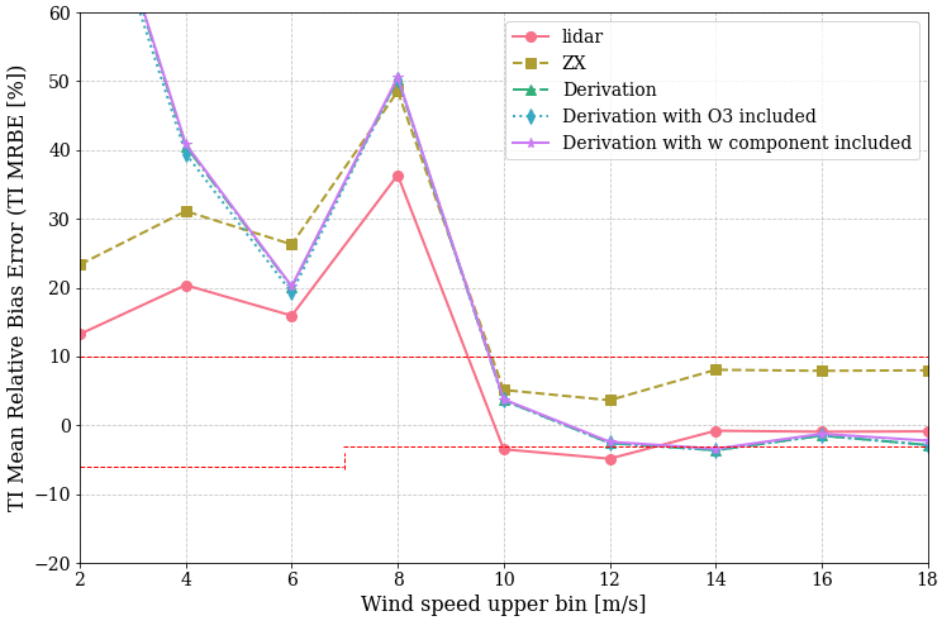

Figure 5.9: Comparison of the MRBE of different adjustment methods at a measurement height of 122m

As shown in Figure 5.8, at a height of 82 meters, the perturbation adjustment begins to perform within the DNV boundaries at a wind speed of 8 m/s and remains close to this boundary until 16 m/s, demonstrating good performance in the 8-14 m/s range. In Figure 5.9, it is clear that at a height of 122 meters, the perturbation adjustment performs well for high wind speeds. However, the method does not stay within the DNV boundaries for 8 m/s, which is likely due to roughness, as the lidar measurements and the ZX correction also indicate significant mean errors. The dominant southwest wind direction means that in this direction, most measurements are taken. This is evident in the comparison of Joint PDF plots in Figure 5.10 and Figure 5.11. The increased number of measurements in the southwest direction enhances the accuracy of TI predictions, as indicated by the lidar-to-cup ratio, explained in section B.4, which centers around -0.1. In contrast, the North-Northwest direction exhibits a more dispersed ratio due to the limited number of measurements. In Figure 5.11, it is evident that at a wind speed of around 8 m/s, the lidar starts to show more under prediction, a trend that was also visible in Figure 5.9. After further research, it could be shown that this was likely due to roughness in the area. Appendix A goes into the terrain analysis done to look at this roughness.

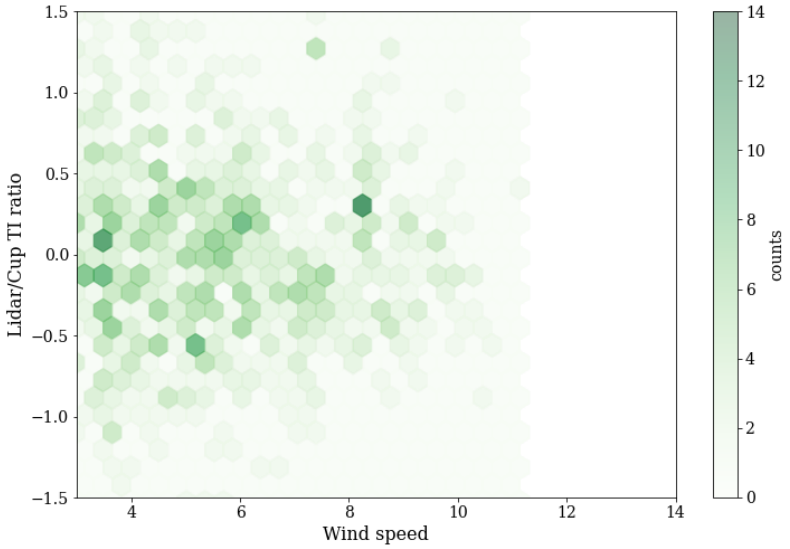

Figure 5.10: Joint PDF plot for NE-E direction at 100m

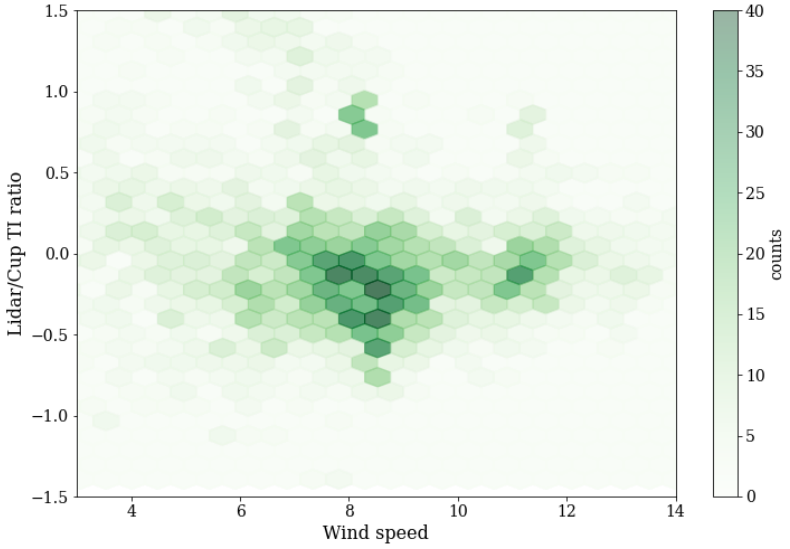

Figure 5.11: Joint PDF plot for S-SW direction at 100m

When we compare the joint PDFs of the lidar with the ZX correction and the different versions of the perturbation adjustment method, it is clear that both the perturbation adjustment method and the correction done by Zephyr result in a shift that reduces the underprediction of the lidar. These joint PDFs come from lidar measurements at a height of 100 meters, which are then compared with measurements from a meteorological mast located 300 meters away, as can be seen in Appendix F, at a height of 101.3 meters. It's important to keep in mind that the differences in location and height will also introduce additional errors and uncertainties in the comparison of measurements, which will be further discussed in chapter 6.

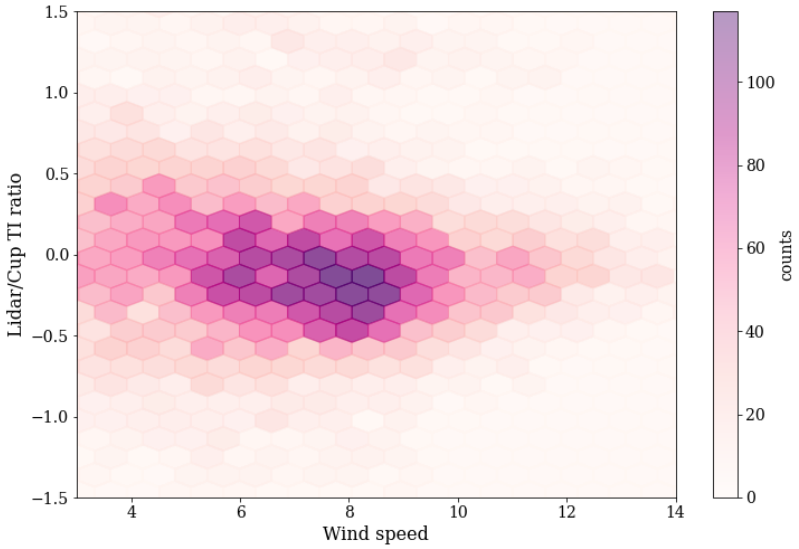

Figure 5.12: Joint PDF plot for lidar without adjustment

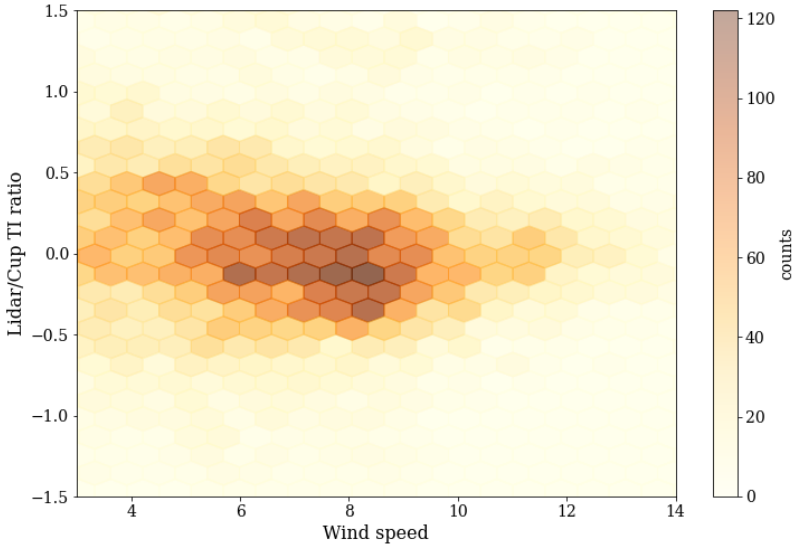

Figure 5.13: Joint PDF plot for lidar with ZX correction

Matching the lidar measurements to cup measurements has several significant advantages. Firstly, reducing the mean relative bias error and bringing the ratio between lidar and cup measurements closer to zero enhances the reliability and accuracy of the lidar data. Right now, the uncertainty in lidar TI estimates is standing in the way of the acceptance of lidar, having the lidar measurements align better with cup anemometer measurements could result in a better acceptance of lidar systems, which will be further explained in chapter 7. It is clear in Figure 5.13 that the correction done in the ZX300 lidar makes the lidar/cup TI ratio reach values closer to zero. The calculation of this ratio can be found in section B.4. If all the values were zero, this would mean perfect alignment between the cup and lidar. If the value is negative, this means that the lidar underpredicts the TI, whereas if the value is positive, the lidar is overpredicting TI. It is evident in Figure 5.12 that the lidar underpredicts the cup anemometer TI values, and this underprediction is solved by Zephyr, by adding a correction factor C, as explained in section 4.4.

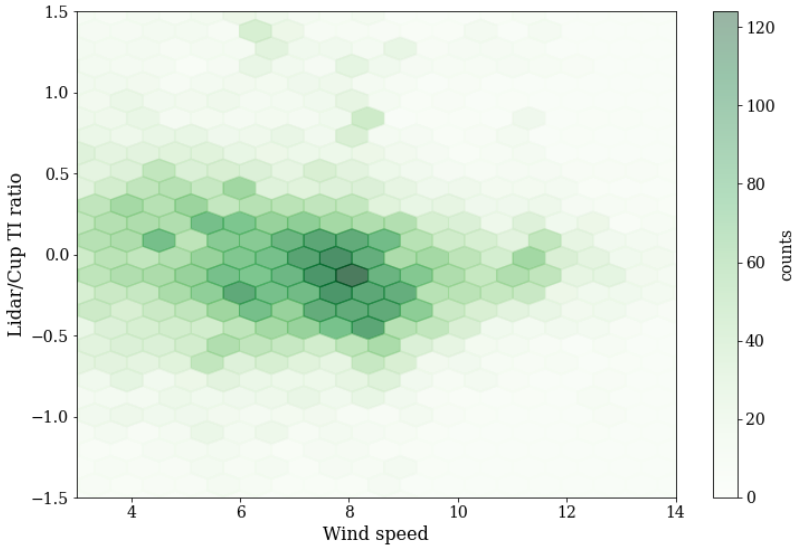

Figure 5.14: Joint PDF plot for lidar with perturbation correction

As can be seen in Figure 5.14, the perturbation adjustment does a similar adjustment to the ZX correction factor. The perturbation adjustment also decreases the underprediction from lidar TI measurements. Figure 5.15 shows that including the third-order terms also adjusts the lidar TI prediction, however, including the thrid-order terms does not show a promising extra adjustment, seeing that the ratio stays close to the ratio values from Figure 5.14.

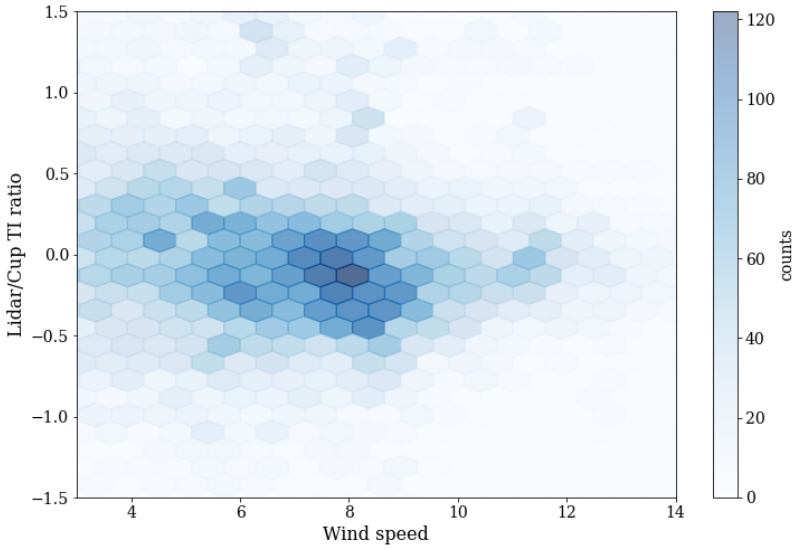

Figure 5.15: Joint PDF plot for lidar with third-order perturbation correction

5.3 Comparison with different adjustment methods

The perturbation adjustment method is a physics-based TI correction model. Over the years multiple kinds of adjustment methods have been created in academia. These adjustment methods mostly require the use of 1Hz data to resolve the low pass filter bias introduced by volume averaging, cross-contamination, and noise. Dimitrov et al. [104] demonstrate a method for incorporating wind measurements from continuous-wave lidars into turbulence fields used for wind turbine load simulations. The study showed the potential of incorporating lidar measurements as constraints to reduce statistical uncertainty in the loads and power production of the

turbine. Interestingly it showed that a larger turbulence length scale led to larger reductions in uncertainty due to an increased correlation length. Sathe et al. [13] utilized correction methods that reconstructed the 1 Hz lidar data which led to a correction of TI. A six-beam method was created, which reduced variance contamination but introduced errors in variance estimates. The study introduces the use of the velocity azimuth display (VAD) method. However, the study concludes with the recommendation of not using the VAD or DBS method in estimating turbulence statistics. L-TERRA, which was touched upon in chapter 2, is a model that corrects TI data by modeling the turbulence at each beam [50] [73]. L-TERRA uses high-frequency output files from the lidar, which includes the different wind velocity components. L-TERRA consists of four different modules that focus on noise removal, volume averaging. variance contamination, and lastly machine learning. Some of the methods exploited by L-TERRA are purely meant for the u, v, and w velocity data, while others can also be applied to the radial velocity. This is contrary to the perturbation adjustment method, which focuses on the u, v, and w velocity data only. The method is validated by looking at the mean absolute error. The perturbation method includes the effects of Reynolds stresses and wind direction variance by looking at the covariance between the Reynolds stresses and the fluctuation of the wind direction. Still, the derived adjustment method does not account for inherent instrument errors.

Chapter 6

Uncertainty in turbulence intensity

Lidar measurements are a great cost-effective alternative for meteorological masts in wind parks. However, the uncertainty in turbulence intensity measurements is still affecting the acceptance by the industry. Therefore the adjustment method discussed in chapter 5 has been developed. This TI adjustment method focuses on perturbation theory-based corrections on the lidar measurements, which offers a physics-based correction on the data. The model was tested in a virtual environment and a wind park site in the Netherlands. This chapter goes into the different factors of uncertainty in TI measurements, and how some of these uncertainties can be tackled by this new adjustment method.

6.1 Background

Turbulence intensities are often determined using simplified formulations, as seen previously in this master's thesis work. These simple formulations are made with a neutral atmospheric stability assumption, while also only accounting for the wind speed dependence [105]. Various factors can cause uncertainty in turbulence intensity measurements. The accuracy and precision of the equipment used to measure wind speed and direction can introduce uncertainty. For instance, lidars and anemometers may have inherent errors or design limitations which can affect the reliability of the measurements. Proper calibration of instruments is also important for accurate measurements. Calibration errors can result in inaccuracies in turbulence intensity readings. Additionally, turbulence itself can make measurements challenging. Wind flows are inherently complex and can be influenced by several factors such as terrain, nearby structures, atmospheric stability, and boundary layer effects. These factors can introduce uncertainty into measurements. It's also important to note that the methods used to process and analyze wind data can introduce uncertainty. Different algorithms and techniques may produce slightly different results, leading to uncertainty in turbulence intensity measurements. Lastly, the duration of the measurement period can affect the accuracy of turbulence intensity estimates. Shorter sampling periods may not capture the full range of turbulence present in the wind flow, leading to underestimation or overestimation of turbulence intensity.

Quantifying the uncertainty in wind measurements of turbulence intensity requires an assessment of potential sources of error and their impact on the measurement accuracy [106]. The following methods are commonly used to quantify uncertainty [107]. One could review the specifications of the instruments used for wind measurements. Manufacturers often provide information on the instrument's accuracy, precision, and calibration uncertainty, which can serve as a baseline for understanding measurement uncertainty. To quantify uncertainty regular calibration of instruments has to be performed to ensure accuracy and keep detailed records of calibration procedures and uncertainties associated with the calibration process. Calibration certificates provided by calibration facilities can be used to quantify uncertainty in calibration. Then quantify by identifying the sources of error in wind measurements, such as instrument errors, environmental conditions, and data processing techniques. Use error propagation analysis to estimate how these errors propagate through the measurement system and contribute to overall uncertainty. Using a field test under controlled conditions can help to assess the performance of instruments and measurement techniques. Comparing measurements from different instruments or methods can help evaluate consistency and identify potential sources of error. For further quantification, an uncertainty budget can be developed that quantifies the contributions of different sources of error to the overall measurement uncertainty. This involves assigning uncertainties to each component of the measurement process, such as instrumentation, calibration, environmental conditions, and data processing. Monte Carlo simulation techniques can also be used to estimate uncertainty by randomly sampling input parameters within their respective uncertainty distributions and propagating these uncertainties through the measurement process to calculate the resulting uncertainty in turbulence intensity measurements. Also, relevant ISO (International

Organization for Standardization) standards, such as ISO17025 for calibration laboratories or ISO61400 for wind turbine performance testing, provide guidelines for assessing measurement uncertainty in various contexts.

6.2 Uncertainty types

According to J. Newmann [50], there are three main drivers for TI errors: instrument noise, volume averaging, and variance contamination. Instrument noise results from factors such as the limited amount of scatterers in the lidar probe volume and spontaneous laser emissions. Volume averaging occurs because the lidar must receive backscattered radiation from a volume of air, rather than a point, to obtain a sufficient amount of data for estimation of the radial wind speed. The probe volume acts as a low-pass filter, as high-frequency motion that occurs on spatial scales smaller than the probe volume of the lidar cannot be resolved. Variance contamination is caused by the scanning strategy. When velocity data from different parts of the lidar scanning circle are combined to estimate the raw wind speed components, it is assumed that the instantaneous wind field is uniform across the scanning circle. However, this assumption is not true due to turbulence, and changes in the wind field across the lidar scanning circle introduce additional variance components into the calculation of the u, v, and w variance. Next to the uncertainties mentioned by Newmann in subsection 6.2.1 through subsection 6.2.3, Gribben et al. [108] further adds the lidar uncertainties arising from calibration, differences with the mast and the complexity of the terrain. These uncertainties will be discussed in subsection 6.2.4 until subsection 6.2.6. The section will conclude with a quantification of the uncertainties in subsection 6.2.7.

6.2.1 Instrument errors

Wind lidars can experience increased uncertainty in turbulence measurements due to instrument noise. This noise can be attributed to a limited amount of aerosol scatters in the probe volume, as discussed by Lenschow et al. [109]. Additionally, as mentioned by Chang [110], spontaneous radiation emissions from the laser can also contribute to instrument noise. The resulting noise can inflate the measurement of the standard deviation of different wind speed components, thereby potentially increasing the turbulence intensity prediction. This instrument noise in lidar measurements is referred to as the Carrier-to-Noise Ratio (explained in chapter 1), which means that the variance measured by lidar is overestimated in unstable conditions [50] [109]. As highlighted by Sathe et al. [13], a lidar measurement consists of laser pulses, each with a characteristic Gaussian shape. These pulses are usually emitted in continuous bursts over a period of time. Depending on the duration, aerosol particles can be exposed to the laser light for longer periods, resulting in a higher CNR, which in turn affects the maximum distance from which the radial velocity can be derived. This inherent characteristic of all lidar data necessitates filtering techniques to eliminate data spikes from the spectral data, and many complex correction methods are employed for this purpose [49] [50] [51]. Before applying the perturbation method to the data, the data underwent filtering to eliminate outliers and instrument noise. It's important to note that the perturbation method itself does not address the instrument errors of the lidar, and therefore does not reduce this uncertainty in TI measurements. To reduce this uncertainty, the perturbation adjustment needs to incorporate a spike filter or utilize the Lenschow method similar to L-TERRA [73].

Lidar also has uncertainty due to its probe length. Lidar systems are equipped with a probe length that determines the height resolution and influences the volume over which wind speeds are averaged [16]. When lidar takes volume averages of non-linear wind profiles, such as logarithmic wind profiles over a specific range of heights determined by the lidar's height resolution, it introduces a bias to the measurement due to the non-linearity of the wind profile. Clive [16] identified a ratio of the volume average that indicates the magnitude of this bias (Equation 6.1). Essentially, a remote sensing device sensitive to signal returns from a range of heights detects the point value in the middle of the height range that is being averaged, similar to what a cup anemometer would measure for a non-linear wind profile. This can then be used as a ratio to see how resolving this issue would influence the lidar measurement.

$$\beta = \frac{< u_z >}{u_z} \tag{6.1}$$

Lastly, a lidar can have potential errors in determining the distance between the lidar sensor and the target surface. This range uncertainty is influenced by factors such as instrument calibration, atmospheric conditions, and signal noise. In the context of turbulence intensity measurements, range uncertainty can significantly impact the accuracy of assessing atmospheric turbulence characteristics. TI quantifies the variation in wind speed within a certain range and is crucial for applications such as wind energy assessment and atmospheric research. Range uncertainty affects TI measurements by introducing errors in the determination of the spatial extent over which wind speed variations are evaluated. Adjusting the TI measurement parameters, such as the averaging window size or the spatial resolution of the analysis, can help mitigate or quantify the effects of range

uncertainty. By optimizing these parameters based on the specific characteristics of the lidar system and the environmental conditions, the accuracy and reliability of TI measurements can be enhanced, thus improving the understanding of atmospheric turbulence phenomena.

6.2.2 Volume averaging

Volume averaging reduces the turbulence estimated from the lidar measurements. In order to obtain an accurate estimate of the radial velocity, lidars need backscatter data from a large number of scatterers within a probe volume. The probe volume involves a tradeoff between spatial resolution and data accuracy. If the probe volume were smaller than 20 m, there would be fewer data points available to estimate the radial velocity, leading to higher uncertainty in the measurements. Because of the significant measurement volume, the velocity estimate represents the weighted sum of a distribution of velocity measurements along the line-of-sight (LOS) instead of a single measurement. This can result in uncertainties in estimating a representative LOS velocity and in underestimating turbulence due to filtering high-frequency turbulence components [49]. When assuming homogeneous flow, the line-of-sight measurements can be projected onto a three-axis coordinate system [111]. However, for this project, dealing with flat terrain, the homogeneous flow assumption will hold. As stated by Klaas-Witt et al. [112], common Doppler lidar profilers suffer from erroneous reconstruction of the horizontal wind vector in inhomogeneous flow conditions typically found at complex terrain sites. Along the line-of-sight, the lidar measures a volume, so the measurements represent spatially averaged samples of the wind speed. Continuous-wave lidars, used in this project, can measure at high frequency, but the measurement volume increases with the focusing distance, which increases with measurement height [113]. The perturbation adjustment takes into account the high-frequency turbulence components, instead of filtering them, and should therefore help in the underestimation of turbulence, as could be seen in chapter 5.

6.2.3 Variance contamination

Variance contamination is a significant source of uncertainty in ground-based lidar measurements. One primary cause of variance contamination is the presence of atmospheric particles such as aerosols and water vapor, which scatter and absorb the laser pulses emitted by lidar systems. This interaction introduces noise and errors, reducing data accuracy and increasing measurement uncertainty. The concentration and distribution of aerosols can significantly affect the lidar signal return, complicating the differentiation between atmospheric constituents and surface characteristics. Additionally, environmental factors such as temperature and humidity fluctuations exacerbate this issue by altering the air's refractive index, affecting the lidar pulse propagation and backscatter signal. Instrumental noise also contributes to variance contamination, introducing another layer of uncertainty. Hardware components of the lidar system, including the laser source, detectors, and electronics, can generate noise that degrades measurement quality. According to Pena et al. [94], due to the laser beams scanning in different directions in the atmosphere, there might be contributions from different velocity components that can lead to higher turbulence estimates than those from a cup or sonic anemometer. This theory is underlined by Kelberlau and Mann [63], who say that the cause of the variance contamination error lies in the combination of radial velocities from spatially separated air volumes. The u and v wind components are reconstructed through a combination of measurement values from two spatially separated air volumes. This is only correct if a wind vector is identical over all the measurement volumes, this is thus not taken into account at the unadjusted lidar TI prediction, whereas the perturbation adjustment takes this into account, by incorporating the angle between the time-averaged wind direction and that of the 1-Hz fluctuation.

6.2.4 Calibration errors

Calibration errors and misalignments further increase variance, diminishing data reliability. A critical factor in variance contamination arises from the scanning strategy used by the lidar. The assumption that the wind field is uniform across the scanning circle is often invalid in turbulent flow conditions. When velocity data from different parts of the scanning circle are combined to estimate raw wind speed components, changes in the wind field introduce additional variance, increasing uncertainty in the u, v, and w measurements [73]. Ground-based lidar systems also face challenges due to the complex interplay between surface reflectivity and vegetation cover. Natural surface heterogeneity, combined with varying angles of incidence and roughness, results in a broad range of reflective values, introducing further variability and uncertainty in measurements. Methods such as signal averaging, statistical filtering, and integrating auxiliary meteorological data can reduce the impact of variance contamination. These approaches enhance the reliability and accuracy of ground-based lidar measurements, thereby reducing uncertainty. As said by Newmann [114], the increase in variance due to contamination can counteract the effects of volume averaging, which as said before, reduces the lidar-estimated variance.

6.2.5 Terrain complexity

Several factors influence the geolocation uncertainty in lidar measurements. Vegetation and terrain conditions affect uncertainty. Complex terrain will give more uncertainties than flat terrain. As said by Hofsass et al. [115], correlations between wind speed measurements with masts or lidar systems show considerable differences in complex terrain, the reason being inhomogeneous flow conditions. In order to focus this research, it has been decided to keep the research in flat terrain, therefore the uncertainty due to terrain won't be reduced or quantified.

6.2.6 Difference to mast

As said by Clive [16], remote sensing devices obtain vector averages. When the lidar measurements of this project are compared with the measurements from the cup anemometer, these are compared with scalar averages. The problem here is that the scalar average will give an overprediction when compared with the vector average due to scalar inflation. Jensen's inequality, mentioned in section 4.1, can be seen as a consequence of the time average of the 1 Hz measurements generating a bias relative to the vector average, as mentioned by Black et al. [86]. This is where the perturbation adjustment can help solve part of the lidar bias. The statistical analysis in section 6.4 and the sensitivity analysis in section 6.5 will go into the change in bias when implementing this perturbation adjustment. Furthermore, a lidar only measures the radial velocity along the laser beam or the line-of-sight velocity. As said by Pena et al. [94], the measurement probe volumes from a ground-based lidar are larger than those of a cup or sonic anemometer, which could lead to the lidar having trouble measuring small turbulent eddies. Finally, uncertainty can arise due to the distance between the lidar and the meteorological mast. At the site used for this project, the distance between the two is 300 meters, which is significant enough for uncertainties to arise.

6.2.7 Uncertainty quantification

Table 6.1: Lidar uncertainties

Sub-Section	Description	Assumed Uncertainty	Adjustment effect
6.2.1	Instrument errors	$1-2\%$	None
6.2.2	Volume averaging	$3-5\%$	Decrease
6.2.3	Variance contamination	$1-2\%$	Decrease
6.2.4	Calibration errors	$2-3\%$ [108]	None
6.2.5	Terrain complexity	$2-3\%$ [108]	None
6.2.6	Difference to mast	5% [108]	Decrease

When using ground-based lidar to measure turbulence intensity, it's important to consider uncertainty to ensure the reliability and accuracy of the data. According to the lidar uncertainty standard review by B. Gribben [108], certain uncertainties have defined assumed values, as can be seen in Table 6.1. These values provide a foundational understanding of the primary sources of measurement variability. However, other uncertainties need to be quantified, including contamination uncertainty, which pertains to the potential interference from nearby reflective surfaces or atmospheric conditions, averaging uncertainty, arising from the lidar's measurement of an averaged value over a volume rather than a point, potentially smoothing out significant turbulence variations, and instrument uncertainty, related to the intrinsic noise generated by the lidar system itself. Accurate characterization and quantification of these additional uncertainties are essential for enhancing the precision of turbulence intensity measurements obtained through ground-based lidar systems.

While precise values for these uncertainties would ideally be derived from specific empirical studies or detailed simulations, educated estimates can be made based on typical lidar system performance and general measurement principles. Contamination uncertainty is generally influenced by the surrounding environment and atmospheric conditions, with an estimate ranging between $1-2\%$. Averaging uncertainty might reasonably be around $3-5\%$, depending on the spatial resolution and turbulence intensity. Instrument uncertainty, often characterized during the instrument's calibration, might fall within the range of $1-2\%$ for typical lidar systems. Combining these with the previously assumed uncertainties, the overall uncertainty can be approximated. However, it's important to note that these values are speculative and should ideally be validated through targeted experiments and rigorous statistical analysis. Next to that, some overlap is expected between the different uncertainties.

6.3 Derivation of uncertainty propagation equation

There are now two different formulas for TI. Equation 6.2 shows the generally used equation for TI [19, 116, 117], whereas Equation 6.3 shows the newly derived equation for TI, which is the TI formula for lidar sampling instead of the single-point anemometer sampling of Equation 6.2. To quantify and compare the uncertainties in both these equations, an uncertainty propagation equation has to be derived. For this derivation, the work done by Coleman and Steele [107] will be used.

$$TI = \frac{\sigma_U}{U} \tag{6.2}$$

$$TI = \sqrt{\frac{\overline{u'^2} * \overline{cos^2(\theta)} + Cov(u'^2, cos^2\theta)}{U^2_{mean}} + \frac{\overline{v'^2} * \overline{cos^2(\theta)} + Cov(v'^2, cos^2\theta)}{U^2_{mean}}} \tag{6.3}$$

For the derivation of an uncertainty propagation equation, a simpler two-variable case will be expressed first. Just like Coleman and Steele [107], a data reduction equation will be used (Equation 6.4). Where both variables will have systematic (β) and random (ϵ) errors, leading to Equation 6.5 and Equation 6.6. After using a Taylor series expansion and neglecting the remainder term, Equation 6.7 can be determined. Coleman and Steele assumed the remainder term to be negligible because it approaches zero more quickly than the first-order terms, as it contains the squares of the errors.

Using the ISO Guide to Uncertainty in Measurements ('GUM') [47], Equation 6.8 can be given as an equation for the expanded uncertainty, where the ISO guide argues that the error distribution of r can be considered Gaussian due to the central limit theorem [82, 107]. In this equation, b_i^2 is the estimate of the variance of the systematic error distribution, s_i^2 is the estimate of the variance of random error distribution, b_{ik} is an estimate of the covariance of the systematic errors in i and k, s_{ik} is an estimate of the covariance of the random errors in i and k, and lastly $\theta_i = \frac{\partial r}{\partial i}$ and $\theta_k = \frac{\partial r}{\partial k}$.

$$r = r(x, y) \tag{6.4}$$

$$x_k = x_{true} + \beta_{x_k} + \epsilon_{x_k} \tag{6.5}$$

$$y_k = y_{true} + \beta_{y_k} + \epsilon_{y_k} \tag{6.6}$$

$$(r_k - r_{true}) = \frac{\partial r}{\partial x}(x_k - x_{true}) + \frac{\partial r}{\partial y}(y_k - y_{true}) \tag{6.7}$$

$$\Upsilon_r = 2\sqrt{\sum_{i=1}^{J} \theta_i^2 b_i^2 + 2\sum_{i=1}^{J-1}\sum_{k=i+1}^{J} \theta_i\theta_k b_{ik} + \sum_{i=1}^{J} \theta_i^2 s_i^2 + 2\sum_{i=1}^{J-1}\sum_{k=i+1}^{J} \theta_i\theta_k s_{ik}} \tag{6.8}$$

Using Equation 6.8, the formulations for TI can be rewritten to quantify the uncertainties. In order to do this, the partial derivatives of the different variables have to be written down. For Equation 6.2, the formula depends on the variables σ and U, thus resulting in θ_σ being equal to $\frac{1}{U}$ and θ_U being equal to $-\frac{\sigma}{U^2}$. Equation 6.9 then follows from using these partial derivatives in Equation 6.8. For Equation 6.3, the formula can be split into two parts, in order to use Equation 6.8. After writing down all the partial derivatives of the equation, which are shown in section B.2, Equation 6.10 can be derived, where $R = A + B$. These two equations can now be used to quantify the uncertainties in both TI derivation methods.

$$\delta TI = \sqrt{\frac{\delta\sigma^2}{U^2} + \frac{\sigma^2\delta U^2}{U^4} - 2\frac{\sigma\delta\sigma\delta U}{U^3}s_{\sigma U}} \tag{6.9}$$

$$\delta TI = \frac{1}{2\sqrt{A+B}}\delta R \tag{6.10}$$

6.4 Statistical analysis

Expanding the formula for turbulence intensity using perturbation theory helps to consider additional sources of variability that are often overlooked in simpler formulations. By including terms related to the covariance of the velocity components and directional cosines, the expanded formula offers a more accurate representation of turbulence intensity. By accounting for the directional cosines, the expanded formula incorporates the effect of the orientation of the velocity fluctuations relative to the mean flow direction. This can reduce uncertainty

by providing a more accurate representation of the actual turbulence characteristics, especially in cases where the flow direction varies significantly. The covariance terms account for the relationship between the squared velocity fluctuations and the directional cosines. These terms help capture the joint variability between the velocity fluctuations and their directionality. Including these covariances reduces uncertainty by ensuring that the interplay between the magnitude of the fluctuations and their direction is properly represented.

Correlation analysis can be used to evaluate the performance of various lidar systems in comparison to a meteorological mast, like measuring turbulence intensity. Several approaches can be employed to assess the correlation between these datasets. Firstly, a Pearson correlation coefficient [118] can be calculated to determine the linear relationship between the turbulence intensity measurements from the lidars and the meteorological mast. This method quantifies the strength and direction of the linear relationship, providing a straightforward metric for comparison. Another approach is the Spearman rank correlation, which assesses the monotonic relationship between the variables [119]. This method is beneficial when the data do not necessarily follow a linear trend, allowing for a more robust comparison in the presence of outliers or non-linear associations. The explanation of the Pearson correlation coefficient and Spearman rank correlation can be found in section B.5 and section B.6, respectively. Additionally, a Bland-Altman plot can be used to visually inspect the agreement between the lidar and meteorological mast measurements. This plot helps identify any systematic biases and the limits of agreement between the two measurement techniques [120]. The Bland-Altman plots corresponding to Table 6.2, can be found in section F.6.

Table 6.2: Correlation analysis of turbulence intensity measurements

Adjustment	**Mean Diff**	**LoA Lower**	**LoA Upper**	**Pearson**	**Spearman**
LIDAR (no adjustment)	-0.0072	-0.1318	0.1174	0.473	0.566
ZX	0.0007	-0.1304	0.1317	0.474	0.566
Perturbation	0.0054	-0.1700	0.1808	0.383	0.516
Perturbation with O3	0.0049	-0.1686	0.1784	0.381	0.514
Perturbation with w component	0.0055	-0.1700	0.1811	0.384	0.516

The correlation analysis of turbulence intensity measurements between various lidar adjustment methods and a meteorological mast reveals several insights into their performance and agreement. For the standard lidar measurements without any adjustments, the mean difference in measurements is -0.0072, with limits of agreement (LoA) ranging from -0.1318 to 0.1174. The Pearson correlation coefficient is 0.473, indicating a moderate linear relationship, while the Spearman correlation coefficient of 0.566 suggests a stronger monotonic relationship. The ZX adjustment shows similar performance, with a mean difference of 0.0007 and LoA from -0.1304 to 0.1317. The Pearson correlation is slightly higher at 0.474, and the Spearman correlation remains the same at 0.566, indicating consistency in the monotonic relationship between the ZX adjustment and the meteorological mast. For the newly derived adjustment method, the mean difference is 0.0054 with a broader LoA from -0.1700 to 0.1808. This method shows a lower Pearson correlation of 0.383 and a Spearman correlation of 0.516, suggesting a weaker linear and monotonic relationship compared to the ZX adjustment method. Including the O3 component in the derivation yields a mean difference of 0.0049 and LoA from -0.1686 to 0.1784, with slightly lower Pearson and Spearman correlations of 0.381 and 0.514, respectively. These results indicate minimal impact on the correlation by including the O3 component. Similarly, incorporating the w component in the derivation results in a mean difference of 0.0055 and LoA from -0.1700 to 0.1811. The Pearson correlation remains consistent at 0.384, and the Spearman correlation at 0.516, indicating that the w component does not significantly alter the relationship between the derived measurements and the mast. Overall, while the ZX adjustment method shows moderate agreement and correlation with the mast, the various derivations demonstrate varying degrees of performance, with some components negatively impacting the correlation and agreement. This analysis underscores the importance of careful consideration of system components in optimizing lidar performance for turbulence intensity measurements.

6.5 Sensitivity analysis

According to Saltelli [121], sensitivity analysis is used to demonstrate how the uncertainty in the model output can be attributed to different sources of uncertainty in the model input. To conduct sensitivity analysis, it has been decided to expand the research involving the virtual turbulence box from 4 to 100 different turbulence boxes. This expansion will allow for the creation of a Monte Carlo simulation. As described by Mooney [122], a

Monte Carlo simulation assesses the behavior of a statistic in random samples by drawing lots of random samples and observing the behavior. Mooney calls the need for an "*artificial world*", which is done in this project with the creation of turbulence boxes. By using multiple turbulence boxes, different adjustment methods can be tested with various Mann parameters. This sensitivity analysis will enable further validation of the adjustment method. In this Monte Carlo analysis, a large number of potential outcomes were simulated based on the uncertainties identified in the measurements. The distribution of these simulated outcomes was then determined to understand the reliability of the uncertainty estimates. To conduct the Monte Carlo analysis, it was decided to simulate 100 different turbulence boxes. These boxes were used to test the perturbation adjustment method against the actual turbulence intensity in the turbulence box.

Mooney [122] explains that a Monte Carlo simulation is very simple in concept. It starts by generating data, which is done by letting the virtual lidar take samples from turbulence boxes with fixed turbulence parameters. The next step involves using the sample data and using this to arrive at the statistical situation of interest, in the case of this project this meant calculating the TI parameter. Then repeat this for several trials, in this project, it was decided to use 100 different turbulence boxes. When this is done, one of the leading turbulence parameters can be changed, and the process starts from the beginning again, thus creating Figure 6.1, Figure 6.2, Figure 6.3, and Figure 6.4.

6.5.1 Turbulent length scale simulation

As shown in Figure 6.1, over 100 different simulations, the adjustment method performed well against the actual TI of the turbulence box for different turbulent length scales. As previously shown in subsection 5.1.2, it is again evident that an increase in turbulence length scale leads to an increase in TI. When compared with the measurements taken by the lidar rings in Figure 6.2, it can be observed that the continuous measurements performed slightly better. The optimal performance of the adjustment will be further discussed with an error metrics analysis in subsection 6.5.3. When a small turbulence parameter $\alpha\epsilon^{2/3}$ is chosen, both methods seem to be suitable. Increasing this parameter in subsection 6.5.2 will show that a lidar starts overpredicting the TI. The results indicate a strong correlation between the two measures, highlighting the reliability of the adjusted lidar measurements for capturing turbulence characteristics in different scenarios.

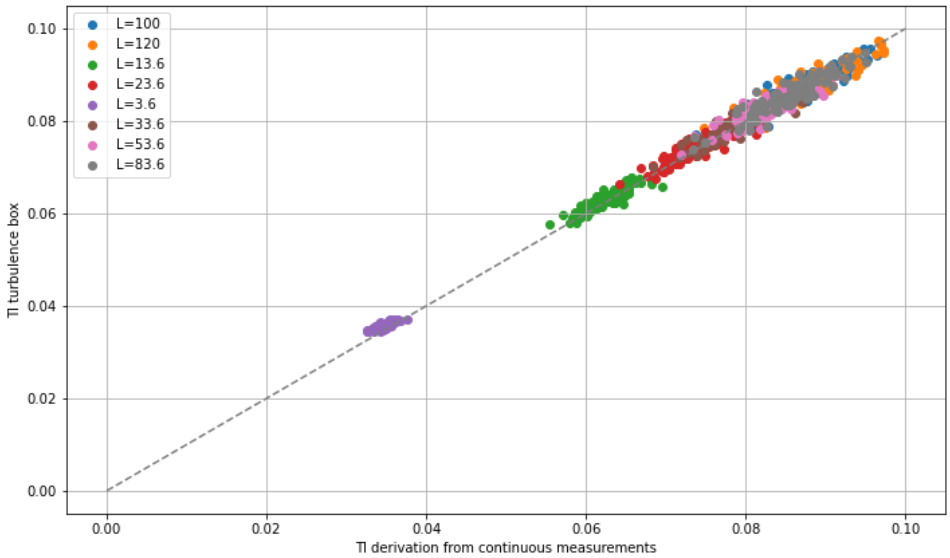

Figure 6.1: Comparison of the adjusted TI after continuous measurements for different turbulent length scales

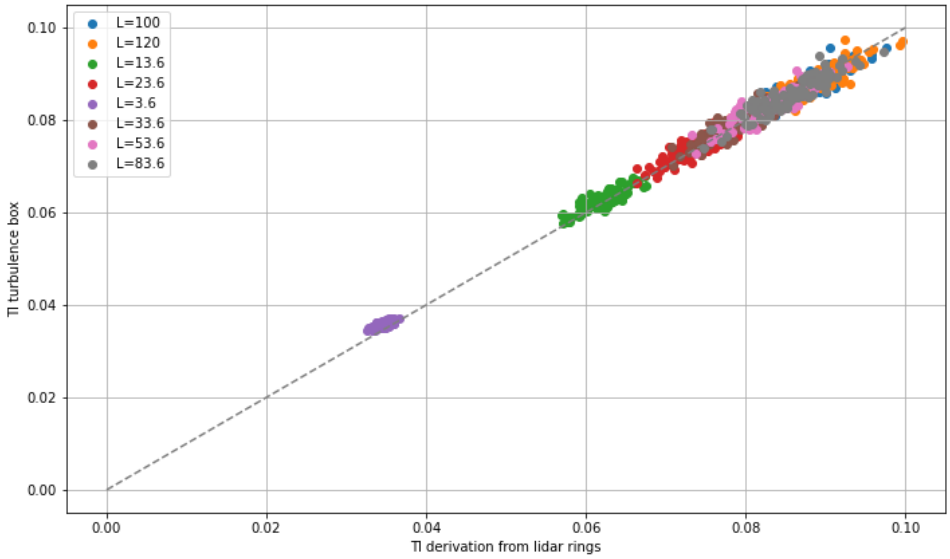

Figure 6.2: Comparison of the adjusted TI after lidar ring measurements for different turbulent length scales

6.5.2 Turbulence parameter simulation

The analysis of the turbulence parameters revealed that creating 100 simulations for different turbulence parameters may show more deviation from the actual TI since the adjustment method has not yet been tested in complex terrain. As can be seen in Figure 6.3 and Figure 6.4, when using the same turbulence parameter $\alpha\epsilon^{2/3}$ (denoted in the figures as ae), the derivation TI coming from the perturbation theory adjustment method, agrees well with the average mean turbulence from different virtual turbulence boxes. However, as said in section 5.1, an increase in this parameter will cause an increase in turbulence intensity, as is also evident in Figure 6.3 and Figure 6.4. As expected this leads to the lidar measurements to overpredict the TI in the virtual turbulence box.

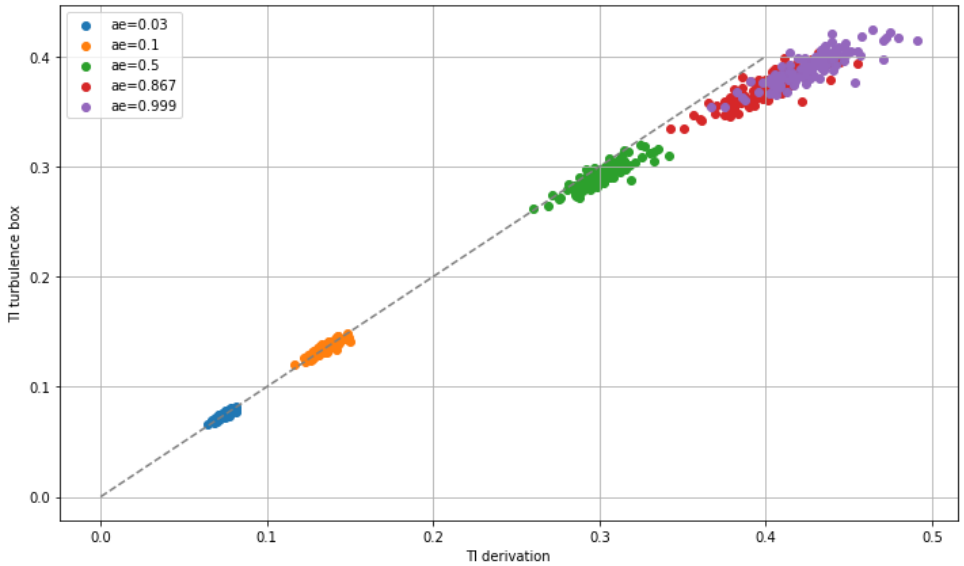

Figure 6.3: Comparison of the adjusted TI after continuous measurements for different turbulent parameters

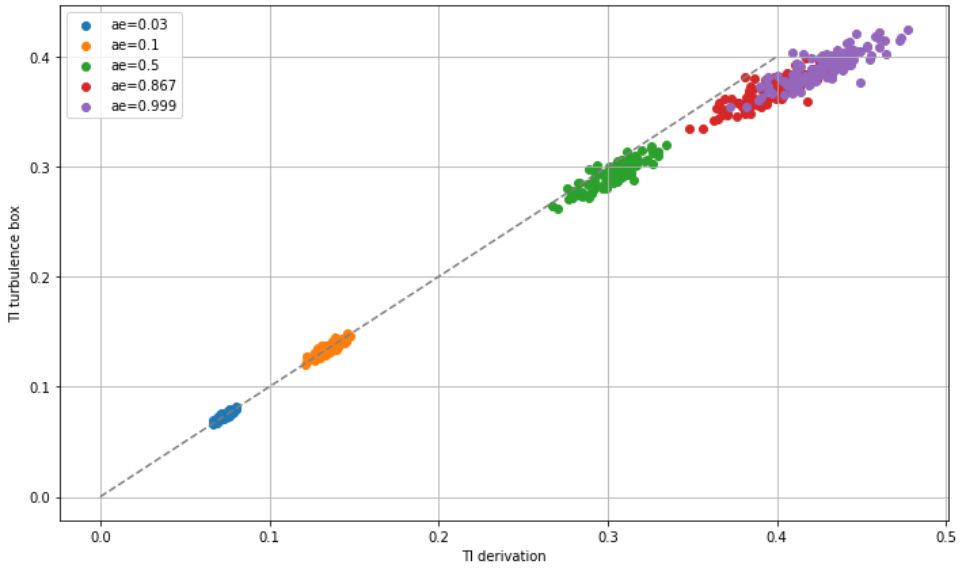

Figure 6.4: Comparison of the adjusted TI after lidar ring measurements for different turbulent parameters

6.5.3 Error metrics

The research used error metrics from the DNV report to test the adjustment method on data from a flat wind site. In this sensitivity analysis, incorporating these error metrics provides a better understanding of the adjustment method's performance. MRBE and RRMSE are calculated with respect to the mean average TI as given by the turbulence box. The cup anemometer does not agree well with the turbulence box, as shown in Figure F.21. When compared with the mean average TI of the turbulence box in Figure 6.5, both the adjusted lidar using the instant lidar ring scan and the adjusted lidar using the continuous scan outperform the lidar measurements without adjustment, showing promise for the use of this adjustment method. The ZX correction appears to overpredict the TI because the virtual lidar scan does not include the uncertainty of instrument noise, which is what the ZX correction is calibrated for.

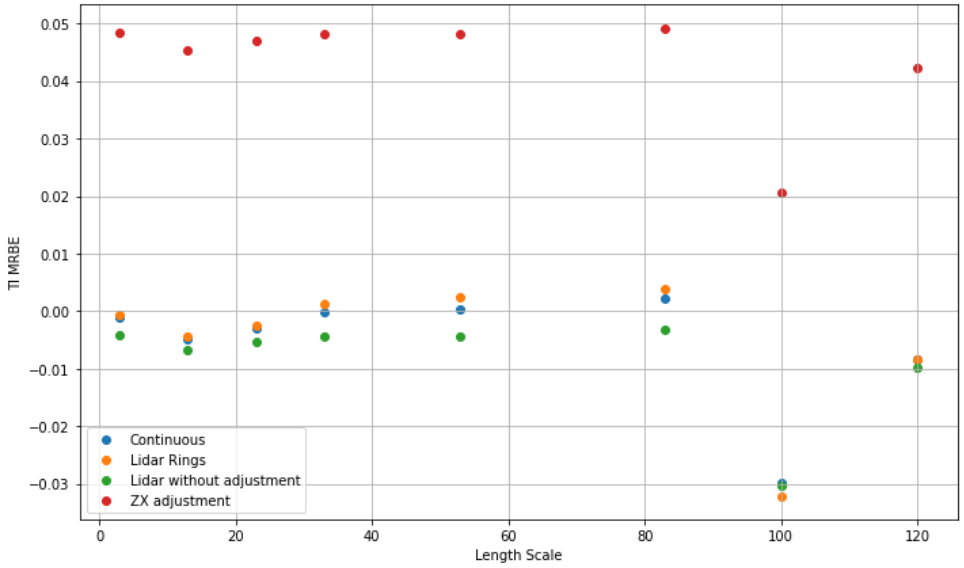

Figure 6.5: Comparison of the MRBE for different lidar TI adjustments

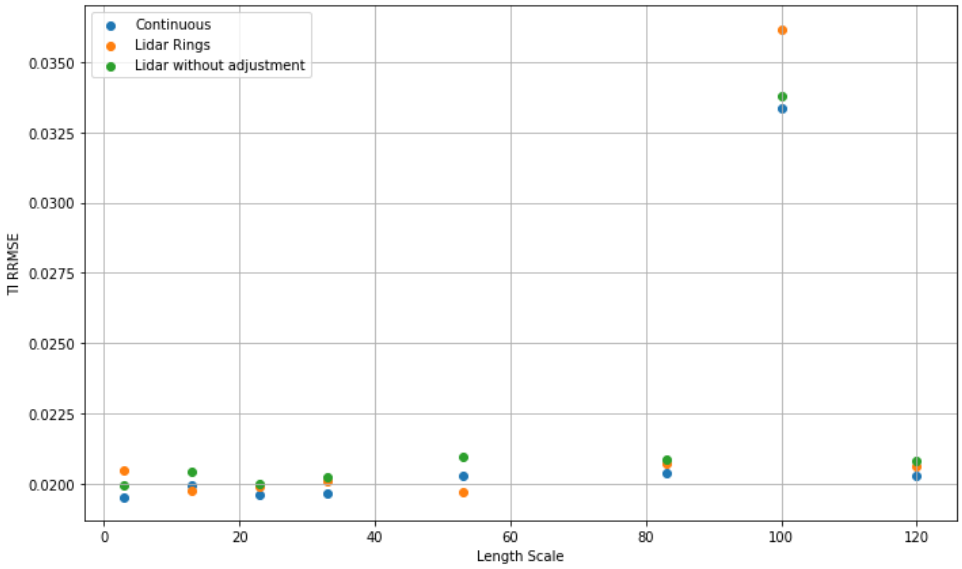

Figure 6.6: Comparison of the RRMSE for different lidar TI adjustments

Chapter 7

Acceptance of lidar TI measurements

Ground-based continuous-wave lidar turbulence intensity measurements are facing challenges in gaining widespread acceptance, as discussed in chapter 1. This section aims to evaluate the difficulties associated with accepting the use of lidar TI measurements. In chapter 2, three different theories of acceptance were proposed to quantify the challenges of accepting lidar measurements. Among these methods, the Technology Acceptance Model was considered the most suitable approach for this master's thesis work. However, it is recommended for further research to explore the possibilities of conducting an innovation diffusion theory analysis and a reliability theory analysis. This section will delve into the TAM developed by Davis and Venkatesh [102], and elaborate on how each aspect of the TAM relates to lidar technology. This information will be utilized to establish a lidar acceptance model, which will outline the key factors influencing lidar acceptance in the industry.

7.1 Technology Acceptance Model

Ground-based lidar technology has emerged as a critical tool in wind energy applications, particularly in wind farm assessments. This section aims to elucidate the TAM specific to ground-based lidar measurements in wind farms. TAM is a theoretical framework, introduced by Davis [123], widely used to understand users' acceptance and adoption of new technologies. In the context of wind energy, assessing the acceptance of ground-based lidar technology is pivotal for its effective integration into wind farm operations.

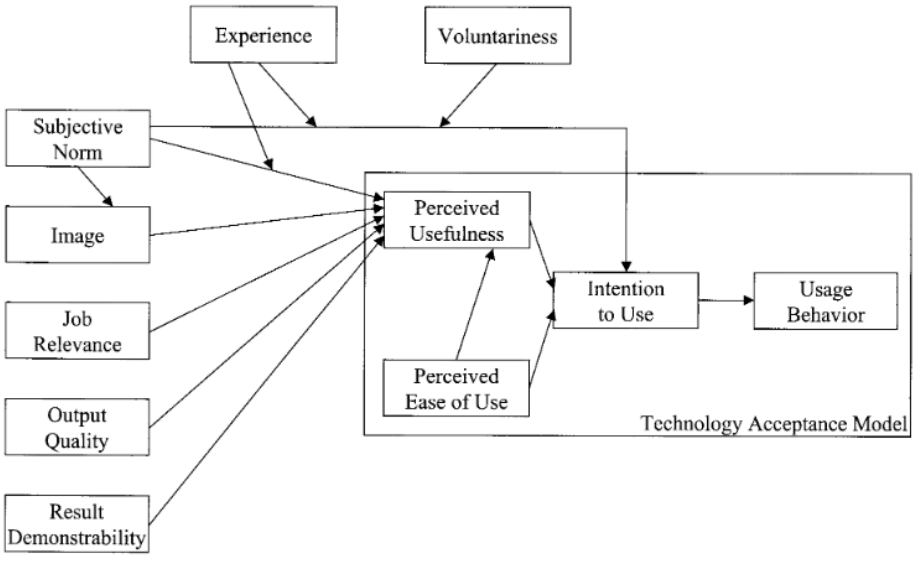

Figure 7.1: Technology Acceptance Model [2]

7.1.1 Social influence processes

Social influences play a significant role in the acceptance of technology within the wind energy sector. The Technology Acceptance Model (TAM) covers subjective norms, social factors, and external influences that affect an individual's attitude towards ground-based lidar technology. Subjective norm refers to the influence of others on a user's decision to use or not to use the technology [124]. In the case of lidar acceptance, this influence mainly

comes from competitors. As more competitors use lidar measurements for their wind projects, a company is more likely to use lidar for their wind measurements. Peers, colleagues, and industry experts' perceptions of ground-based lidar technology can influence individual attitudes. Positive endorsements and experiences shared within professional networks can enhance acceptance. Social factors, such as organizational culture, management support, and industry standards, shape the perception of ground-based lidar technology. Collaborative efforts and knowledge-sharing among industry stakeholders can foster acceptance. External influences, such as government policies, regulatory frameworks, and market trends, impact the adoption of ground-based lidar technology. Incentive programs, subsidies, and mandates promoting renewable energy adoption can drive acceptance.

The perception of ground-based lidar usage is changing for the better, thanks to the reduction in lidar uncertainty and the collaborative efforts of industry stakeholders. IEA Wind task 32 and DNV's RP have given a positive endorsement of lidar usage, which has been shared across a big professional network, increasing acceptance. Both of these efforts have focused on discussing the impact of lidar usage and, as a result, the social influence is expected to have a positive impact on the growing acceptance of ground-based lidar applications.

7.1.2 Cognitive instrumental processes

Figure 7.1 shows four cognitive instrumental determinants of perceived usefulness: job relevance, output quality, result demonstrability, and perceived ease of use. The argument presented is that people form perceived usefulness judgments by comparing what a system is capable of doing with what they need to get done in their job. To develop the theoretical basis for these instrumental determinants, recent developments in the reference paradigms upon which TAM's perceived usefulness construct was originally formulated are drawn. Job relevance is defined as an individual's perception regarding the degree to which the target system applies to his or her job [124]. Drawing from TAM, individuals' perceptions of how the technology aligns with their job requirements significantly influence their attitudes and intentions to use it. In the case of ground-based lidar, the decrease in uncertainty mostly influences jobs in the wind resource assessment of a wind park. Ground-based lidar technology's ability to streamline wind resource assessments, optimize turbine placement, and enhance performance monitoring directly impacts the job relevance for professionals involved in site selection, engineering, and maintenance within wind farms. The availability of accurate and real-time data from lidar measurements empowers decision-makers to make informed choices regarding wind farm planning, operations, and maintenance, thus enhancing job relevance for managerial and technical personnel.

Ground-based lidar measurements are increasingly relevant for wind farm operations. However, the uncertainty in data can lead to scepticism and reluctance among professionals, impacting their attitudes and intentions to use new technologies like lidar. Addressing this uncertainty directly aligns with the perceived usefulness and job relevance constructs of the TAM model, as discussed by Viswanath Venkatesh and Fred D. Davis [124]. By reducing uncertainty in lidar measurements, professionals tasked with site selection, turbine optimization, and operational planning can rely on accurate data to perform their duties effectively. This enhances the alignment of lidar technology with job roles and responsibilities within wind farm teams, leading to increased acceptance and utilization of the technology.

Output quality refers to how well a technology performs and the results it produces. In the case of wind lidar, output quality refers to how accurate, reliable, and useful the wind data provided by the lidar system is. The quality of the output directly affects how users perceive the system's usefulness and ease of use, which can influence whether they decide to use the technology. A study by IEA Wind Task 32 [8] found that output quality is an essential factor in determining the acceptance of wind lidar technology. This is because users need to know that the wind measurements provided by the lidar system are reliable and accurate. If the output quality is high, users are more likely to trust the technology and have a positive attitude towards using it. As users become more confident in the technology's ability to provide reliable and accurate wind measurements, they are more likely to see its usefulness. This means that as uncertainty about the output quality decreases, users are more likely to adopt wind lidar systems. Ultimately, this can lead to higher adoption rates within the wind energy sector.

Result demonstrability is defined by Moore and Benbasat [125] as the "tangibility of the results of using the innovation", directly impacting perceived usefulness within the TAM. Decreasing uncertainty in lidar turbulence intensity measurements enhances the tangibility and discernibility of results obtained from lidar technology. Turbulence intensity measurements are critical for assessing wind farm performance, identifying wake effects, and optimizing turbine operation. By improving the accuracy and reliability of turbulence intensity data, lidar technology enhances the clarity and visibility of its outcomes, thus enhancing result demonstrability. Enhanced result demonstrability positively influences perceived usefulness within the TAM framework. When users can readily attribute gains in their job performance to the use of lidar technology, they are more likely to perceive

it as useful. Reduced uncertainty in turbulence intensity measurements enables users to discern the direct impact of lidar data on their decision-making processes, reinforcing the perceived usefulness of the technology. The positive relationship between result demonstrability, perceived usefulness, and acceptance suggests that decreasing uncertainty in lidar turbulence intensity measurements can lead to increased acceptance of lidar technology within wind farm operations. When users can correlate the use of lidar with tangible improvements in wind farm performance, they are more likely to adopt and integrate the technology into their workflows. Reducing uncertainty in lidar turbulence intensity measurements not only improves the accuracy and reliability of data but also enhances the visibility of results, making them more demonstrable to users. This, in turn, boosts the perceived usefulness and acceptance of lidar technology within the wind energy sector, facilitating its broader adoption and utilization. Decreasing uncertainty in lidar turbulence intensity measurements directly impacts result demonstrability, perceived usefulness, and acceptance within the Technology Acceptance Model framework. By enhancing the tangibility of outcomes and enabling users to discern the direct impact of lidar data on their job performance, reduced uncertainty strengthens the case for adopting and integrating lidar technology into wind farm operations, driving innovation and efficiency in the renewable energy sector.

7.1.3 Perceived ease of use

Perceived ease of use, a fundamental component of the Technology Acceptance Model, directly influences perceived usefulness, thereby impacting acceptance of new technologies. According to Davis et al. [67], systems that are perceived as less effortful to use are more likely to enhance job performance. This section explores how reducing uncertainty in ground-based lidar measurements can enhance perceived ease of use and ultimately drive acceptance within wind farm operations. Decreasing uncertainty in ground-based lidar measurements reduces the cognitive load associated with interpreting and utilizing lidar data. High-quality, reliable data that are easily understandable require less mental effort from users, enhancing the perceived ease of use of lidar technology within wind farm operations. Reducing uncertainty in lidar measurements instils confidence among users regarding the reliability and accuracy of the technology. When users have confidence in the data provided by lidar systems, they perceive the technology as easier to use and integrate into their workflows, leading to greater acceptance. Clear and reliable lidar data, resulting from reduced uncertainty, streamline decision-making processes within wind farm operations. Users can make decisions more efficiently and with greater confidence when they have access to high-quality data, thereby perceiving the technology as easier to use and more beneficial to their job performance. Reducing uncertainty in lidar measurements may also lead to more effective training programs and user interfaces, further enhancing perceived ease of use. As users become more familiar with the technology and its capabilities, they are more likely to perceive it as easy to use and integrate into their daily tasks. The perceived ease of use of ground-based lidar technology is crucial for its acceptance within wind farm operations. By reducing uncertainty in lidar measurements, stakeholders can improve the user experience, streamline decision-making processes, and enhance user confidence, ultimately driving acceptance and utilization of lidar technology in the renewable energy sector. Reducing uncertainty in ground-based lidar measurements not only improves the accuracy and reliability of data but also enhances the perceived ease of use of the technology within wind farm operations. By streamlining decision-making processes, increasing user confidence, and facilitating effective training programs, reduced uncertainty drives acceptance and adoption of lidar technology, contributing to the advancement of renewable energy initiatives.

7.1.4 Perceived usefulness

The Technology Acceptance Model emphasizes the importance of perceived usefulness, which represents users' subjective evaluations of a technology's ability to improve their job performance or facilitate task completion [124]. In the wind energy sector, perceived usefulness refers to how professionals view ground-based lidar systems as valuable tools for optimizing various aspects of wind farm operations. Ground-based lidar technology provides real-time data on wind patterns, turbulence intensity, and other critical parameters essential for wind resource assessment, turbine placement, and performance monitoring within wind farms. This data allows decision-makers to make informed choices regarding site selection, operational planning, and maintenance strategies, ultimately enhancing the efficiency and profitability of wind energy projects. As lidar technology advances and improves data accuracy and reliability, stakeholders in the wind energy sector increasingly recognize its instrumental role in streamlining decision-making processes and optimizing operational outcomes.

Perceived usefulness is a key factor in the adoption and integration of ground-based lidar systems within wind farm operations. Professionals are more likely to embrace lidar technology when they see it as valuable for enhancing job performance, achieving operational objectives, and driving organizational success in the renewable energy domain. As stakeholders realize the tangible benefits of lidar systems in optimizing wind farm operations, the path towards widespread acceptance and utilization of lidar technology becomes increasingly clear, leading to a new era of innovation and efficiency in renewable energy endeavors.

7.1.5 Intentions to use

The intentions to use ground-based lidar technology are a critical aspect of TAM. They reflect individuals' inclinations and predispositions towards adopting a specific technology. In the context of wind energy applications, intentions to use represent professionals' perceptions of the relevance and potential benefits of integrating lidar systems into their operational workflows within wind farm management. Professionals in the wind energy sector are inclined to use ground-based lidar technology when they believe it can enhance job performance, help achieve operational objectives, and address key challenges in wind farm operations. As stakeholders recognize the instrumental role of lidar in providing accurate, real-time data on wind patterns, turbulence intensity, and other critical parameters, their intentions to leverage lidar systems as integral tools for decision-making and planning within wind farms are strengthened. Intentions to use ground-based lidar technology are influenced by various factors, including perceived usefulness, organizational support, perceived ease of use, and social influences. Individuals are more likely to embrace lidar technology when they perceive it as valuable for enhancing their job roles and responsibilities, and when they receive adequate support and resources from their organizations to integrate lidar systems into their operational workflows. Ultimately, intentions to use ground-based lidar technology within the wind energy sector serve as a precursor to actual adoption and utilization. As stakeholders exhibit positive intentions towards leveraging lidar systems for optimizing wind farm operations, the groundwork is laid for the widespread acceptance and integration of lidar technology into renewable energy practices.

7.1.6 Usage behaviour

The Technology Acceptance Model considers usage behavior as the observable adoption and utilization of a specific technology, representing the tangible expression of perceived usefulness and intentions to use. In the context of ground-based lidar technology for wind energy applications, usage behavior refers to the observable patterns of engagement, interaction, and integration of lidar systems within wind farm operations. Professionals within the wind energy sector exhibit usage behavior when they actively incorporate ground-based lidar technology into their decision-making processes, planning activities, and operational workflows within wind farms. Stakeholders use lidar data to inform site selection, optimize turbine placements, and monitor performance metrics, driving sustained adoption and utilization. Various factors influence usage behavior, including perceived usefulness, ease of use, organizational support, and external pressures. Individuals are more likely to embrace ground-based lidar technology when they perceive it as valuable for enhancing job performance, encounter minimal barriers to its use, and receive adequate support and resources from their organizations. Ultimately, usage behavior serves as an indicator of the effectiveness and relevance of ground-based lidar technology within the wind energy sector. As stakeholders demonstrate sustained engagement and integration of lidar systems into their operational workflows, the transformative potential of lidar technology in driving innovation and efficiency within renewable energy initiatives is realized, paving the way for continued advancements and evolution in wind farm management practices.

7.2 Lidar Acceptance Model

Based on the information from section 7.1, a lidar acceptance model can be developed, as shown in Figure 7.2. The model accounts for five external factors. Firstly, the lidar's data collection positively impacts its usefulness by effectively measuring wind at different heights, particularly at hub height, which met masts cannot do. This reduces uncertainty in wind assessment, as data doesn't need to be estimated from lower heights. Additionally, in large wind farms, where multiple met masts are needed, a lidar enhances performance monitoring and offers a better way to validate power curves [126], thus increasing its perceived usefulness. Although the impact of lidar on complex terrain is unclear in this project, it may be explored in future research. Finally, a lidar's flexibility and lower cost compared to met masts positively influence the intention to use. However, this project mainly focuses on lidar measurement uncertainty, which is perceived as the major hurdle to lidar acceptance. This uncertainty negatively affects the perceived usefulness and intention to use. If reducing uncertainty through perturbation adjustment is achieved, this negative influence on lidar acceptance will diminish, thus increasing the overall acceptance of lidar measurements.

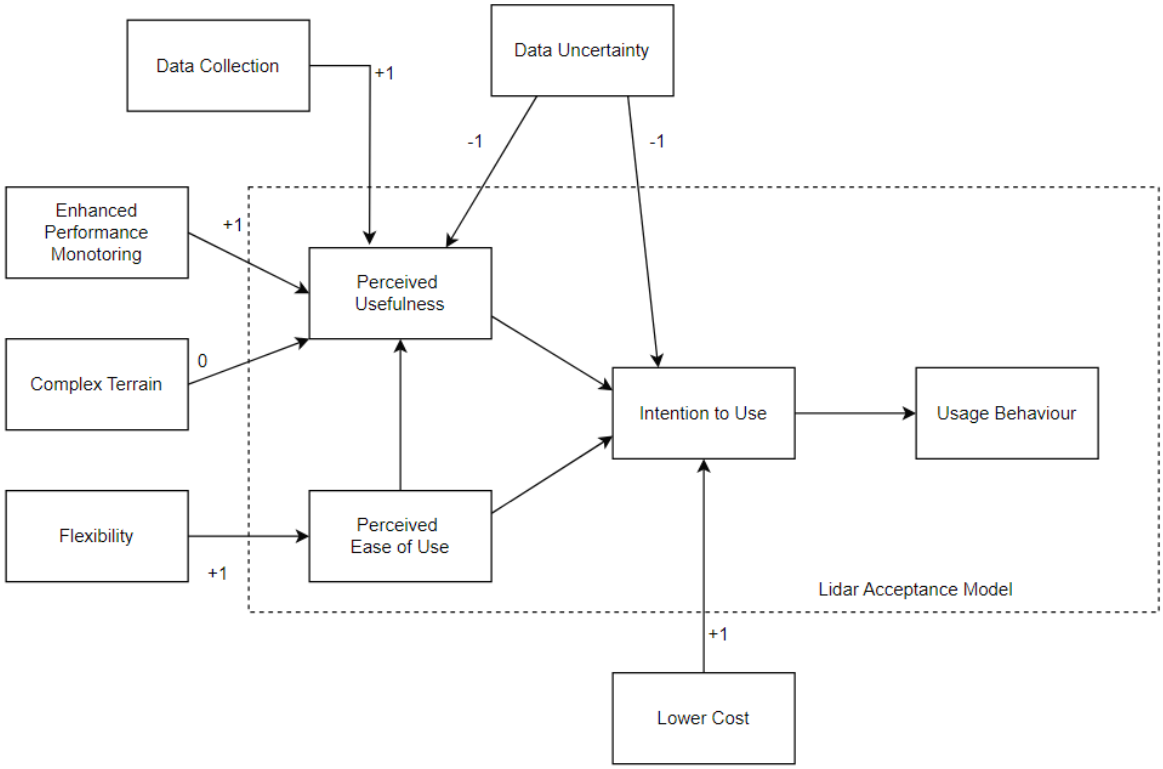

Figure 7.2: Lidar Acceptance Model

Chapter 8

Conclusions and recommendations

In this master's thesis work, the concept of using an adjustment method for ground-based lidar turbulence intensity measurements has been investigated. The main goal of this work is to see how much the uncertainty of ground-based lidar turbulence measurements decreases by implementing a perturbation theory-based adjustment. The answering of this question was split into three sub-questions, each of which can now be assessed.

This master's thesis seeks to assess how perturbation theory and recommended practices can help minimize uncertainties in predicting turbulence intensity using ground-based lidar. The research explores the potential uncertainties when perturbation theory is applied to turbulence intensity predictions using ground-based lidar. Initially, the study delves into the current state of ground-based lidar technology and turbulence measurements. A new equation for turbulence intensity is developed using perturbation theory, building upon prior work on mean wind speed by Black. This equation shows promise for further refinement with higher-order terms and consideration of 3D turbulence. The derived equation is validated against a Kaimal spectrum and demonstrates positive results. This newly derived equation serves as the basis for a turbulence intensity adjustment model, aiming to minimize uncertainties in lidar measurements. Following the creation of this adjustment model, an uncertainty analysis is performed to ascertain the expected uncertainties in the new turbulence intensity predictions. The analysis reveals that implementing a perturbation theory-based adjustment on the lidar data can reduce uncertainties in volume averaging, variance contamination, and the differences between the lidar and the cup anemometer. The adjustment method follows the principles of a previously developed adjustment model, L-TERRA. Consequently, this research successfully predicts the magnitudes of uncertainty when employing the new adjustment method.

In order to test the adjustment method, the DNV joint industry project report was utilized. The aim was to reduce uncertainties in ground-based lidar turbulence measurement and see how well the adjustment method followed the insights from the joint industry project when implemented in a flat wind site. Before delving into the insights of the DNV report, the data provided by Vattenfall was analyzed. This report presents an analysis of wind data from a Vattenfall wind site in the southern Netherlands, highlighting its relevance in the context of DNV's joint industry project. The research follows the IEC criteria to ensure a methodically accurate approach to evaluating wind energy sites. The data analysis process involves filtering, layering by height, and aligning by column names to address data misalignment and the dynamic characteristics of the wind site. The integration of a machine-learning model, particularly an LSTM model, was also explored to enhance data precision. The analysis encompasses the comparison of un-interpolated, interpolated, and machine-learning-adjusted datasets, with a focus on the TI parameter. Error metrics, wind roses, and statistical analyses provide a comprehensive understanding of the discrepancies and agreements between lidar and met mast measurements. It became clear that an adjustment method was needed to lower the error metrics because interpolation and machine learning did not offer sufficient solutions. The created adjustment method was first tested in a virtual environment, which was created with the help of DTU's Hipersim. Following the creation of different turbulence boxes and a virtual ground-based continuous-wave lidar capable of doing lidar scans in the virtual environment, different variations of the adjustment method could be tested. A statement made in literature by Sathe et al was also proven, as the continuous lidar scan showed similar results as the instant lidar rings scan in various turbulence boxes. The adjustment method was proven to work well for different turbulence parameters, as a change in turbulence length scale proved a great alignment, and a change in turbulence parameter showed an expected overprediction due to more complex turbulent structures. Using the error metrics given in the DNV report, the adjustment method was tested against the original lidar TI predictions and the correction done by Zephyr and was shown to perform well at different heights. Therefore the lidar TI adjustment method follows the insights from the joint industry project well.

After implementing and testing the adjustment method, it was important to assess how this research contributes to the increased acceptance of using lidar technology to measure turbulence at flat wind sites. This assessment was carried out through the implementation of a lidar acceptance model, based on the technology acceptance model introduced by Davis. The lidar acceptance model depends on data uncertainty, data collection, performance monitoring, complex terrain, ease of use, and cost. The report has demonstrated that the negative impact of data uncertainty on perceived usefulness and intention to use can be addressed by implementing an adjustment method for predicting ground-based lidar turbulence intensity. Therefore, an adjustment method can improve the overall acceptance of using ground-based lidar technology in wind resource assessment.

This master's thesis project has introduced a new method for adjusting ground-based lidar turbulence intensity predictions. However, as noted in this report, there is room for improvement and additional features in this adjustment method. Therefore, further recommendations will be provided to conclude this report. Firstly, the adjustment method can be tested on larger datasets. One limitation of the current dataset is that it only includes two months of overlapping data between the cup anemometer measurements and lidar measurements. A larger dataset could help enhance the adjustment method. Additionally, utilizing multiple datasets can assist in cross-validating the results. The adjustment model can also be enhanced by incorporating a machine learning correction, such as a random forest model, which has shown promising results for this dataset. As recommended by the DNV report, the use of LSTM models with larger datasets can also help reduce uncertainties in lidar TI measurements. The current turbulence intensity equation is designed for flat terrain, but it is recommended to explore its extension for complex terrain, as demonstrated by previous research on mean wind speed. Furthermore, further research can be conducted to quantify the decrease in uncertainty, including an uncertainty analysis on ground-based lidar with and without the implemented adjustment method. The sensitivity analysis can also be expanded by varying more turbulent components in the different turbulence boxes. Lastly, the lidar acceptance model can be tested and applied to different lidar acceptance issues, with further research focusing on extending or modifying the model.

The primary goal of this thesis was to reduce the uncertainty of ground-based lidar turbulence measurements using a perturbation theory adjustment. Several steps were taken to achieve this objective. Firstly, the project investigated the potential of perturbation theory in quantifying uncertainties in turbulence intensity predictions obtained by ground-based lidar. Building upon previous work on mean wind speed, a new equation for turbulence intensity was developed. Multiple analyses demonstrated that applying the perturbation adjustment to the lidar measurements resulted in an improved lidar/cup ratio, indicating that the lidar measurements closely aligned with the met mast measurements. The perturbation adjustment closely matched the adjustment made by Zephyr, showing the promise of using physics-based adjustments, such as L-TERRA. Additionally, the JIP report was referenced to establish acceptance criteria. The report provided error limits for MBRE and RRMSE values. The new adjustment mostly aligned with these boundaries, although it was limited by the available measurement data. Future research could benefit from using datasets with a greater overlap between lidar and met mast measurements. Lastly, the study explored lidar acceptance by examining the various factors influencing it. Analysis of the lidar acceptance model revealed that reducing uncertainties in lidar measurements would enhance the acceptance of lidar measurements. Implementing the perturbation adjustment method is therefore expected to improve lidar acceptance.

Bibliography

[1] M. Wei, W. Chong, J. Cao, T. Zhou, and D. Zheng, "Uncertainty evaluation for wind speed measurement part (1):"gum method and monte carlo method"," *Flow Measurement and Instrumentation*, vol. 97, p. 102607, 2024.

[2] V. Venkatesh and F. D. Davis, "A theoretical extension of the technology acceptance model: Four longitudinal field studies," *Management science*, vol. 46, no. 2, pp. 186–204, 2000.

[3] H. Ritchie, P. Rosado, and M. Roser, "Energy production and consumption," *Our World in Data*, 2020. https://ourworldindata.org/energy-production-consumption.

[4] S. Shafiee and E. Topal, "When will fossil fuel reserves be diminished?," *Energy policy*, vol. 37, no. 1, pp. 181–189, 2009.

[5] A. Scholbrock, P. Fleming, D. Schlipf, A. Wright, K. Johnson, and N. Wang, "Lidar-enhanced wind turbine control: Past, present, and future," in *2016 American Control Conference (ACC)*, pp. 1399–1406, IEEE, 2016.

[6] S. Raach, D. Schlipf, J. Trujillo, and P. Cheng, "Model-based wake tracking using lidar measurements for wind farm control," *Large Wind-Power Plants: Interaction, Control and Integration*, p. 2015, 2015.

[7] L. M. Bardal and L. R. Sætran, "Influence of turbulence intensity on wind turbine power curves," *Energy Procedia*, vol. 137, pp. 553–558, 2017.

[8] A. Clifton, P. Clive, J. Gottschall, D. Schlipf, E. Simley, L. Simmons, D. Stein, D. Trabucchi, N. Vasiljevic, and I. Würth, "Iea wind task 32: Wind lidar identifying and mitigating barriers to the adoption of wind lidar," *Remote Sensing*, vol. 10, no. 3, p. 406, 2018.

[9] S. Emeis, M. Harris, and R. M. Banta, "Boundary-layer anemometry by optical remote sensing for wind energy applications," *Meteorologische Zeitschrift*, vol. 16, no. 4, pp. 337–348, 2007.

[10] K. Browning and R. Wexler, "The determination of kinematic properties of a wind field using doppler radar," *Journal of Applied meteorology and climatology*, vol. 7, no. 1, pp. 105–113, 1968.

[11] R. Kropfli, "Single doppler radar measurements of turbulence profiles in the convective boundary layer," *Journal of Atmospheric and Oceanic Technology*, vol. 3, no. 2, pp. 305–314, 1986.

[12] M. R. Watts, C. Poulton, M. Byrd, and G. Smolka, "Lidar on a chip enters the fast lane: Sensors for self-driving cars and robots will be tiny, reliable, and affordable," *IEEE Spectrum*, vol. 60, no. 9, pp. 38–43, 2023.

[13] A. Sathe, R. Banta, L. Pauscher, K. Vogstad, D. Schlipf, and S. Wylie, "Estimating turbulence statistics and parameters from ground-and nacelle-based lidar measurements: Iea wind expert report," 2015.

[14] A. Sathe and J. Mann, "A review of turbulence measurements using ground-based wind lidars," *Atmospheric Measurement Techniques*, vol. 6, no. 11, pp. 3147–3167, 2013.

[15] D. Kim, T. Kim, G. Oh, J. Huh, and K. Ko, "A comparison of ground-based lidar and met mast wind measurements for wind resource assessment over various terrain conditions," *Journal of Wind Engineering and Industrial Aerodynamics*, vol. 158, pp. 109–121, 2016.

[16] P. J. M. Clive, "Compensation of vector and volume averaging bias in lidar wind speed measurements," *IOP Conference Series: Earth and Environmental Science*, vol. 1, p. 012036, may 2008.

[17] W. Zhang, C. D. Markfort, and F. Porté-Agel, "Near-wake flow structure downwind of a wind turbine in a turbulent boundary layer," *Experiments in fluids*, vol. 52, pp. 1219–1235, 2012.

[18] J. C. Kaimal and J. J. Finnigan, *Atmospheric boundary layer flows: their structure and measurement*. Oxford university press, 1994.

[19] G. Ren, J. Liu, J. Wan, F. Li, Y. Guo, and D. Yu, "The analysis of turbulence intensity based on wind speed data in onshore wind farms," *Renewable Energy*, vol. 123, pp. 756–766, 2018.

[20] K. Kaiser, W. Langreder, H. Hohlen, and J. Højstrup, "Turbulence correction for power curves," in *Wind Energy: Proceedings of the Euromech Colloquium*, pp. 159–162, Springer, 2007.

[21] L. M. Bardal and L. R. Sætran, "Influence of turbulence intensity on wind turbine power curves," *Energy Procedia*, vol. 137, pp. 553–558, 2017. 14th Deep Sea Offshore Wind RD Conference, EERA DeepWind'2017.

[22] M. M. Hand, N. D. Kelley, and M. J. Balas, "Identification of wind turbine response to turbulent inflow structures," in *Fluids Engineering Division Summer Meeting*, vol. 36967, pp. 2557–2566, 2003.

[23] N. Carpman, "Turbulence intensity in complex environments and its influence on small wind turbines," 2011.

[24] G. I. Taylor, "The spectrum of turbulence," *Proceedings of the Royal Society of London. Series A-Mathematical and Physical Sciences*, vol. 164, no. 919, pp. 476–490, 1938.

[25] I. IEC, "61400-1: Wind turbines part 1: Design requirements," *International Electrotechnical Commission*, vol. 177, 2005.

[26] "11.4 frozen: The taylor hypothesis." `https://www.e-education.psu.edu/meteo300/node/737`. Accessed: 2024-03-30.

[27] B. M. Sumer and D. R. Fuhrman, *Turbulence in coastal and civil engineering*, vol. 51. World Scientific, 2020.

[28] A. H. Black, J.-P. Cariou, and F. Delbos, "Development of a generalized framework for point and lidar measurement sensitivities in turbulent, complex flow," 2023.

[29] P. Rosenbusch, P. Mazoyer, L. Pontreau, P. E. Allain, and J.-P. Cariou, "Wind speed reconstruction from mono-static wind lidar eliminating the effect of turbulence," *Journal of Renewable and Sustainable Energy*, vol. 13, no. 6, 2021.

[30] R. Robey and J. K. Lundquist, "Behavior and mechanisms of doppler wind lidar error in varying stability regimes," *Atmospheric Measurement Techniques*, vol. 15, no. 15, pp. 4585–4622, 2022.

[31] S. Knoop, F. C. Bosveld, M. J. de Haij, and A. Apituley, "A 2-year intercomparison of continuous-wave focusing wind lidar and tall mast wind measurements at cabauw," *Atmospheric Measurement Techniques*, vol. 14, no. 3, pp. 2219–2235, 2021.

[32] C. Slinger and M. Harris, "Introduction to continuous-wave doppler lidar," *Summer School in Remote Sensing for Wind Energy, Boulder, USA*, vol. 11, 2012.

[33] D. A. Smith, M. Harris, A. S. Coffey, T. Mikkelsen, H. E. Jørgensen, J. Mann, and R. Danielian, "Wind lidar evaluation at the danish wind test site in høvsøre," *Wind Energy: An International Journal for Progress and Applications in Wind Power Conversion Technology*, vol. 9, no. 1-2, pp. 87–93, 2006.

[34] D. Kindler, A. Oldroyd, A. Macaskill, and D. Finch, "Acourtr system. preliminary results," *Meteorologische Zeitschrift (Berlin)*, vol. 16, 2007.

[35] M. Courtney, R. Wagner, and P. Lindelöw, "Testing and comparison of lidars for profile and turbulence measurements in wind energy," in *IOP Conference Series: Earth and Environmental Science*, vol. 1, p. 012021, IOP Publishing, 2008.

[36] S.-E. Gryning, E. Batchvarova, B. Brümmer, H. Jørgensen, and S. Larsen, "On the extension of the wind profile over homogeneous terrain beyond the surface boundary layer," *Boundary-layer meteorology*, vol. 124, pp. 251–268, 2007.

[37] A. Sathe, J. Mann, T. Barlas, W. Bierbooms, and G. Van Bussel, "Influence of atmospheric stability on wind turbine loads," *Wind energy*, vol. 16, no. 7, pp. 1013–1032, 2013.

[38] C. M. St Martin, J. K. Lundquist, A. Clifton, G. S. Poulos, and S. J. Schreck, "Wind turbine power production and annual energy production depend on atmospheric stability and turbulence," *Wind Energy Science*, vol. 1, no. 2, pp. 221–236, 2016.

[39] M. Kelly and S.-E. Gryning, "Long-term mean wind profiles based on similarity theory," *Boundary-layer meteorology*, vol. 136, pp. 377–390, 2010.

[40] "Pasquill stability classes." `https://www.ready.noaa.gov/READYpgclass.php`. Accessed: 2024-07-24.

[41] W. G. Van Sark, H. C. Van der Velde, J. P. Coelingh, and W. A. Bierbooms, "Do we really need rotor equivalent wind speed?," *Wind Energy*, vol. 22, no. 6, pp. 745–763, 2019.

[42] X. Shen, X. Zhu, and Z. Du, "Wind turbine aerodynamics and loads control in wind shear flow," *Energy*, vol. 36, no. 3, pp. 1424–1434, 2011.

[43] P. Kundu, I. Cohen, and D. Dowling, "Fluid mechanics 6th ed. isbn: 9780124059351," 2016.

[44] P. Murphy, J. K. Lundquist, and P. Fleming, "How wind speed shear and directional veer affect the power production of a megawatt-scale operational wind turbine," *Wind Energy Science Discussions*, vol. 2019, pp. 1–46, 2019.

[45] "IEC 61400-12-1:2022 Wind energy generation systems - Part 12-1: Power performance measurements of electricity producing wind turbines," 9 2022. Published on 2022-09-05.

[46] R. Wagner, I. Antoniou, S. M. Pedersen, M. S. Courtney, and H. E. Jørgensen, "The influence of the wind speed profile on wind turbine performance measurements," *Wind Energy: An International Journal for Progress and Applications in Wind Power Conversion Technology*, vol. 12, no. 4, pp. 348–362, 2009.

[47] I. ISO. and B. OIML, *Guide to the Expression of Uncertainty in Measurement*. Aenor, 1993.

[48] S. Pindado, J. Cubas, and F. Sorribes-Palmer, "The cup anemometer, a fundamental meteorological instrument for the wind energy industry. research at the idr/upm institute," *Sensors*, vol. 14, no. 11, pp. 21418–21452, 2014.

[49] N. Dimitrov, A. Borraccino, A. Peña, A. Natarajan, and J. Mann, "Wind turbine load validation using lidar-based wind retrievals," *Wind Energy*, vol. 22, no. 11, pp. 1512–1533, 2019.

[50] J. F. Newman, A. Clifton, M. J. Churchfield, and P. Klein, "Improving lidar turbulence estimates for wind energy," in *Journal of Physics: Conference Series*, vol. 753, p. 072010, IOP Publishing, 2016.

[51] A. Sathe, J. Mann, J. Gottschall, and M. S. Courtney, "Can wind lidars measure turbulence?," *Journal of Atmospheric and Oceanic Technology*, vol. 28, no. 7, pp. 853–868, 2011.

[52] G. Alfonsi, "Reynolds-averaged navier–stokes equations for turbulence modeling," 2009.

[53] P. M. Stevenson, "Optimized perturbation theory," *Physical Review D*, vol. 23, no. 12, p. 2916, 1981.

[54] A. Borraccino, M. Courtney, and R. Wagner, "Generic methodology for field calibration of nacelle-based wind lidars," *Remote Sensing*, vol. 8, no. 11, p. 907, 2016.

[55] W. Niemeier and D. Tengen, "Uncertainty assessment in geodetic network adjustment by combining gum and monte-carlo-simulations," *Journal of Applied Geodesy*, vol. 11, no. 2, pp. 67–76, 2017.

[56] D. Kim, T. Kim, G. Oh, J. Huh, and K. Ko, "A comparison of ground-based lidar and met mast wind measurements for wind resource assessment over various terrain conditions," *Journal of Wind Engineering and Industrial Aerodynamics*, vol. 158, pp. 109–121, 2016.

[57] L. Kristensen, "Cup anemometer behavior in turbulent environments," *Journal of Atmospheric and Oceanic Technology*, vol. 15, no. 1, pp. 5–17, 1998.

[58] K. Papadopoulos, N. Stefantos, U. S. Paulsen, and E. Morfiadakis, "Effects of turbulence and flow inclination on the performance of cup anemometers in the field," *Boundary-Layer Meteorology*, vol. 101, pp. 77–107, 2001.

[59] T. F. Pedersen, *Development of a Classification System for Cup Anemometers-CLASSCUP*. 2003.

[60] J. P. Goit, S. Shimada, and T. Kogaki, "Can lidars replace meteorological masts in wind energy?," *Energies*, vol. 12, no. 19, p. 3680, 2019.

[61] A. Albers, A. W. Janssen, and J. Mander, "How to gain acceptance for lidar measurements," in *Procedings of DEWEK Conference*, 2010.

[62] J. Newman, A. Clifton, M. Churchfield, and P. Klein, "Improving lidar turbulence estimates for wind energy," vol. 753, 2016. Cited by: 0; All Open Access, Gold Open Access, Green Open Access.

[63] F. Kelberlau and J. Mann, "Cross-contamination effect on turbulence spectra from doppler beam swinging wind lidar," *Wind Energy Science*, vol. 5, no. 2, pp. 519–541, 2020.

[64] M. Iarlori, F. Madonna, V. Rizi, T. Trickl, and A. Amodeo, "Effective resolution concepts for lidar observations," *Atmospheric Measurement Techniques*, vol. 8, no. 12, pp. 5157–5176, 2015.

[65] J. G. Simmonds and J. E. Mann Jr, *A first look at perturbation theory*. Courier Corporation, 1998.

[66] N. Marangunić and A. Granić, "Technology acceptance model: a literature review from 1986 to 2013," *Universal access in the information society*, vol. 14, pp. 81–95, 2015.

[67] F. D. Davis, *A technology acceptance model for empirically testing new end-user information systems: Theory and results*. PhD thesis, Massachusetts Institute of Technology, 1985.

[68] G. Hübner, V. Leschinger, F. J. Müller, and J. Pohl, "Broadening the social acceptance of wind energy–an integrated acceptance model," *Energy Policy*, vol. 173, p. 113360, 2023.

[69] T. A. Wani and S. Ali, "Innovation diffusion theory," *Journal of general management research*, vol. 3, no. 2, pp. 101–118, 2015.

[70] I. Sahin, "Detailed review of rogers' diffusion of innovations theory and educational technology-related studies based on rogers' theory.," *Turkish Online Journal of Educational Technology-TOJET*, vol. 5, no. 2, pp. 14–23, 2006.

[71] L. Alhmoud and B. Wang, "A review of the state-of-the-art in wind-energy reliability analysis," *Renewable and Sustainable Energy Reviews*, vol. 81, pp. 1643–1651, 2018.

[72] D. Giavarina, "Understanding bland altman analysis," *Biochemia medica*, vol. 25, no. 2, pp. 141–151, 2015.

[73] J. F. Newman and A. Clifton, "An error reduction algorithm to improve lidar turbulence estimates for wind energy," *Wind Energy Science*, vol. 2, no. 1, pp. 77–95, 2017.

[74] G. H. Ryu, D. Kim, D.-Y. Kim, Y.-G. Kim, S. J. Kwak, M. S. Choi, W. Jeon, B.-S. Kim, and C.-J. Moon, "Analysis of vertical wind shear effects on offshore wind energy prediction accuracy applying rotor equivalent wind speed and the relationship with atmospheric stability," *Applied sciences*, vol. 12, no. 14, p. 6949, 2022.

[75] D. Vickers and L. Mahrt, "Quality control and flux sampling problems for tower and aircraft data," *Journal of atmospheric and oceanic technology*, vol. 14, no. 3, pp. 512–526, 1997.

[76] G. K. Uyanık and N. Güler, "A study on multiple linear regression analysis," *Procedia-Social and Behavioral Sciences*, vol. 106, pp. 234–240, 2013.

[77] M. Tranmer and M. Elliot, "Multiple linear regression," *The Cathie Marsh Centre for Census and Survey Research (CCSR)*, vol. 5, no. 5, pp. 1–5, 2008.

[78] "Linearregression." `https://scikit-learn.org/stable/modules/generated/sklearn.linear_model.LinearRegression.html`. Accessed: 2024-07-24.

[79] Å. Björck, "Least squares methods," *Handbook of numerical analysis*, vol. 1, pp. 465–652, 1990.

[80] V. Bulaevskaya, S. Wharton, A. Clifton, G. Qualley, and W. Miller, "Wind power curve modeling in complex terrain using statistical models," *Journal of Renewable and Sustainable Energy*, vol. 7, no. 1, 2015.

[81] A. Clifton, L. Kilcher, J. Lundquist, and P. Fleming, "Using machine learning to predict wind turbine power output," *Environmental research letters*, vol. 8, no. 2, p. 024009, 2013.

[82] F. M. Dekking, *A Modern Introduction to Probability and Statistics: Understanding why and how*. Springer Science & Business Media, 2005.

[83] D. J. Griffiths, *Introduction to electrodynamics*. Cambridge University Press, 2023.

[84] A. Ben-Israel and T. N. Greville, *Generalized inverses: theory and applications*. Springer Science & Business Media, 2006.

[85] S. Chountasis, V. N. Katsikis, D. Pappas, *et al.*, "Applications of the moore-penrose inverse in digital image restoration," *Mathematical Problems in Engineering*, vol. 2009, p. 170724, 2009.

[86] A. Black, J. Lundquist, C. Montavon, and R. Robey, "Behavior and mechanisms of doppler wind lidar error in complex terrain: stable flow case study at perdigão," in *Journal of Physics: Conference Series*, vol. 2767, p. 052062, IOP Publishing, 2024.

[87] L. Dong, W. H. Lio, and E. Simley, "On turbulence models and lidar measurements for wind turbine control," *Wind Energy Science*, vol. 6, no. 6, pp. 1491–1500, 2021.

[88] N. Dimitrov, M. Pedersen, and Ásta Hannesdóttir, "An open-source python-based tool for mann turbulence generation with constraints and non-gaussian capabilities," *Journal of Physics: Conference Series*, vol. 2767, p. 052058, jun 2024.

[89] J. Mann, "The spatial structure of neutral atmospheric surface-layer turbulence," *Journal of fluid mechanics*, vol. 273, pp. 141–168, 1994.

[90] M. McWilliam, N. Bonfils, N. K. Dimitrov, and S. Dou, "Wind farm parameterization and turbulent wind box generation," 2022.

[91] J. Berg, A. Natarajan, J. Mann, and E. G. Patton, "Gaussian vs non-gaussian turbulence: impact on wind turbine loads," *Wind Energy*, vol. 19, no. 11, pp. 1975–1989, 2016.

[92] N. Dimitrov, A. Natarajan, and J. Mann, "Effects of normal and extreme turbulence spectral parameters on wind turbine loads," *Renewable Energy*, vol. 101, pp. 1180–1193, 2017.

[93] J. Mann, "Wind field simulation," *Probabilistic engineering mechanics*, vol. 13, no. 4, pp. 269–282, 1998.

[94] A. Peña, J. Mann, and N. Dimitrov, "Turbulence characterization from a forward-looking nacelle lidar," *Wind Energy Science*, vol. 2, no. 1, pp. 133–152, 2017.

[95] M. Kelly, "From standard wind measurements to spectral characterization: turbulence length scale and distribution," *Wind Energy Science*, vol. 3, no. 2, pp. 533–543, 2018.

[96] M. de Maré and J. Mann, "On the space-time structure of sheared turbulence," *Boundary-layer meteorology*, vol. 160, no. 3, pp. 453–474, 2016.

[97] M. De Maré and J. Mann, "Validation of the mann spectral tensor for offshore wind conditions at different atmospheric stabilities," in *Journal of Physics: Conference Series*, vol. 524, p. 012106, IOP Publishing, 2014.

[98] A. Chougule, J. Mann, A. Segalini, and E. Dellwik, "Spectral tensor parameters for wind turbine load modeling from forested and agricultural landscapes," *Wind Energy*, vol. 18, no. 3, pp. 469–481, 2015.

[99] S. B. Pope, "Turbulent flows," *Measurement Science and Technology*, vol. 12, no. 11, pp. 2020–2021, 2001.

[100] H. Tennekes and J. L. Lumley, *A first course in turbulence*. MIT press, 1972.

[101] H. Ueda and J. O. Hinze, "Fine-structure turbulence in the wall region of a turbulent boundary layer," *Journal of Fluid Mechanics*, vol. 67, no. 1, pp. 125–143, 1975.

[102] P. A. Davidson, *Turbulence: an introduction for scientists and engineers*. Oxford university press, 2015.

[103] U. Frisch, *Turbulence: the legacy of AN Kolmogorov*. Cambridge university press, 1995.

[104] N. Dimitrov and A. Natarajan, "Application of simulated lidar scanning patterns to constrained gaussian turbulence fields for load validation," *Wind Energy*, vol. 20, no. 1, pp. 79–95, 2017.

[105] S. Caires, J.-J. Schouten, L. Lønseth, V. Neshaug, I. Pathirana, and O. Storas, "Uncertainties in offshore wind turbulence intensity," in *Journal of Physics: Conference Series*, vol. 1356, p. 012037, IOP Publishing, 2019.

[106] S. L. Ellison and A. Williams, "Quantifying uncertainty in analytical measurement," 2012.

[107] H. W. Coleman and W. G. Steele, *Experimentation, validation, and uncertainty analysis for engineers*. John Wiley & Sons, 2018.

[108] B. Gribben, M. Courtney, J. Gottschall, and J. Hughes, "A methodology review of uncertainty estimation in wind resource and power performance assessments when using lidars," 2018.

[109] D. H. Lenschow, V. Wulfmeyer, and C. Senff, "Measuring second-through fourth-order moments in noisy data," *Journal of Atmospheric and Oceanic technology*, vol. 17, no. 10, pp. 1330–1347, 2000.

[110] W. S. Chang, *Principles of lasers and optics*. Cambridge University Press, 2005.

[111] S. Raach, D. Schlipf, F. Haizmann, and P. W. Cheng, "Three dimensional dynamic model based wind field reconstruction from lidar data," in *Journal of Physics: Conference Series*, vol. 524, p. 012005, IOP Publishing, 2014.

[112] T. Klaas-Witt and S. Emeis, "The five main influencing factors for lidar errors in complex terrain," *Wind Energy Science*, vol. 7, no. 1, pp. 413–431, 2022.

[113] E. Simley, L. Pao, N. Kelley, B. Jonkman, and R. Frehlich, "Lidar wind speed measurements of evolving wind fields," in *50th AIAA aerospace sciences meeting including the new horizons forum and aerospace exposition*, p. 656, 2012.

[114] J. Newman, "Optimizing lidar scanning strategies for wind energy turbulence measurements," 2015.

[115] M. Hofsäß, A. Clifton, and P. W. Cheng, "Reducing the uncertainty of lidar measurements in complex terrain using a linear model approach," *Remote Sensing*, vol. 10, no. 9, p. 1465, 2018.

[116] A. Clifton and R. Wagner, "Accounting for the effect of turbulence on wind turbine power curves," in *Journal of Physics: Conference Series*, vol. 524, p. 012109, IOP Publishing, 2014.

[117] E. Hedevang, "Wind turbine power curves incorporating turbulence intensity," *Wind Energy*, vol. 17, no. 2, pp. 173–195, 2014.

[118] I. Cohen, Y. Huang, J. Chen, J. Benesty, J. Benesty, J. Chen, Y. Huang, and I. Cohen, "Pearson correlation coefficient," *Noise reduction in speech processing*, pp. 1–4, 2009.

[119] J. H. Zar, "Significance testing of the spearman rank correlation coefficient," *Journal of the American Statistical Association*, vol. 67, no. 339, pp. 578–580, 1972.

[120] C. Bunce, "Correlation, agreement, and bland–altman analysis: statistical analysis of method comparison studies," *American journal of ophthalmology*, vol. 148, no. 1, pp. 4–6, 2009.

[121] A. Saltelli, "Sensitivity analysis for importance assessment," *Risk analysis*, vol. 22, no. 3, pp. 579–590, 2002.

[122] C. Z. Mooney, *Monte carlo simulation*. No. 116, Sage, 1997.

[123] F. D. Davis *et al.*, "Technology acceptance model: Tam," *Al-Suqri, MN, Al-Aufi, AS: Information Seeking Behavior and Technology Adoption*, vol. 205, p. 219, 1989.

[124] V. Venkatesh and F. D. Davis, "A theoretical extension of the technology acceptance model: Four longitudinal field studies," *Management Science*, vol. 46, no. 2, pp. 186–204, 2000.

[125] G. C. Moore and I. Benbasat, "Development of an instrument to measure the perceptions of adopting an information technology innovation," *Information systems research*, vol. 2, no. 3, pp. 192–222, 1991.

[126] R. Wagner, T. F. Pedersen, M. Courtney, I. Antoniou, S. Davoust, and R. Rivera, "Power curve measurement with a nacelle mounted lidar," *Wind Energy*, vol. 17, no. 9, pp. 1441–1453, 2014.

[127] "L2 norm." `https://mathworld.wolfram.com/L2-Norm.html`. Accessed: 2024-02-18.

[128] J. L. Myers, A. D. Well, and R. F. Lorch Jr, *Research design and statistical analysis*. Routledge, 2013.

[129] T. W. MacFarland and J. M. Yates, *Spearman's Rank-Difference Coefficient of Correlation*, pp. 249–297. Cham: Springer International Publishing, 2016.

[130] I. E. Commission *et al.*, "Wind turbines-part 1: design requirements," *IEC61400-1*, 2005.

Appendix A

Analysis

A.1 Interpolation

Figure A.1 and Figure A.2 show the effect of interpolating the lidar data.Since the heights at which the lidar and the meteorological mast measure are different, interpolation can be a helpful tool to reduce uncertainties in measurements. As can be seen, the met mast only measures between the height of 58 meters and 123 meters, whereas the lidar has a larger range of heights. Interpolation allows for the estimation of wind speed and TI at heights where direct measurements are unavailable, thus providing a more continuous and comprehensive profile of these parameters.

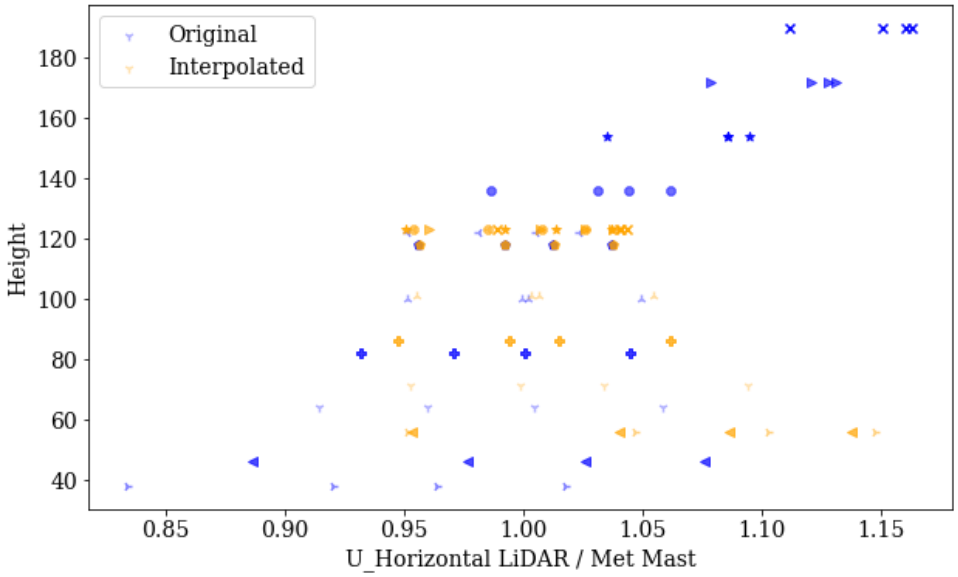

Figure A.1: Interpolated vs uninterpolated wind speed for different heights

As evident in Figure A.1, the lidar tends to overpredict wind speed at higher altitudes, leading to an underprediction of TI, as can be seen in Figure A.2. This discrepancy underscores the need for careful interpolation and cross-validation between different measurement devices. The comparison between different heights also reveals that wind profiles are not linear, since wind speed generally increases with height due to the decreasing influence of surface friction. Consequently, measurements taken at different heights need to be adjusted to a common reference level for accurate comparison.

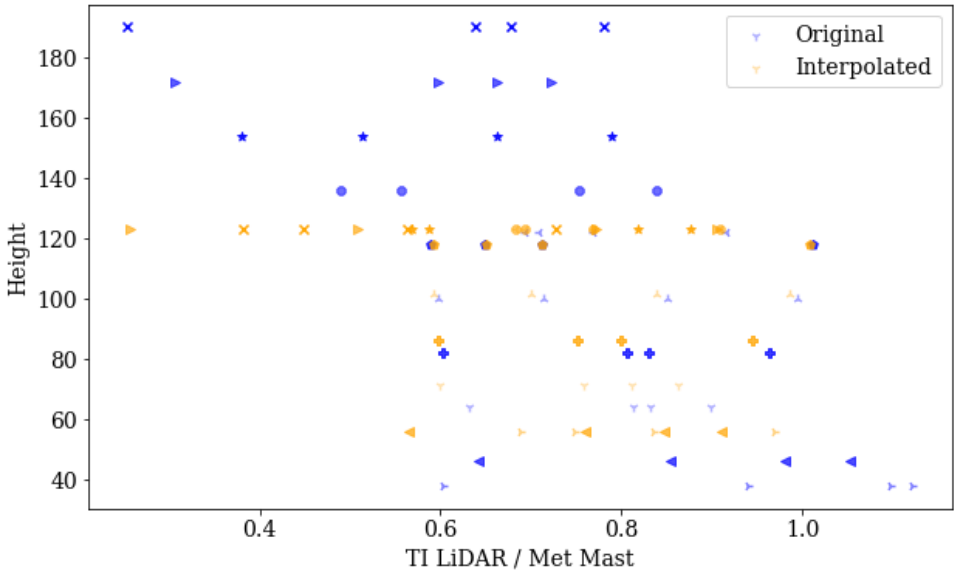

Figure A.2: Interpolated vs uninterpolated TI for different heights

A.2 Euclidian norm

This section proves that the Euclidian or l_2 norm of the horizontal components of wind speed is a convex function. In favor of proving this statement, the Euclidian norm and the convex function have to be explained. The l_2 norm is a vector norm defined for a complex vector [127], and can be seen in Equation A.1. Next to that, a function f is convex if for any two points x and y and any $\lambda \in [0, 1]$, the inequality given in Equation A.2 holds. This can be tested in a Python file with the data from the wind site. This results in Figure A.3, which shows that indeed the l_2 norm of the horizontal wind components is a convex function.

$$l_2 = \sqrt{u^2 + v^2} \tag{A.1}$$

$$f\left(\lambda x + (1-\lambda)\, y\right) \leq \lambda f(x) + (1-\lambda) f(y) \tag{A.2}$$

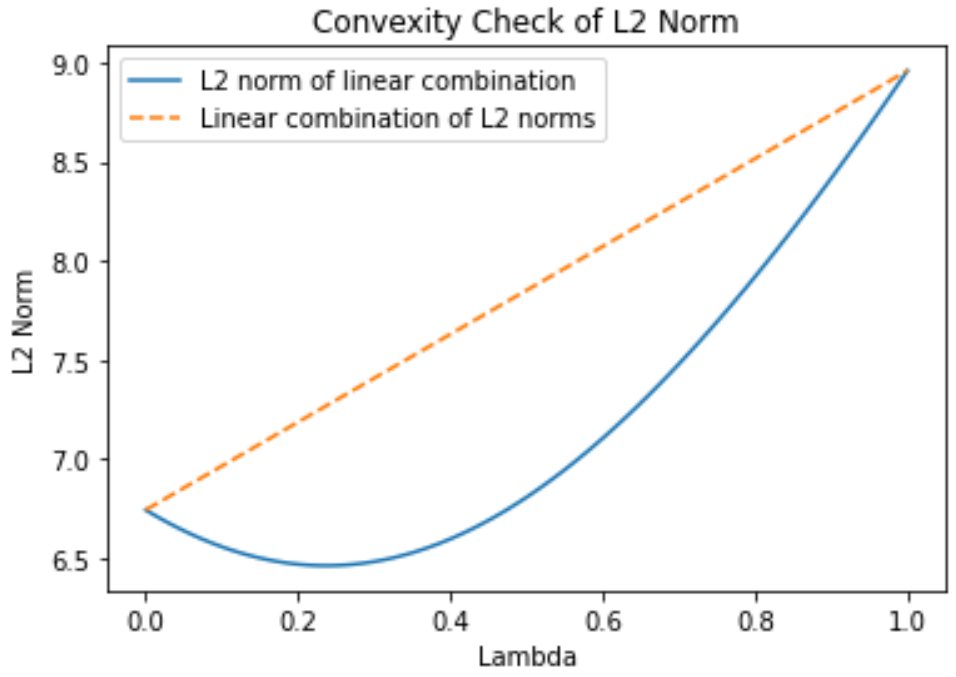

Figure A.3: Check for convexity of Euclidian norm of horizontal wind components

A.3 Roughness analysis

In Figure 5.9 and Figure 5.11, it was evident that the lidar had extra underprediction at a wind speed of 8 m/s. To investigate if this is due to roughness, a roughness analysis can be conducted. Since this occurs at a wind speed of 8 m/s and the measurements are taken for 10-minute intervals, it's important to examine what lies to the S-SW side of the site at a distance of 4800 meters. This distance is derived by multiplying the wind speed (8 m/s) with the time (10 minutes), resulting in a distance of 4.8 kilometers, as shown in Equation A.3.

$$R_{8m/s} = 8 * 10 * 60 = 4800m = 4.8km \tag{A.3}$$

WindPRO can be used to perform a roughness analysis for the surrounding area, focusing on the 5-kilometer radius around the site. This involves creating a 5-kilometer ring around the lidar location and conducting a roughness analysis in Figure A.4a and a height contour analysis in Figure A.4b. Observing Figure A.4a, it's apparent that the terrain in the 5-kilometer radius does not change in terms of roughness, indicating that roughness may not explain the lidar underprediction. Looking at the roughness map, it is more likely that the West and North-East directions result in changes in turbulence intensity due to the wind arriving from the water. Another reason for the lidar underprediction could be the presence of existing turbines in the park. In Figure A.4a, it should be noted that the three westmost turbines were already at the site when the measurements were taken. Since the meteorological mast was positioned 300 meters to the south of the lidar, as shown in Figure F.6, it could have experienced more wake effects from the existing turbines, possibly overestimating the turbulence in the air.

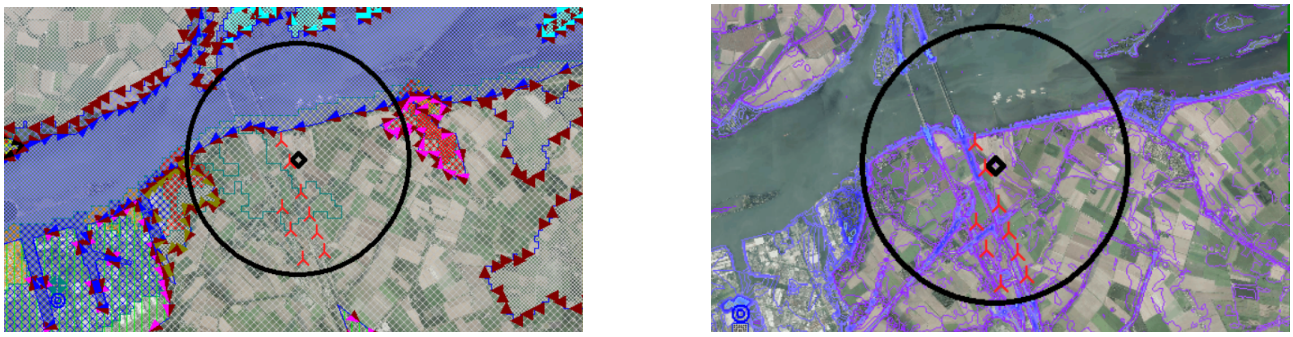

(a) Roughness analysis

(b) Height contour lines

Figure A.4: Comparison of roughness analysis and height contour lines

It is interesting to take a look at what would happen if the S-SW direction is excluded from the dataset. When comparing Figure A.5 with Figure 5.8, it can be seen that both the lidar and its corrections perform a lot better when compared with the meteorological mast at a wind speed of $8m/s$. It is also interesting to note that the perturbation adjustment performs a lot better at lower wind speeds, but worse at higher wind speeds, which is probably due to lesser measurements, since the S-SW wind direction was the prominent wind direction at this site.

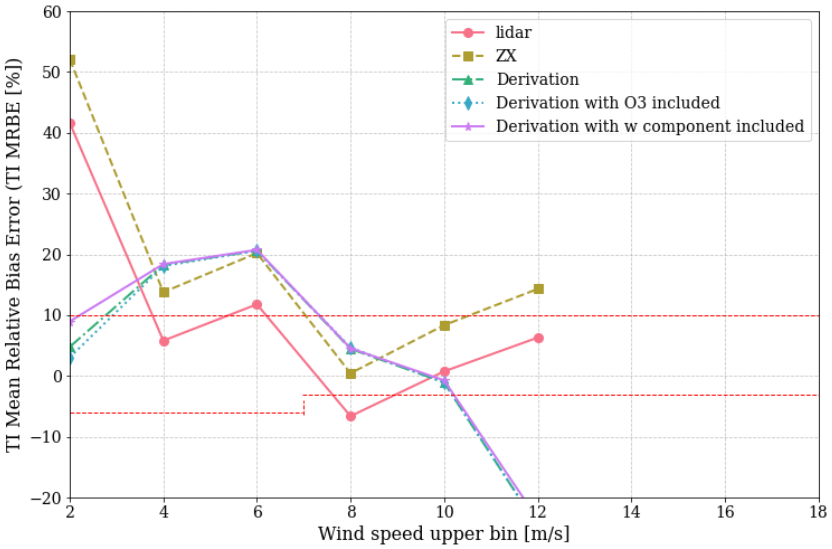

Figure A.5: MRBE at 82m with S-SW direction excluded

Appendix B

Basic equations

B.1 Reynolds conditions

These Reynolds conditions have been taken from the book by Sumer and Fuhrman [27].

$$\overline{f+g} = \overline{f} + \overline{g} \tag{B.1}$$

$$\overline{af} = a\overline{f} \tag{B.2}$$

$$\overline{a} = a \tag{B.3}$$

$$\overline{\frac{\partial f}{\partial s}} = \frac{\partial \overline{f}}{\partial s} \tag{B.4}$$

$$\overline{\overline{f}g} = \overline{f}\,\overline{g} \tag{B.5}$$

$$\overline{\overline{f}} = \overline{f} \tag{B.6}$$

$$\overline{f'} = 0 \tag{B.7}$$

$$\overline{\overline{f}\overline{g}} = \overline{f}\,\overline{g} \tag{B.8}$$

$$\overline{\overline{f}g'} = 0 \tag{B.9}$$

in which a = constant, and $s = x_1, x_2, x_3, t$

B.2 TI derivatives

For the new formula:

$$TI = \sqrt{\frac{\overline{u'^2} \cdot \overline{\cos^2(\theta)} + \mathrm{Cov}(u'^2, \cos^2(\theta))}{U^2_{\mathrm{mean}}} + \frac{\overline{v'^2} \cdot \overline{\cos^2(\theta)} + \mathrm{Cov}(v'^2, \cos^2(\theta))}{U^2_{\mathrm{mean}}}} \tag{B.10}$$

The variables are $\overline{u'^2}$, $\overline{v'^2}$, $\overline{\cos^2(\theta)}$, $\mathrm{Cov}(u'^2, \cos^2(\theta))$, $\mathrm{Cov}(v'^2, \cos^2(\theta))$, and U_{mean}.

Due to the complexity of the formula, we can break it into parts.

$$A = \frac{\overline{u'^2} \cdot \overline{\cos^2(\theta)} + \mathrm{Cov}(u'^2, \cos^2(\theta))}{U^2_{\mathrm{mean}}}, \quad B = \frac{\overline{v'^2} \cdot \overline{\cos^2(\theta)} + \mathrm{Cov}(v'^2, \cos^2(\theta))}{U^2_{\mathrm{mean}}} \tag{B.11}$$

$$TI = \sqrt{A + B} \tag{B.12}$$

The partial derivatives are more complicated and involve chain rules. Each partial derivative of A and B with respect to their variables must be computed first, followed by the derivative of the square root function.

Let's denote $R = A + B$ for simplicity. The partial derivatives of R are:

$$\frac{\partial R}{\partial \overline{u'^2}} = \frac{\overline{\cos^2(\theta)}}{U_{\text{mean}}^2}, \quad \frac{\partial R}{\partial \overline{v'^2}} = \frac{\overline{\cos^2(\theta)}}{U_{\text{mean}}^2} \tag{B.13}$$

$$\frac{\partial R}{\partial \overline{\cos^2(\theta)}} = \frac{\overline{u'^2} + \overline{v'^2}}{U_{\text{mean}}^2}, \quad \frac{\partial R}{\partial \text{Cov}(u'^2, \cos^2(\theta))} = \frac{1}{U_{\text{mean}}^2}, \quad \frac{\partial R}{\partial \text{Cov}(v'^2, \cos^2(\theta))} = \frac{1}{U_{\text{mean}}^2} \tag{B.14}$$

$$\frac{\partial R}{\partial U_{\text{mean}}} = -2\frac{\overline{u'^2} \cdot \overline{\cos^2(\theta)} + \text{Cov}(u'^2, \cos^2(\theta)) + \overline{v'^2} \cdot \overline{\cos^2(\theta)} + \text{Cov}(v'^2, \cos^2(\theta))}{U_{\text{mean}}^3} \tag{B.15}$$

Then the uncertainty δR is:

$$\delta R = , \sqrt{\begin{array}{l}\left(\frac{\partial R}{\partial \overline{u'^2}}\delta\overline{u'^2}\right)^2 + \left(\frac{\partial R}{\partial \overline{v'^2}}\delta\overline{v'^2}\right)^2 + \left(\frac{\partial R}{\partial \overline{\cos^2(\theta)}}\delta\overline{\cos^2(\theta)}\right)^2 + \left(\frac{\partial R}{\partial \text{Cov}(u'^2, \cos^2(\theta))}\delta\text{Cov}(u'^2, \cos^2(\theta))\right)^2 \\ + \left(\frac{\partial R}{\partial \text{Cov}(v'^2, \cos^2(\theta))}\delta\text{Cov}(v'^2, \cos^2(\theta))\right)^2 + \left(\frac{\partial R}{\partial U_{\text{mean}}}\delta U_{\text{mean}}\right)^2 + \textit{(cross terms with correlations)}\end{array}} \tag{B.16}$$

B.3 Diameter of lidar ring

As can be seen in the schematic of the continuous wave lidar in Figure 1.1a, the diameter of the lidar ring can be derived with two parameters: the height z and the lidar opening angle ϕ. For this example, a measuring height of 100 meters is chosen, and the ϕ is taken to be 30 degrees.

$$D_{Lring} = 2 * (z * tan(\phi)) \tag{B.17}$$

$$D_{Lring} = 2 * (100 * tan(30°)) \tag{B.18}$$

$$D_{Lring} = 115.47m \tag{B.19}$$

B.4 Lidar/cup TI ratio

$$means = \frac{TI_{lidar} + TI_{cup}}{2} \tag{B.20}$$

$$differences = TI_{lidar} - TI_{cup} \tag{B.21}$$

$$Lidar/CupRatio = \frac{differences}{means} \tag{B.22}$$

B.5 Pearson correlation coefficient

According to Cohen *et al* [118], the Pearson correlation coefficient is defined as:

$$\rho(a, b) = \frac{E(ab)}{\sigma_a \sigma_b} \tag{B.23}$$

where $E(ab)$ is the cross-correlation between a and b, whereas σ_a and σ_b are the standard deviations of a and b. If the Pearson correlation coefficient is squared it will indicate the linear relationship between a and b. The closer ρ^2 comes to the value of 1, the stronger the correlation between a and b. The authors also mention that a and b are uncorrelated when ρ^2 is equal to zero.

B.6 Spearman rank correlation

As said by Zar [119], the Spearman rank correlation coefficient is given by:

$$r_s = 1 - \frac{6 \sum d_i^2}{n(n^2 - 1)} \tag{B.24}$$

where n is the number of observations and d_i is the difference between the two ranks of each observation. The Spearmann correlation coefficient equals the Pearson correlation coefficient of two rank variables, as said by Myers *et al* [128]. This method compares the ordered ranks of the variables to determine if there is an association or correlation between them, as mentioned by MacFarland and Yates [129]. They mention that it should be remembered that correlation does not imply causation, so even if there is a strong association between two variables, it does not necessarily mean that one variable causes another. This caution is essential for all measures of association or correlation.

Appendix C

Code flowcharts

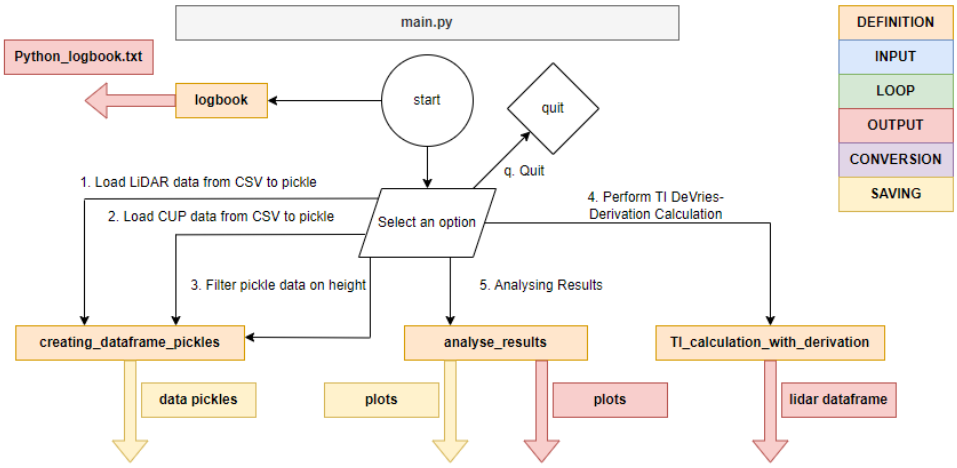

Figure C.1: Flowchart main.py

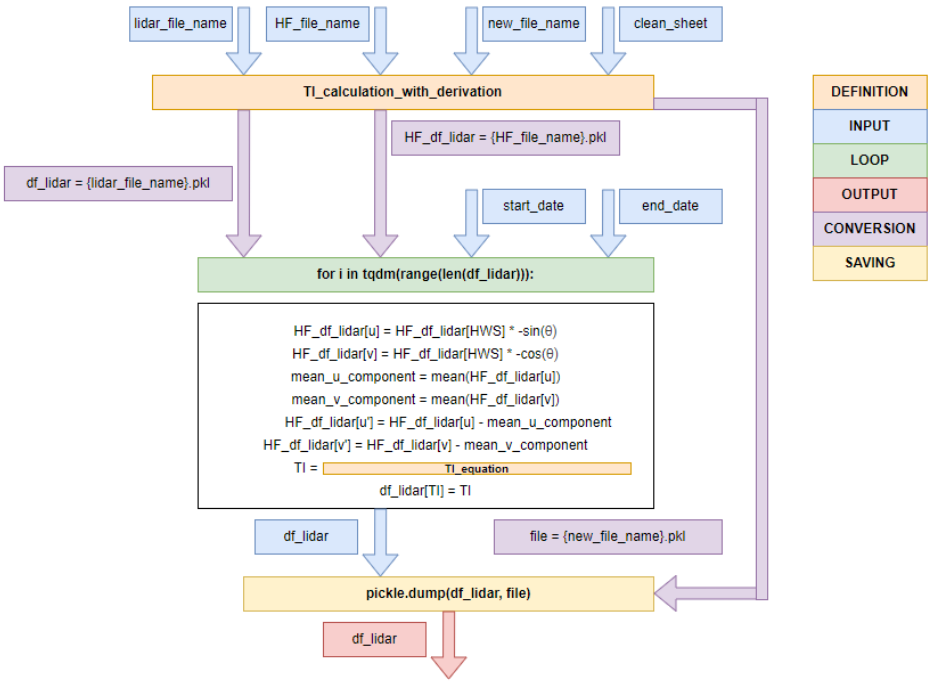

Figure C.2: Flowchart TI calculation with derivation

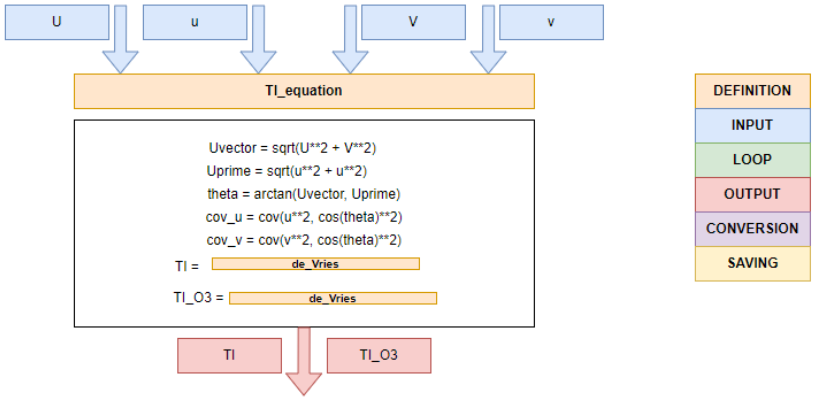

Figure C.3: Flowchart TI equation

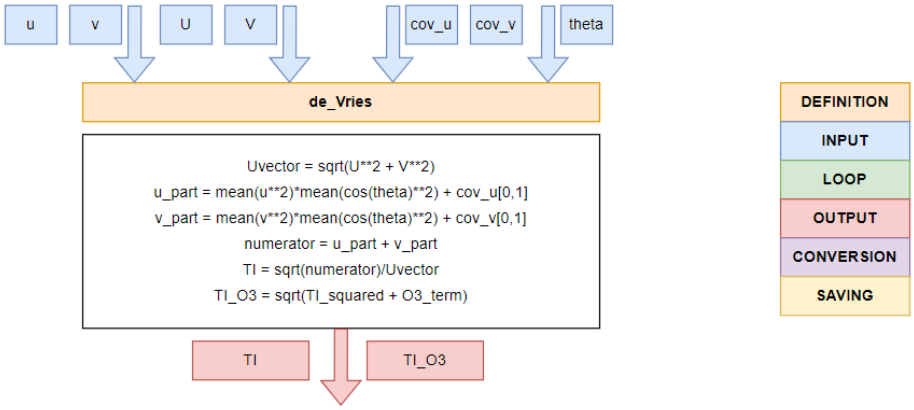

Figure C.4: Flowchart De Vries Calculation

Appendix D

Derivation verification

D.1 Mean wind speed derivation

The following derivation is the work of A. Black [28] [86], however due to it's significance to the project, it has been decided to lay out here as well.

Your U_{scalar} consists of a U and V component.

$$U_{scalar,1Hz} = \sqrt{\mathbf{u}^2 + \mathbf{v}^2} \tag{D.1}$$

We can now use Reynolds decomposition (section 4.1):

$$U_{scalar,1Hz} = \sqrt{\overline{u}^2 + 2\overline{u}u' + u'^2 + \overline{v}^2 + 2\overline{v}v' + v'^2} \tag{D.2}$$

It is then possible to factor out vector average:

$$U_{scalar,1Hz} = \sqrt{\overline{u}^2 + \overline{v}^2}\sqrt{1 + \frac{1}{\overline{u}^2 + \overline{v}^2}\left[2\overline{u}u' + u'^2 + 2\overline{v}v' + v'^2\right]} \tag{D.3}$$

We know that $U_{vector} = \sqrt{\overline{u}^2 + \overline{v}^2}$:

$$U_{scalar,1Hz} = U_{vector}\sqrt{1 + \frac{1}{U^2_{vector}}\left[2\overline{u}u' + u'^2 + 2\overline{v}v' + v'^2\right]} \tag{D.4}$$

We can now use binomial approximation (section 4.1), but keep in mind that we are dropping the $O(3)$ terms (*Note: this is for the mean wind speed case, this might be different in the TI case*):

$$U_{scalar,1Hz} = U_{vector}\left[1 + \frac{1}{2U^2_{vector}}\left(2\overline{u}u' + u'^2 + 2\overline{v}v' + v'^2\right) - \frac{1}{8U^4_{vector}}\left(4\overline{u}^2u'^2 + 4\overline{v}^2v'^2 + 8\overline{u}u'\overline{v}v'\right)\right] \tag{D.5}$$

This formula is limited in application, due to the error term needing to be small and since it likely is not applicable for low speeds with high turbulence. From this point in the formula, we can apply time averaging (explained in section 4.1), which drops the linear terms (using the fact that $\overline{\overline{u}u'} = \overline{u} \cdot \overline{u'} = \overline{u} \cdot 0 = 0$ and $\overline{\overline{v}v'} = \overline{v} \cdot \overline{v'} = \overline{v} \cdot 0 = 0$):

$$U_{scalar,1Hz} = \overline{U_{vector}}\overline{\left[1 + \frac{1}{2U^2_{vector}}\left(2\overline{u}u' + u'^2 + 2\overline{v}v' + v'^2\right) - \frac{1}{8U^4_{vector}}\left(4\overline{u}^2u'^2 + 4\overline{v}^2v'^2 + 8\overline{u}u'\overline{v}v'\right)\right]} \tag{D.6}$$

$$U_{scalar} = U_{vector}\overline{\left[1 + \frac{1}{2U^2_{vector}}\left[u'^2 + v'^2\right] - \frac{1}{2U^4_{vector}}\left[\overline{u}^2u'^2 + \overline{v}^2v'^2 + 2\overline{u}u'\overline{v}v'\right]\right]} \tag{D.7}$$

Since we know that $U_{vector} = \sqrt{\overline{u}^2 + \overline{v}^2}$ and $\overrightarrow{U_{vector}} \cdot \overrightarrow{U'} = \overline{u}u' + \overline{v}v'$, we can re-express the formula as square of dot product of mean and turbulent terms.

$$U_{scalar} = U_{vector}\overline{\left[1 + \frac{1}{2U^2_{vector}}\left[u'^2 + v'^2\right] - \frac{1}{2U^4_{vector}}\left[U_{vector} \cdot \overrightarrow{U'}\right]^2\right]} \tag{D.8}$$

We can simplify this equation, knowing that: $\left[U_{vector} \cdot \overrightarrow{U'}\right]^2 = U_{vector}^2 \left[u'^2 + v'^2\right] cos^2(\theta)$, with θ being the angle between U_{vector} and $\overrightarrow{U'}$.

$$U_{scalar} = U_{vector} \overline{\left[1 + \frac{1}{2U_{vector}^2} \left[u'^2 + v'^2\right] - \frac{1}{2U_{vector}^2} \left[u'^2 + v'^2\right] cos^2(\theta)\right]} \tag{D.9}$$

$$U_{scalar} = U_{vector} \overline{\left[1 + \frac{1}{2U_{vector}^2} \left[u'^2 + v'^2\right] (1 - cos^2(\theta))\right]} \tag{D.10}$$

Simple trigonometry ($sin^2 + cos^2 = 1$) and the fact that $\overline{1 + \frac{1}{2U_{vector}^2}} = 1 + \frac{1}{2U_{vector}^2}$ leads to the following expressions:

$$U_{scalar} = U_{vector} \left[1 + \frac{1}{2U_{vector}^2} \overline{\left[u'^2 + v'^2\right] sin^2\theta}\right] \tag{D.11}$$

$$U_{scalar} = U_{vector} + \frac{1}{2U_{vector}} \overline{\left|\left|\overrightarrow{U'}\right|\right|_2^2 sin^2\theta} \tag{D.12}$$

D.2 TI derivation

Equation D.13 can be found in literature [13] [19] [130].

$$TI = \frac{\sigma_U}{U_{mean}} \tag{D.13}$$

Equation D.14 can be found in literature [82].

$$Var = \sigma_U^2 = \overline{U_{scalar}^2} - \overline{U_{scalar}}^2 \tag{D.14}$$

Equation D.15 can be taken from Black's perturbation method in [28].

$$U_{mean} = \sqrt{\overline{u}^2 + \overline{v}^2} \tag{D.15}$$

giving:

$$TI = \frac{\sqrt{\overline{U_{scalar}^2} - \overline{U_{scalar}}^2}}{U_{mean}} \tag{D.16}$$

Equation D.17 can be taken from Black [28], as said in section 4.1.

$$U_{scalar} = U_{mean} \left[1 + \frac{1}{2U_{mean}^2} \left[2\overline{u}u' + u'^2 + 2\overline{v}v' + v'^2\right] - \frac{1}{8U_{mean}^4} \left[4\overline{u}^2u'^2 + 4\overline{v}^2v'^2 + 8\overline{u}u'\overline{v}v'\right]\right] \tag{D.17}$$

We need the squared form of this for TI, giving the following derivation:

$$U_{scalar} = U_{mean} + \frac{1}{2U_{mean}} \left[2\overline{u}u' + u'^2 + 2\overline{v}v' + v'^2\right] - \frac{1}{2U_{mean}^3} \left[\overline{u}^2u'^2 + \overline{v}^2v'^2 + 2\overline{u}u'\overline{v}v'\right] \tag{D.18}$$

$$U_{scalar}^2 = \left(U_{mean} + \frac{1}{2U_{mean}} \left[2\overline{u}u' + u'^2 + 2\overline{v}v' + v'^2\right] - \frac{1}{2U_{mean}^3} \left[\overline{u}^2u'^2 + \overline{v}^2v'^2 + 2\overline{u}u'\overline{v}v'\right]\right)^2 \tag{D.19}$$

Equation D.20 has been tested in a virtual environment, and showed a 0% difference with the squared answer of Equation D.17.

$$\begin{aligned} U_{scalar}^2 = U_{mean}^2 &+ \left[2\overline{u}u' + u'^2 + 2\overline{v}v' + v'^2\right] - \frac{1}{U_{mean}^2} \left[\overline{u}^2u'^2 + \overline{v}^2v'^2 + 2\overline{u}u'\overline{v}v'\right] + \left(\frac{2\overline{u}u' + u'^2 + 2\overline{v}v' + v'^2}{2U_{mean}}\right)^2 \\ &+ \left(\frac{\overline{u}^2u'^2 + \overline{v}^2v'^2 + 2\overline{u}u'\overline{v}v'}{2U_{mean}^3}\right)^2 - \frac{1}{2U_{mean}^4} \left[2\overline{u}u' + u'^2 + 2\overline{v}v' + v'^2\right] \left[\overline{u}^2u'^2 + \overline{v}^2v'^2 + 2\overline{u}u'\overline{v}v'\right] \end{aligned} \tag{D.20}$$

Expanding:

$$
\begin{aligned}
U_{scalar}^2 = & U_{mean}^2 + \left[2\overline{u}u' + u'^2 + 2\overline{v}v' + v'^2\right] \\
& - \frac{1}{U_{mean}^2}\left[\overline{u}^2u'^2 + \overline{v}^2v'^2 + 2\overline{u}u'\overline{v}v'\right] \\
& + \frac{1}{4U_{mean}^2}\left[4\overline{u}^2u'^2 + 4\overline{u}u'^3 + 4\overline{v}^2v'^2 + 8\overline{u}u'\overline{v}v' + 4\overline{u}u'v'^2 + 4u'^2\overline{v}v' + 4\overline{v}v'^3 + u'^4 + v'^4 + 2u'^2v'^2\right] \\
& + \frac{1}{4U_{mean}^6}\left[\overline{u}^4u'^4 + \overline{v}^4v'^4 + 6\overline{u}^2u'^2\overline{v}^2v'^2 + 4\overline{u}u'\overline{v}^3v'^3 + 4\overline{u}^3u'^3\overline{v}v'\right] \\
& - \frac{1}{2U_{mean}^4}\left[2\overline{u}^3u'^3 + 2\overline{v}^3v'^3 + 6\overline{u}^2u'^2\overline{v}v' + 6\overline{u}u'\overline{v}^2v'^2 + \overline{u}^2u'^4 + \overline{v}^2v'^4 + \overline{u}^2u'^2v'^2 + u'^2\overline{v}^2v'^2 + 2\overline{u}u'^3\overline{v}v' + 2\overline{u}u'\overline{v}v'^3\right]
\end{aligned}
\tag{D.21}
$$

Simplifying Equation D.21 leads to Equation D.22, which has been tested in a virtual environment, and showed a 0% difference with the answer of Equation D.20:

$$
\begin{aligned}
U_{scalar}^2 = & U_{mean}^2 + \left[2\overline{u}u' + u'^2 + 2\overline{v}v' + v'^2\right] \\
& + \frac{1}{4U_{mean}^2}\left[4\overline{u}u'^3 + 4\overline{u}u'v'^2 + 4u'^2\overline{v}v' + 4\overline{v}v'^3 + u'^4 + v'^4 + 2u'^2v'^2\right] \\
& + \frac{1}{4U_{mean}^6}\left[\overline{u}^4u'^4 + \overline{v}^4v'^4 + 6\overline{u}^2u'^2\overline{v}^2v'^2 + 4\overline{u}u'\overline{v}^3v'^3 + 4\overline{u}^3u'^3\overline{v}v'\right] \\
& - \frac{1}{2U_{mean}^4}\left[2\overline{u}^3u'^3 + 2\overline{v}^3v'^3 + 6\overline{u}^2u'^2\overline{v}v' + 6\overline{u}u'\overline{v}^2v'^2 + \overline{u}^2u'^4 + \overline{v}^2v'^4 + \overline{u}^2u'^2v'^2 + u'^2\overline{v}^2v'^2 + 2\overline{u}u'^3\overline{v}v' + 2\overline{u}u'\overline{v}v'^3\right]
\end{aligned}
\tag{D.22}
$$

We will now disregard the fourth-order components and install a constant $O(4)$:

$$
\begin{aligned}
U_{scalar}^2 = & U_{mean}^2 + \left[2\overline{u}u' + u'^2 + 2\overline{v}v' + v'^2\right] \\
& + \frac{1}{U_{mean}^2}\left[\overline{u}u'^3 + \overline{u}u'v'^2 + u'^2\overline{v}v' + \overline{v}v'^3\right] \\
& - \frac{1}{U_{mean}^4}\left[\overline{u}^3u'^3 + \overline{v}^3v'^3 + 3\overline{u}^2u'^2\overline{v}v' + 3\overline{u}u'\overline{v}^2v'^2\right] + O(4)
\end{aligned}
\tag{D.23}
$$

Now you can apply time averaging on this, using the fact that $\overline{u'} = 0$, $\overline{u'^2} \neq 0$, $\overline{u'^3} \neq 0$, $\overline{u+v} = \overline{u} + \overline{v}$ and $\overline{\overline{u}} = \overline{u}$ (also considering $\overline{\overline{A}BC} = \overline{A} \cdot \overline{BC}$):

$$
\begin{aligned}
\overline{U_{scalar}^2} = & U_{mean}^2 + \overline{\left[2\overline{u}u' + u'^2 + 2\overline{v}v' + v'^2\right]} \\
& + \frac{1}{U_{mean}^2}\overline{\left[\overline{u}u'^3 + \overline{u}u'v'^2 + u'^2\overline{v}v' + \overline{v}v'^3\right]} \\
& - \frac{1}{U_{mean}^4}\overline{\left[\overline{u}^3u'^3 + \overline{v}^3v'^3 + 3\overline{u}^2u'^2\overline{v}v' + 3\overline{u}u'\overline{v}^2v'^2\right]} + O(4)
\end{aligned}
\tag{D.24}
$$

The step from Equation D.24 to Equation D.25 leads to a difference of around 0.65%.

$$
\begin{aligned}
\overline{U_{scalar}^2} = & U_{mean}^2 + \left[\overline{u'^2} + \overline{v'^2}\right] \\
& + \frac{1}{U_{mean}^2}\left[\overline{u}\,\overline{u'^3} + \overline{u}\,\overline{u'v'^2} + \overline{v}\,\overline{u'^2v'} + \overline{v}\,\overline{v'^3}\right] \\
& - \frac{1}{U_{mean}^4}\left[\overline{u}^3\overline{u'^3} + \overline{v}^3\overline{v'^3} + 3\overline{u}^2\overline{v}\,\overline{u'^2v'} + 3\overline{v}^2\overline{u}\,\overline{u'v'^2}\right] + O(4)
\end{aligned}
\tag{D.25}
$$

Now that we have a formula for the first part of the TI equation, we will move on to the next part, using Equation 4.20 as a starting point.

$$
\overline{U_{scalar}} = \overline{U_{mean}\left[1 + \frac{1}{2U_{mean}^2}\left(2\overline{u}u' + u'^2 + 2\overline{v}v' + v'^2\right) - \frac{1}{8U_{mean}^4}\left(4\overline{u}^2u'^2 + 4\overline{v}^2v'^2 + 8\overline{u}u'\overline{v}v'\right)\right]}
\tag{D.26}
$$

Since we know that $\overline{u'} = 0$:

$$\overline{U_{scalar}} = U_{mean} + \frac{1}{2U_{mean}}\left[\overline{u'^2} + \overline{v'^2}\right] - \frac{1}{2U_{mean}^3}\left[\overline{u}^2\overline{u'^2} + \overline{v}^2\overline{v'^2} + \overline{2\overline{u}u'\overline{v}v'}\right] \tag{D.27}$$

Now we need to square this, giving the following:

$$\overline{U_{scalar}}^2 = \left(U_{mean} + \frac{1}{2U_{mean}}\left[\overline{u'^2} + \overline{v'^2}\right] - \frac{1}{2U_{mean}^3}\left[\overline{u}^2\overline{u'^2} + \overline{v}^2\overline{v'^2} + \overline{2\overline{u}u'\overline{v}v'}\right]\right)^2 \tag{D.28}$$

The step from Equation D.28 to Equation D.29 has also been verified in a virtual environment, leading to a difference of 0%.

$$\begin{aligned}\overline{U_{scalar}}^2 = {} & U_{mean}^2 + \left[\overline{u'^2} + \overline{v'^2}\right] - \frac{1}{U_{mean}^2}\left[\overline{u}^2\overline{u'^2} + \overline{v}^2\overline{v'^2} + \overline{2\overline{u}u'\overline{v}v'}\right] \\ & + \frac{1}{4U_{mean}^2}\left[\overline{u'^4} + \overline{v'^4} + 2\overline{u'^2v'^2}\right] \\ & - \frac{1}{2U_{mean}^4}\left[\overline{u}^2\overline{u'^4} + \overline{u'^2}\overline{v}^2\overline{v'^2} + \overline{2\overline{u}u'^3\overline{v}v'} + \right. \\ & \left. \overline{u}^2\overline{u'^2v'^2} + \overline{v}^2\overline{v'^4} + \overline{2\overline{u}u'\overline{v}v'^3}\right] \\ & + \frac{1}{4U_{mean}^6}\left[\overline{u}^4\overline{u'^4} + \overline{v}^4\overline{v'^4} + 6\overline{\overline{u}^2u'^2\overline{v}^2v'^2}\right. \\ & \left. + \overline{4\overline{u}u'\overline{v}^3v'^3} + \overline{4\overline{u}^3u'^3\overline{v}v'}\right]\end{aligned} \tag{D.29}$$

Here as well, we will disregard the fourth-order terms, since it was found that these terms are the same as the fourth-order terms of Equation D.22:

$$\begin{aligned}\overline{U_{scalar}}^2 = {} & U_{mean}^2 + \left[\overline{u'^2} + \overline{v'^2}\right] \\ & - \frac{1}{U_{mean}^2}\left[\overline{u}^2\overline{u'^2} + \overline{v}^2\overline{v'^2} + \overline{2\overline{u}u'\overline{v}v'}\right] + O(4)\end{aligned} \tag{D.30}$$

We can now fill in the equation for TI:

$$TI = \frac{\sqrt{\overline{U_{scalar}^2} - \overline{U_{scalar}}^2}}{U_{mean}} \tag{D.31}$$

$$\begin{aligned}TI_{numerator}^2 = {} & U_{mean}^2 + \left[\overline{u'^2} + \overline{v'^2}\right] \\ & + \frac{1}{U_{mean}^2}\left[\overline{\overline{u}u'^3} + \overline{\overline{u}u'v'^2} + \overline{\overline{v}u'^2v'} + \overline{\overline{v}v'^3}\right] \\ & - \frac{1}{U_{mean}^4}\left[\overline{\overline{u}^3u'^3} + \overline{\overline{v}^3v'^3} + 3\overline{\overline{u}^2\overline{v}u'^2v'} + 3\overline{\overline{v}^2\overline{u}u'v'^2}\right] \\ & - U_{mean}^2 - \left[\overline{u'^2} + \overline{v'^2}\right] \\ & + \frac{1}{U_{mean}^2}\left[\overline{u}^2\overline{u'^2} + \overline{v}^2\overline{v'^2} + \overline{2\overline{u}u'\overline{v}v'}\right] + O(4)\end{aligned} \tag{D.32}$$

$$\begin{aligned}TI_{numerator}^2 = {} & \frac{1}{U_{mean}^2}\left[\overline{\overline{u}u'^3} + \overline{\overline{u}u'v'^2} + \overline{\overline{v}u'^2v'} + \right. \\ & \left. \overline{\overline{v}v'^3} + \overline{u}^2\overline{u'^2} + \overline{v}^2\overline{v'^2} + \overline{2\overline{u}u'\overline{v}v'}\right] \\ & - \frac{1}{U_{mean}^4}\left[\overline{\overline{u}^3u'^3} + \overline{\overline{v}^3v'^3} + 3\overline{\overline{u}^2\overline{v}u'^2v'} + 3\overline{\overline{v}^2\overline{u}u'v'^2}\right] \\ & + O(4)\end{aligned} \tag{D.33}$$

So now we implement this in the equation for TI, where we will also square this function, for easy implementation:

$$TI^2 = \frac{TI^2_{numerator}}{U^2_{mean}} \tag{D.34}$$

$$\begin{aligned} TI^2 = & \frac{1}{U^4_{mean}} \Big[\overline{u}\overline{u'^3} + \overline{u}\overline{u'v'^2} + \overline{v}\overline{u'^2v'} + \overline{v}\overline{v'^3} + \\ & \overline{u}^2\overline{u'^2} + \overline{v}^2\overline{v'^2} + \overline{2\overline{u}u'\overline{v}v'}\Big] - \\ & \frac{1}{U^6_{mean}} \Big[\overline{u}^3\overline{u'^3} + \overline{v}^3\overline{v'^3} + 3\overline{u}^2\overline{v}\overline{u'^2v'} + 3\overline{v}^2\overline{u}\overline{u'v'^2}\Big] \\ & + O(4) \end{aligned} \tag{D.35}$$

If we also drop the O(3)-terms and replace this by a constant $O(3)$, the solution goes to zero:

$$\begin{aligned} TI^2 = & \frac{1}{U^4_{mean}} \Big[\overline{u}^2\overline{u'^2} + \overline{v}^2\overline{v'^2} + 2\overline{\overline{u}u'\overline{v}v'}\Big] \\ & + O(3) + O(4) \end{aligned} \tag{D.36}$$

We can re-express this as square of th dot product of mean and turbulent terms, as done in section 4.1:

$$TI^2 = \frac{1}{U^4_{mean}} \overline{\left[U_{mean} \cdot \overrightarrow{U'}\right]^2} + O(3) + O(4) \tag{D.37}$$

We can simplify this equation, knowing that: $\left[U_{mean} \cdot \overrightarrow{U'}\right]^2 = U^2_{mean}\left[u'^2 + v'^2\right] cos^2(\theta)$, with θ being the angle between U_{vector} and $\overrightarrow{U'}$.

$$TI^2 = \frac{1}{U^2_{mean}} \overline{\left[u'^2 + v'^2\right] cos^2(\theta)} + O(3) + O(4) \tag{D.38}$$

We know that $\overline{u'^2 cos^2} = \overline{u'^2} * \overline{cos^2\theta} + Cov(u'^2, cos^2\theta)$[82]:

$$Cov(X, Y) = E\left[(X - \mu_X)(Y - \mu_Y)\right] \tag{D.39}$$

$$Cov(u'^2, cos^2\theta) = E\left[\left(u'^2 - \overline{u'^2}\right)\left(cos^2\theta - \overline{cos^2\theta}\right)\right] \tag{D.40}$$

This gives the following:

$$\begin{aligned} TI^2 = & \frac{\overline{u'^2} * \overline{cos^2(\theta)} + Cov(u'^2, cos^2\theta)}{U^2_{mean}} + \\ & \frac{\overline{v'^2} * \overline{cos^2(\theta)} + Cov(v'^2, cos^2\theta)}{U^2_{mean}} + O(3) + O(4) \end{aligned} \tag{D.41}$$

Leading to:

$$TI = \sqrt{\frac{\overline{u'^2} * \overline{cos^2(\theta)} + Cov(u'^2, cos^2\theta)}{U^2_{mean}} + \frac{\overline{v'^2} * \overline{cos^2(\theta)} + Cov(v'^2, cos^2\theta)}{U^2_{mean}}} \tag{D.42}$$

D.3 Derivation terms

Term	Description
TI	Defined as the ratio of the mean wind speed (u) to the standard deviation (σ) of wind speed: $I = \frac{\sigma}{u}$
σ_U	Represents the square root of the fluctuation of the wind speed U ($\sqrt{U'^2}$)
U_{mean}	Calculated as the square root of the square of the mean of the different speed components
U_{scaler}	Represents the square root of the square of the different speed components
$\overline{u}$	Mean of the wind speed component u
u'	Fluctuation component of wind speed u
$\overline{v}$	Mean of the wind speed component v
v'	Fluctuation component of wind speed v
θ	Angle between the square root of the square of the mean of the different speed components and the square root of the fluctuation of the different speed components
$Cov(u', cos^2\theta)$	Represents the joint variability between the fluctuation of one wind speed component and the cosine squared of the angle between the wind speed components

Table D.1: Derivation Terms

Appendix E

Existing standards

Standard	Revision	Title
IEC 61400-1	2019	WEGS[1] - Part 1: Design Requirements
IEC 61400-11	2012, A1:2018	Wind turbines, Part 11: Acoustic noise measurement techniques
IEC 61400-12-1	2017	WEGS[1], Part 12-1: Power performance measurements of electricity producing wind turbines
IEC 61400-13	2015-12	Wind turbines, Part 13: Measurement of mechanical loads
IEC CDV 61400-50-2	2020-08	Nacelle mounted lidar for wind measurements
IEC 61400-50-4	-	WEGS[1] - Part 50-4: Use of floating lidars for wind measurements
IEC 61400-15-1	-	WEGS[1] - Part 15-1: Site suitability input conditions for wind power plants
IEC 61400-15-2	-	WEGS[1] - Part 15-2: Energy assessment
IEC 61400-1	2012	2.55

Table E.1: IEC Standards ([1] *Wind Energy Generation Systems*)

IEC 61400-11 requires the measurement of turbulence intensity, but it does not specify which type of sensors should be used. Therefore, lidar measurements can be used.

IEC 61400-12-1 uses cup anemometer measurements for power performance assessment but allows for the use of lidar under certain conditions. Annex L provides guidance and requirements for the use of lidars and sodars for power performance measurements. Using sodars or lidars is conditional upon the use of a cup or sonic sensor on a short meteorological mast on-site. This is limited to flat terrain where site calibration is not required. The meteorological mast should be at least 40 meters tall or the height of the wind turbine's lower blade-tip. Turbulence intensity measurements are often contractually required by turbine OEMs to filter TI outside the conditions of the sales power curve.

IEC 61400-13 requires the measurement of turbulence intensity. Lidar is mentioned in informative Annex D "Recommendations for offshore measurements," which states that lidar can be used if there is no mast available at the offshore test location. Turbulence measurements and certain other parameters must be verified, and data from nearby onshore locations may be used for that purpose. Annex D also allows for an anemometer below hub height to verify the lidar measurements of turbulence intensity. Section 7.2.1 states the direct requirements: "turbulence intensity is defined as if measured through a hub height anemometer (sonic or cup). If other wind speed sensing techniques are used, the derived Tl shall be equivalent to that measured by either a sonic or cup anemometer." Therefore, lidars can be used if they are cup equivalent, or a correction is made, and a verification is provided.

IEC CDV 61400-50-3 is a standard for wind measurements from nacelle-mounted lidars. It is expected to be used primarily for resource assessment but does not specify any particular use case. The IEC 61400-12-1 power performance measurements are mentioned. It requires a sensitivity analysis on several environmental variables (EVs), including TI. According to Section 8.2 of IEC CDV 61400-50-3, "The sensitivity of the accuracy of an intermediate value to an EV can be assessed either by comparison with a reference measurement, through tests in a lab, simulations or theoretical analysis depending on the EV and the intermediate value."

Currently, work is being done to release the IEC 61400-50-4 for floating lidars and the IEC 61400-15 series standards, 61400-15-1 to cover site suitability and 61400-15-2 to cover energy assessment.

Appendix F

Figures

F.1 Project planning

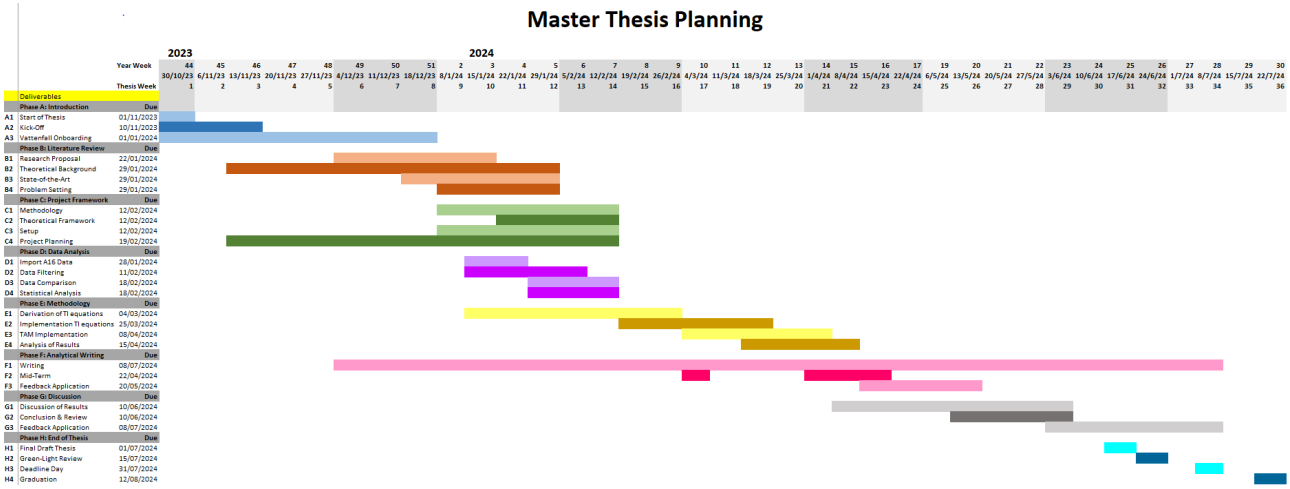

Figure F.1: Master Thesis Planning

F.2 Machine learning

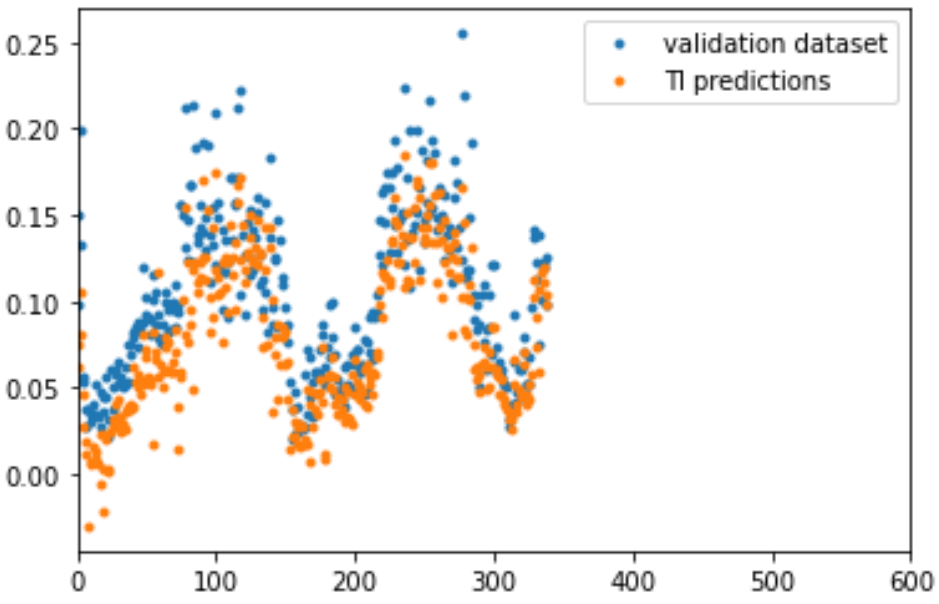

Figure F.2: LSTM Predictions

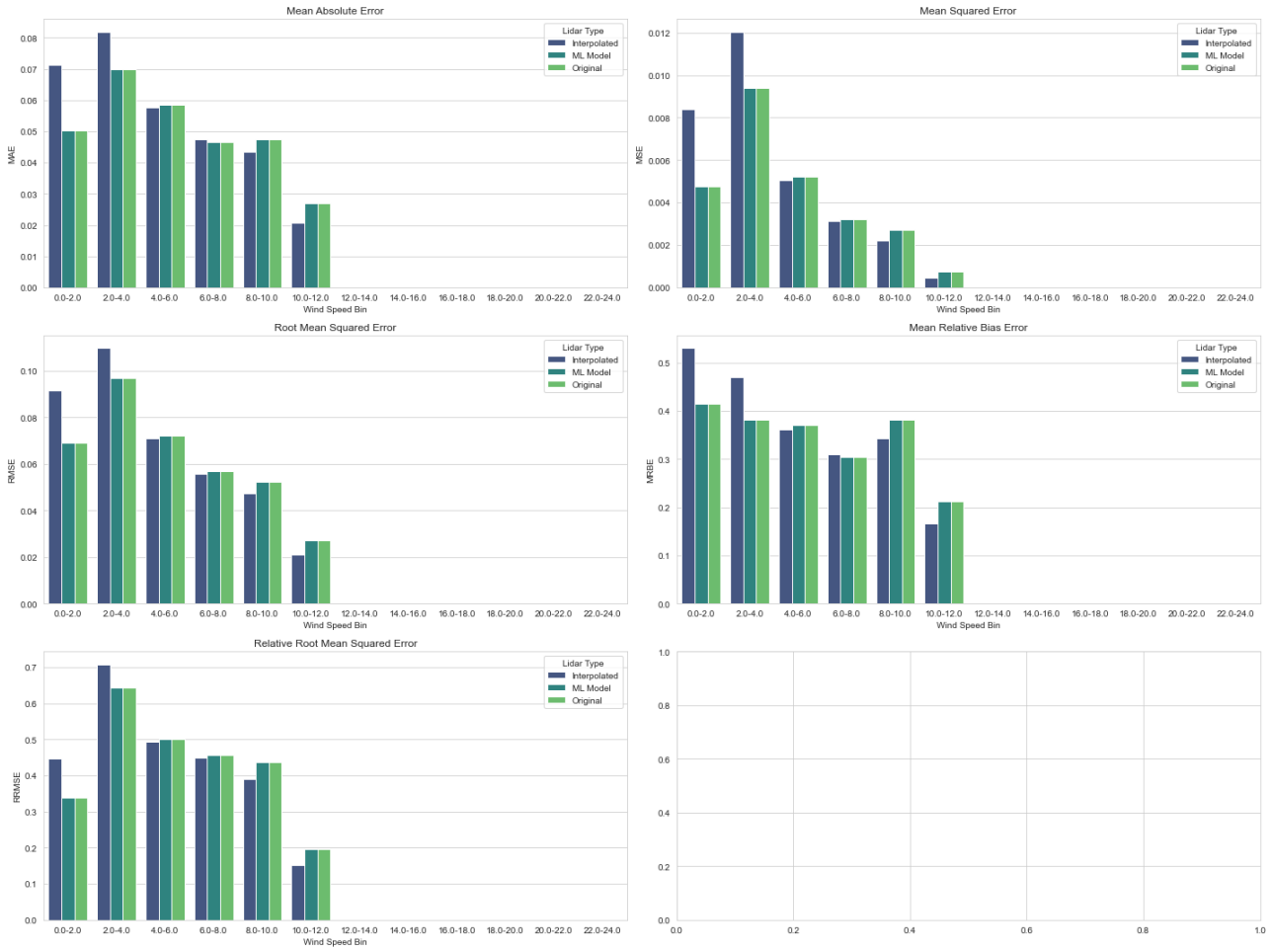

Figure F.3: Data error metrics

F.3 Mast installation report

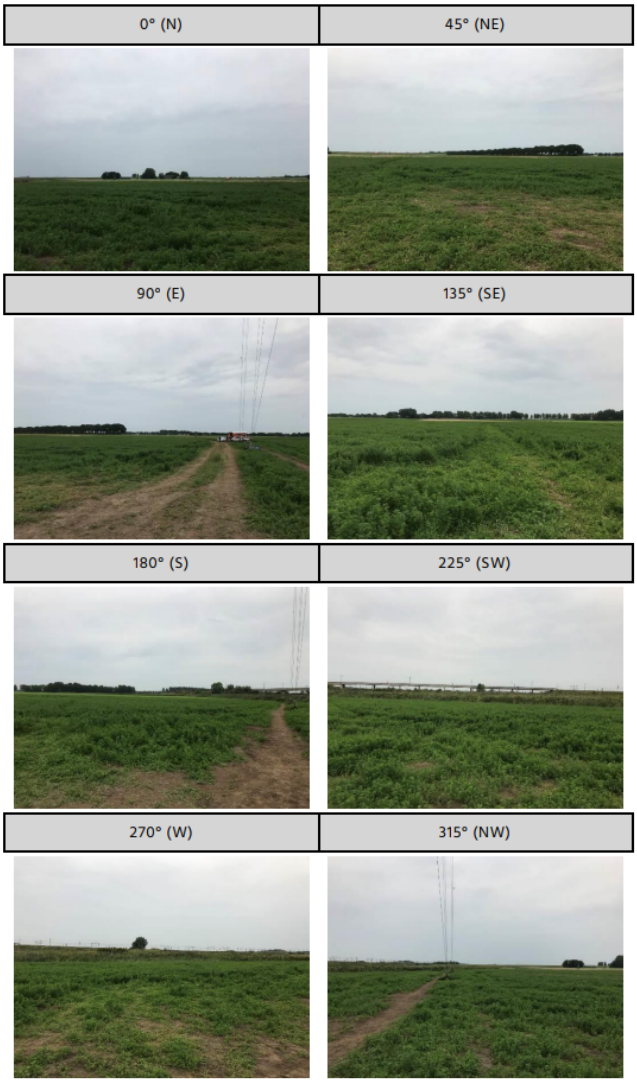

Figure F.4: Area surrounding Met Mast

Figure F.5: Met Mast Picture

Figure F.6: Met Mast (*circle*) + Lidar Location (*triangle*)

Figure F.7: Distance between past locations of lidar and met mast, based on installation reports (*note that both the lidar and met mast are removed and therefore not visible on the picture*)

F.4 Correlation coefficients

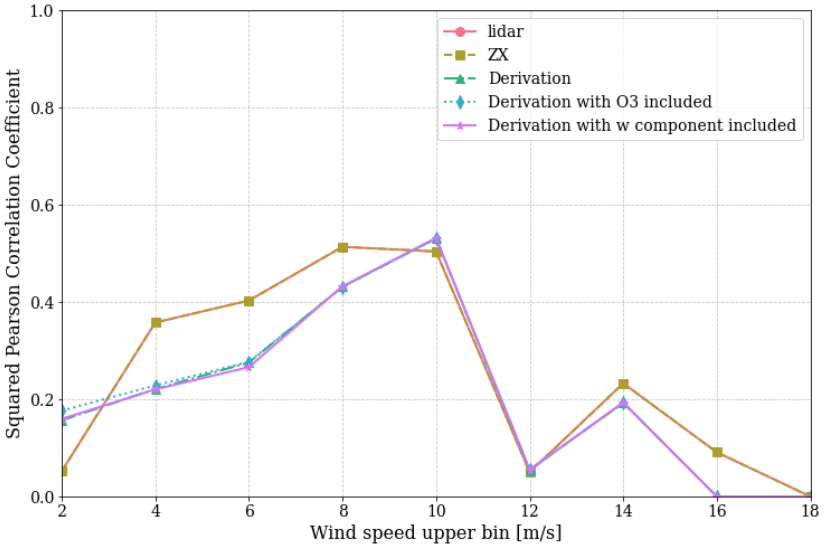

Figure F.8: SPCC vs Wind Speed at 82m

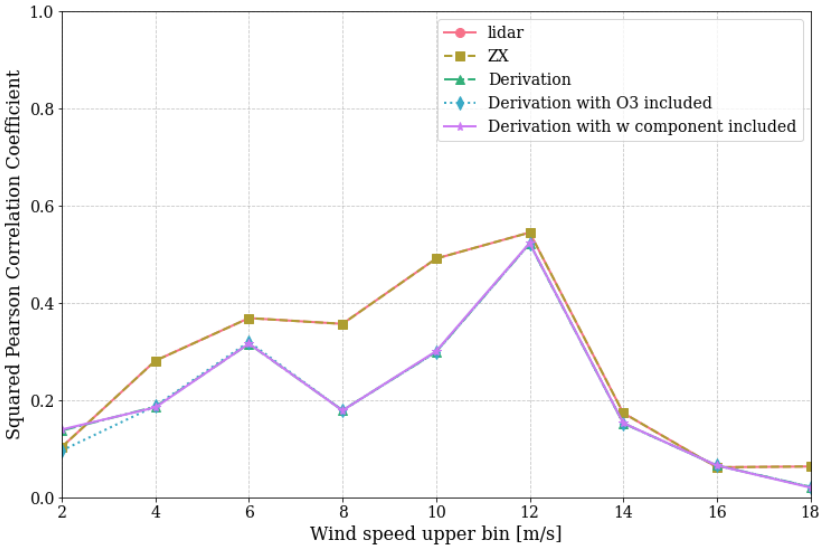

Figure F.9: SPCC vs Wind Speed at 122m

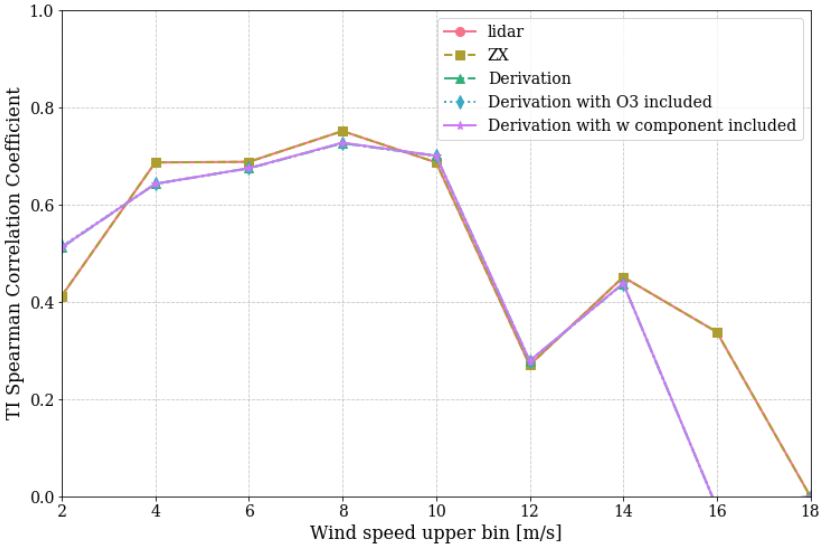

Figure F.10: SCC vs Wind Speed at 82m

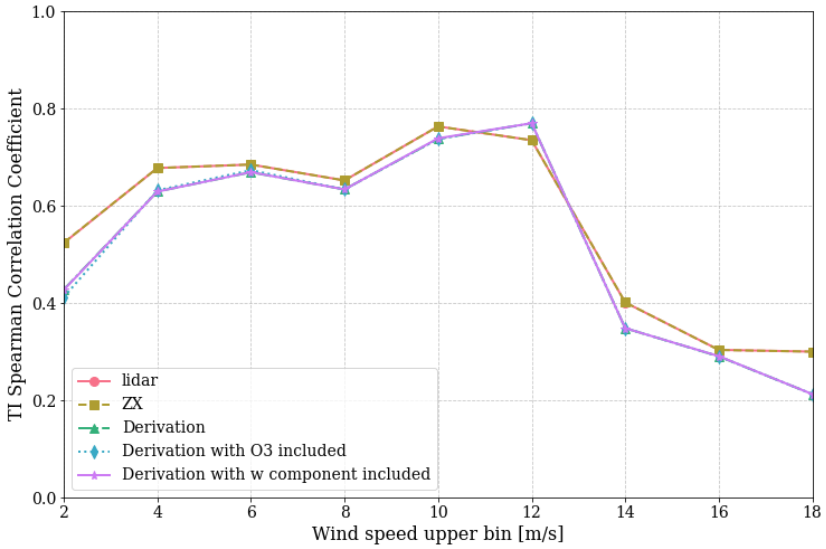

Figure F.11: SCC vs Wind Speed at 122m

F.5 Virtual lidar rings

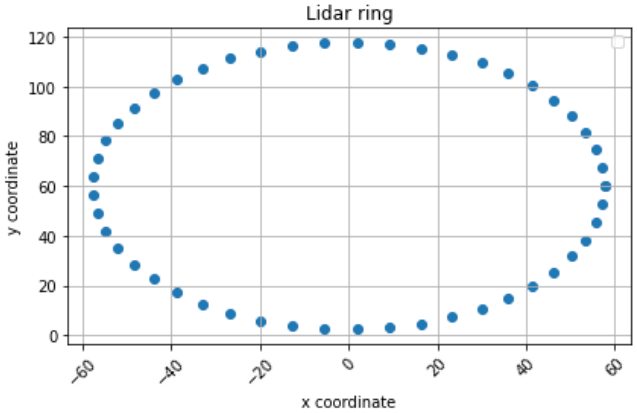

Figure F.12: Lidar ring for instant placement in turbulence box

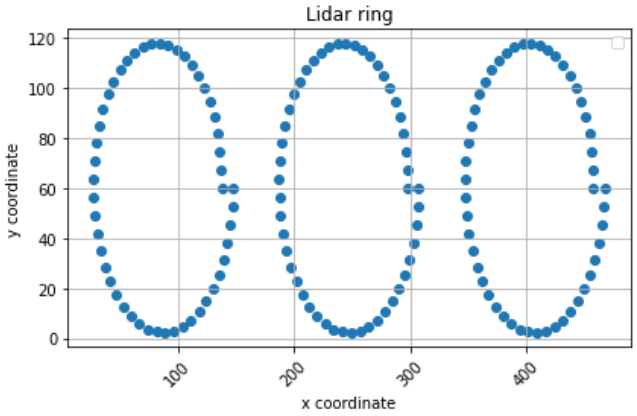

Figure F.13: Continuous lidar scan with 15 seconds interval due to height shifting

F.6 Bland-Altman plots for correlation analysis

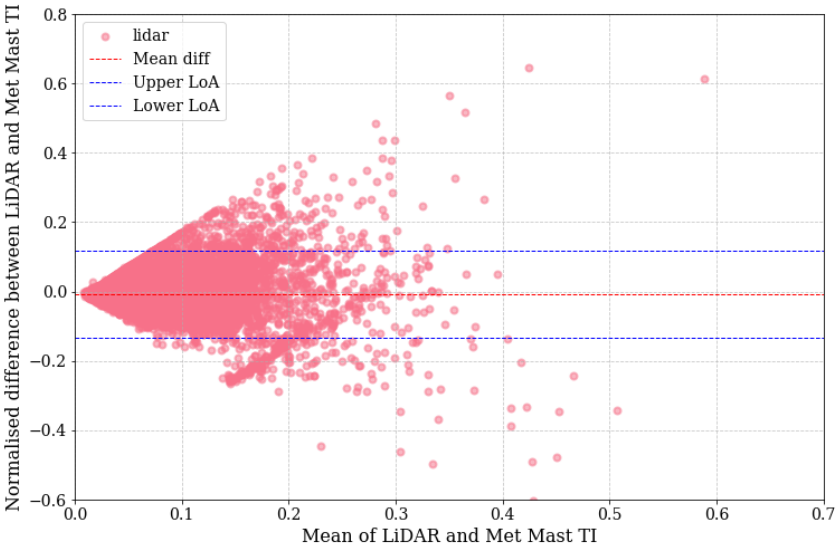

Figure F.14: Bland-altman Lidar vs met mast

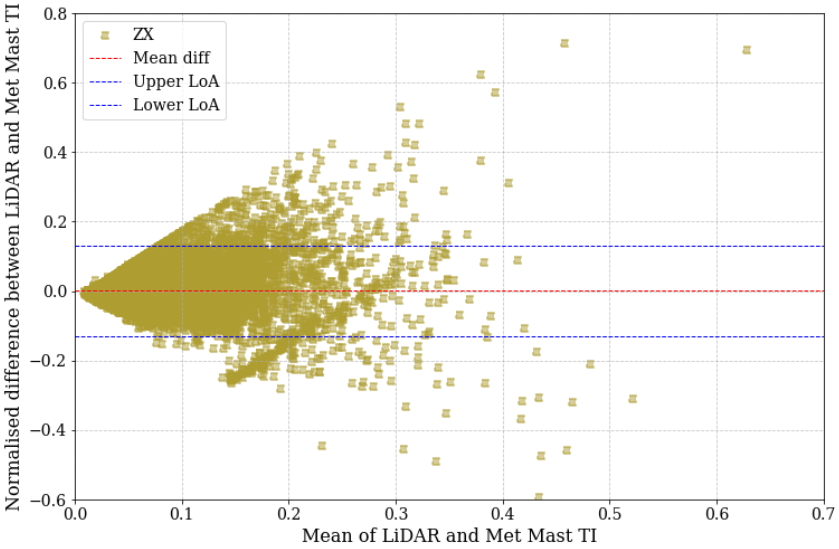

Figure F.15: Bland-altman Lidar ZX correction vs met mast

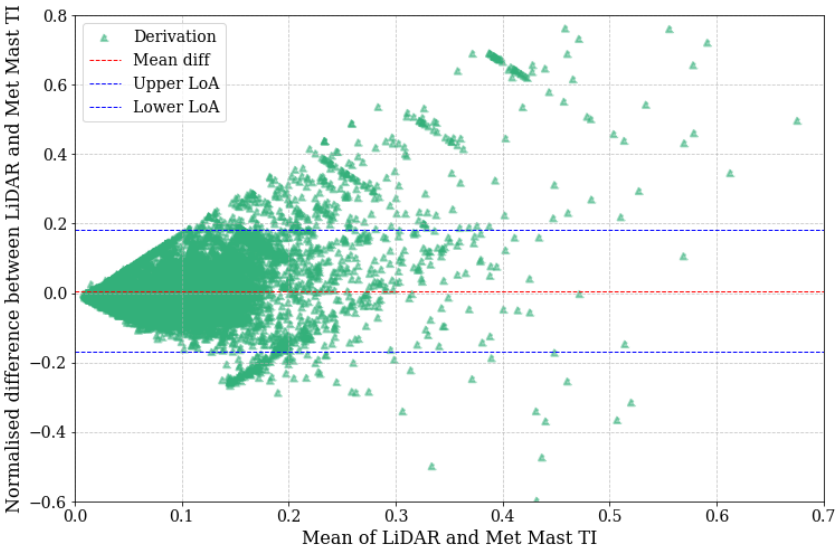

Figure F.16: Bland-altman Lidar Derivation Adjustment vs met mast

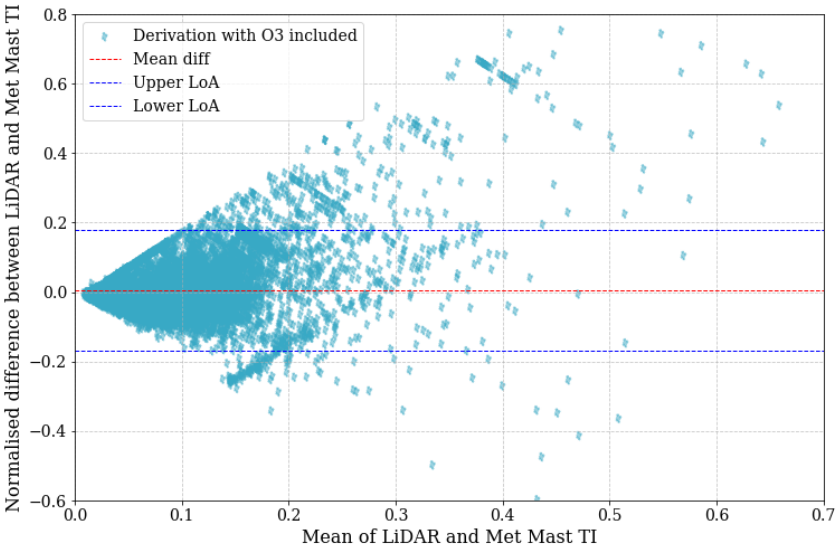

Figure F.17: Bland-altman Lidar O3 correction vs met mast

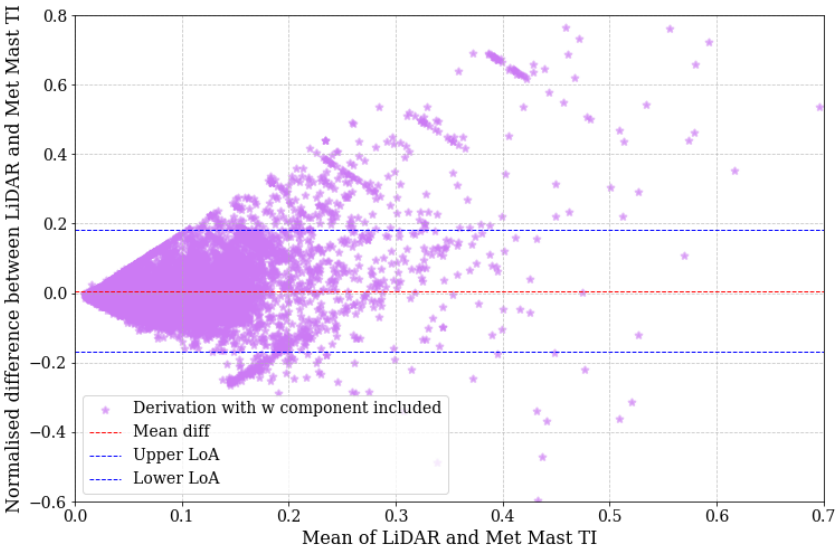

Figure F.18: Bland-altman Lidar w correction vs met mast

F.7 Monte Carlo simulations

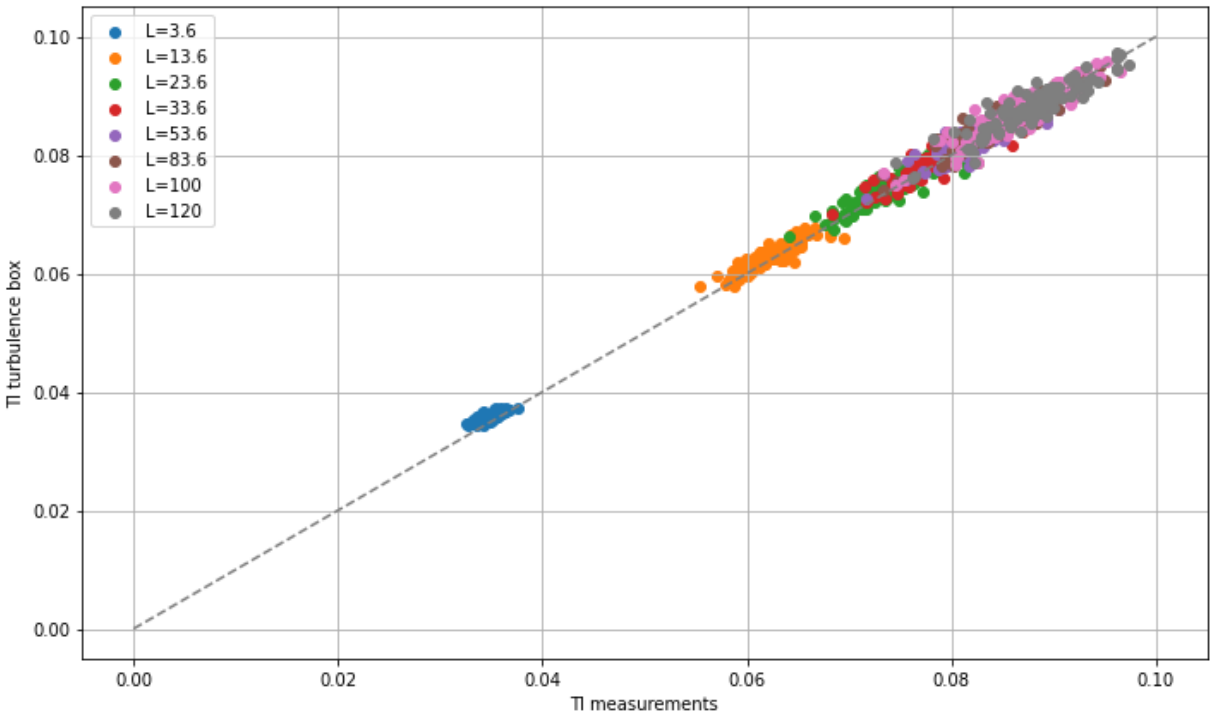

Figure F.19: Comparison of the non-adjusted TI after lidar measurements for different turbulent length scales

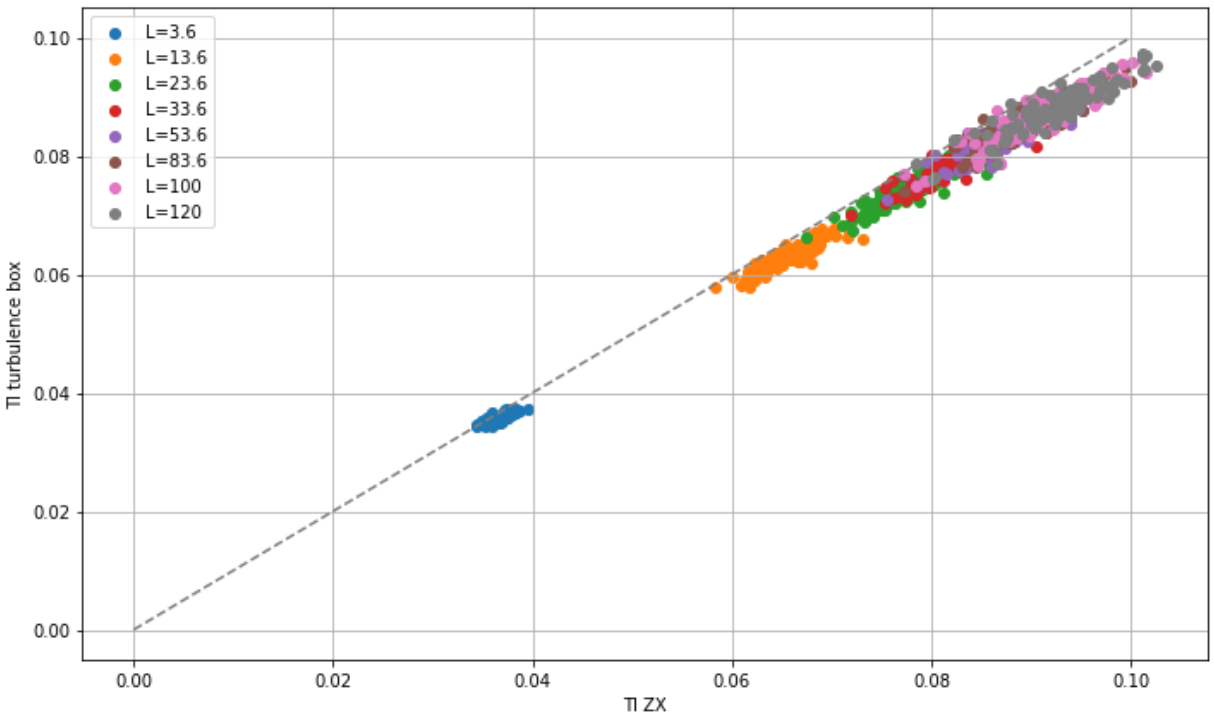

Figure F.20: Comparison of the ZX-adjusted TI after lidar measurements for different turbulent length scales

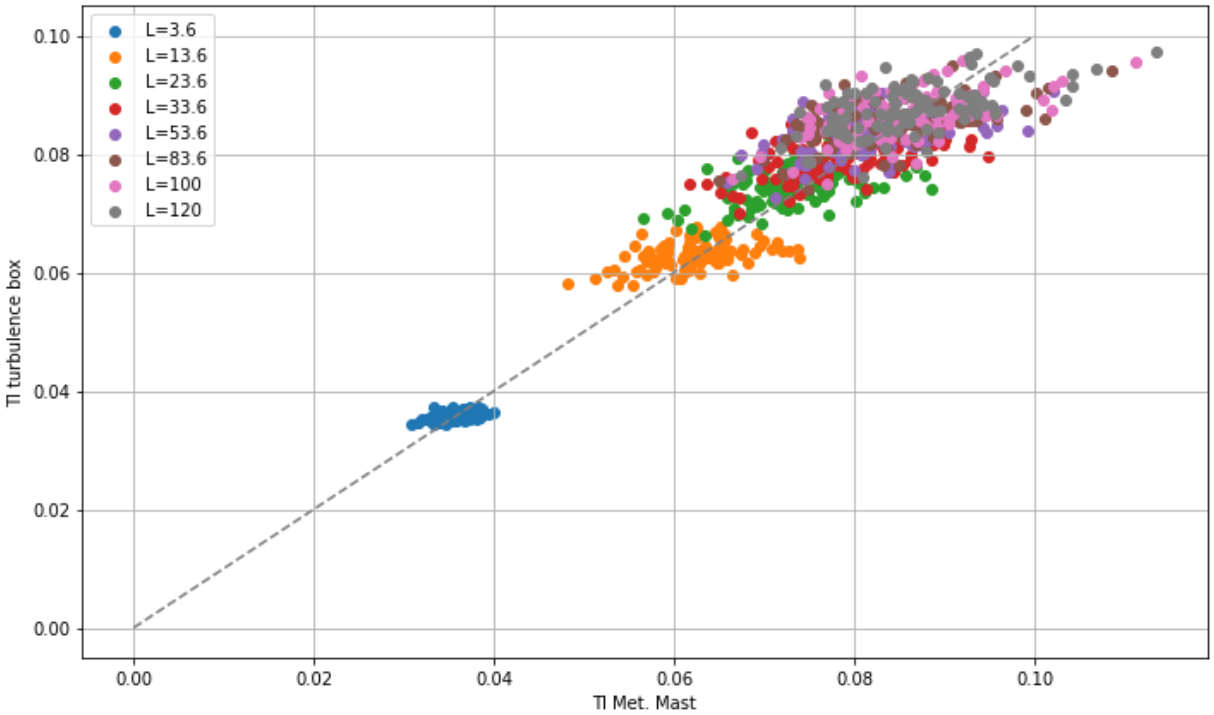

Figure F.21: Comparison of TI after met mast measurements for different turbulent length scales